Spinning and Mixing:
Two Studies of Microfluidic Problems
Using Molecular Dynamics Simulations

by

Eric C. J. Oliver

Thesis submitted in partial fulfilment
of the requirements for the degree of
Master of Science in Physics

University of Ottawa
August 2006

SUMMARY

Advances in microfluidics have led to the development of devices which can perform simple operations on fluids with the aim of developing a fully integrated “lab-on-a-chip”. Of prime importance to this procedure is the efficient operation of each individual component. Using theoretical predictions and two-dimensional Molecular Dynamics (MD) simulations, we have explored the operation of two such devices: one which forces a cavity of fluid into rotational motion and one to mix two different fluid species. For the rotational operation, we have referred to experimental results for a circular cavity coupled to a microfluidic channel in which a laminar flow is induced. This flow causes the fluid in the cavity to rotate which we model with MD simulations. We examine the role of wall-fluid interactions and its effect on enhancing the amount of angular momentum generated in the cavity. The reduction in wall-fluid interaction allows the fluid to slip along the wall and acquire a greater level of spin. We hope this technique can be applied experimentally to enhance the rotation in these devices. For the mixing operation, we examined a previously studied theoretical system where the authors claim obstacles in microchannels increase mixing efficiency for a fluid composed of two species. We make theoretical predictions to the contrary and demonstrate, using MD simulations, that our predictions are correct. Our results show that obstacles have two effects. First, obstacles increase the amount of contact between fluid species which only has a negligible effect on increasing the mixing efficiency. Second, the obstacles flatten the normally Poiseuille (quadratic) flow profile over a finite channel length which decreases the distance required for partial but not complete mixing. We demonstrate that all channels of at least a certain length, defined by the diffusive properties of the channel, will reach full mixing at the same point. Both projects illustrate the utility of MD simulations in predicting fluid behaviour in microfluidic systems. Our aim is that these studies can be integrated into the greater body of knowledge pertaining to microfluidics.

SOMMAIRE

Les récentes avancées dans le domaine de la microfluidique ont mené au développement d'appareils permettant d'effectuer des opérations simples sur des fluides dans le but de développer des systèmes entièrement intégrés de type laboratoire-sur-puce (« lab-on-a-chip ») . De tels systèmes intégrés sont caractérisés par l'efficacité individuelle de chacune de leurs composantes. À l'aide de prédictions théoriques et de simulations de type dynamique moléculaire (DM) en deux dimensions, nous avons exploré le fonctionnement de deux composantes envisagées pour les laboratoires-sur-puce: une cavité confinant le fluide tout en lui imposant un mouvement de rotation et un canal microfluidique permettant de mélanger deux types de liquide. Pour le cas de la cavité induisant une rotation du fluide, nous avons comparé nos résultats de simulation DM à des résultats expérimentaux d'une cavité circulaire couplée à un canal microfluidique dans lequel un écoulement laminaire avait été induit (faisant ainsi tourner le fluide dans la cavité). Nous avons examiné le rôle des interactions entre le mur et le fluide et leur effet sur l'augmentation du moment angulaire dans la cavité. Nos résultats indiquent que la réduction de l'interaction entre le mur et le fluide permet à ce dernier de glisser plus facilement et ainsi acquérir une plus grande vitesse de rotation. Nous espérons que cette technique puisse être appliquée expérimentalement pour augmenter la rotation dans ces appareils. Dans le cas du canal microfluidique permettant de mélanger deux types de liquide, nous avons examiné une prédiction théorique, jamais testée expérimentalement ou par simulation, selon laquelle deux types de liquide se mélangeraient plus facilement si des obstacles étaient ajoutés dans le micro-canal dans lequel se trouvent les liquides. Cependant, les résultats de nos simulations MD indiquent que les obstacles ne facilitent pas le mélange complet de deux fluides confinés à un micro-canal. Nous démontrons que la présence d'obstacles a deux effets. Premièrement, les obstacles augmentent bel et bien les contacts entre les différents fluides mais cet effet est négligeable en ce qui concerne l'efficacité du processus de mélange. Deuxièmement, les obstacles aplatissent le profil d'écoulement de Poiseuille (qui est normalement quadratique) sur une longueur finie, ce qui diminue la distance exigée pour obtenir un mélange partiel mais ne change en rien la distance nécessaire pour obtenir un mélange complet. Finalement nous démontrons de façon théorique que tous les canaux dont la longueur est supérieure à une longueur critique définie par les propriétés diffusives du canal, atteindront un état de mélange complet au même point. Les deux projets illustrent l'utilité des simulations de DM pour la prédiction du comportement des liquides dans les systèmes microfluidiques.

ACKNOWLEDGEMENTS

I would like to thank the following people and organizations:

. . .

Martin K, Fred, Martin B, Seb and Gary for discussions
Nick and Mike for diversions
J.-F., Michel, Fred and Owen for office antics
Fred and Michel for the pressure to make good figures :)
Martin K, Seb, Martin B, PAB and many others for good times
Michel, Fred, J.-F., Seb, Martin B, PAB et Gary pour améliorer ma langue seconde
Gary for his unfailing optimism!
All of the Slater group and the Department of Physics at U of O
Mom, Dad and Jason for support

. . .

for money of course: High Performace Computing Virtual Laboratory,
the Nunatsiavut Government and the Univeristy of Ottawa

. . .

and Lindsay for love, encouragement and patience

Table of Contents

1

Introduction

Molecular Dynamics simulations are rooted in two basic elements of our physical interpretation of our surroundings: that the world is inherently atomistic and that matter follows basic kinematic rules of motion. The proposition that matter is built of atomistic building blocks dates back to the scholars of antiquity. Kinematic laws of motion were formally expressed in the latter part of the second millenium, by figures such as Kepler and Newton. If we take the individual components of an atomistic view of the world and, combined with some approximations concerning the interactions between different components, consider them to follow a given set of kinematic rules then we can develop a model for basic matter itself. The last several decades has seen the level of computing power rise to the point where it is feasible to perform simulations involving many thousands of individual, interacting components using such a model.

In modern terms, these simulations involve finding a numerical solution to the many body problem, to which an analytical solution has eluded researchers for some time. Molecular Dynamics simulations are able to model actual materials, such as water, where the particles of the system represent molecules and atoms, such as oxygen and hydrogen. These simulations also involve models which handle interatomic bonds and electric interactions and have been able to predict amazing things pertaining to actual materials. The downside to this approach is that since it is highly computationally intensive simulations can only be run for small systems and short times.

We are interested in exploring the generic properties of microfluidic systems, particularly those pertaining to hydrodynamics and diffusion. In this case we perform what is called *coarse* *graining*, whereas the approach mentioned above (where components of the system represent actual molecules and atoms) is called *atomistic*. In coarse grain simulations, the individual particles do not represent molecules or atoms but a generic element of the material. These simulations produce generic properties of the systems, such as flow characteristics or thermodynamic properties, and are much less computationally intensive which allows for the simulation of larger systems over longer time scales. Clearly, Molecular Dynamics offers a method of simulating matter but it should be noted that the results can only be interpreted in terms of what general trends experimentalists should expect to observe in the physics, especially in the case of coarse grain models; the exact numerical results from Molecular Dynamics should not be taken at face value. Nevertheless, simulations can be used to point experimentalists in the right direction without needing to perform as many exhausting and costly experiments.

This thesis presents two different studies on systems involving fluids and solids which are broken down according to the method described above and simulated using Molecular Dynamics. Both systems have applications in microfluidics and so we will briefly review this field and summarize several papers that are relevant to our studies. We will also review the hydrodynamic, capillarity and diffusion theory relevant to our research as well as the implementation of the Molecular Dynamics computational model. Finally, we will introduce the two submitted manuscripts that form the bulk of this thesis as well as other work performed during the course of this degree.

Microfluidics

Microfluidics, and the closely related field of nanofluidics, is the study of the properties and dynamics of fluids on very small scales. It is a field where the assumptions of macroscopic models are at their most strenuous and the molecular structure of matter may become apparent. Furthermore, wall-fluid interactions often dominate the physics since the ratio of surface contact area to fluid volume is large. Microfluidics has made much progress in the past few decades and there are many resources on its history and current state of affairs including recent review articles by T. M. Squires and S. R. Quake [1] and J. C. Eijkel and A. van den Berg [2] as well as a book by P. Tabeling [3]. It is becoming increasingly possible to create a “lab-on-a-chip” by integrating a series of microfluidic operations in order to perform a specific experiment or measurement. For such a device to operate succesfully, each individual operation must be performed properly. This

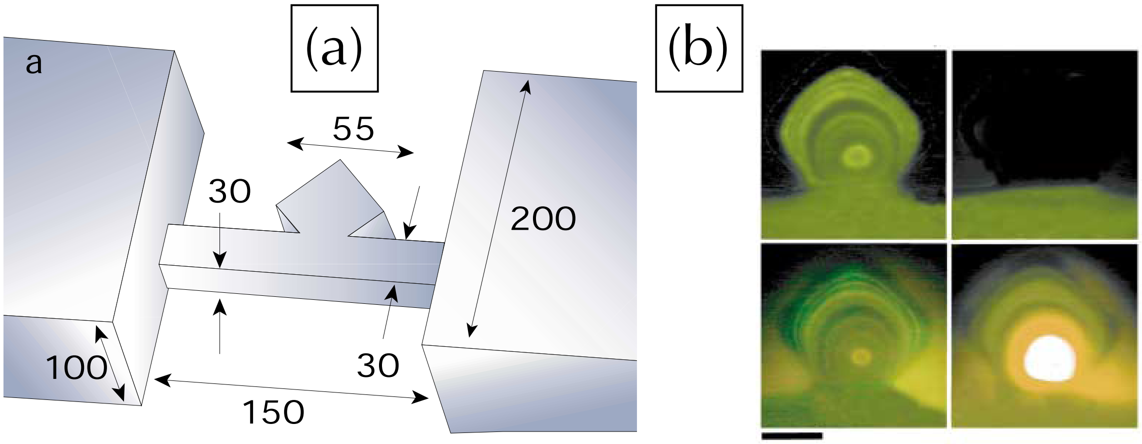

FIGURE 1.1 (a) System used by the Chiu group to explore fluid rotation in a microcavity. A pressure difference is created between the two large resevoirs which generates a Poiseuille flow in a narrow channel (all dimensions are in μm). A small cavity is coupled to the channel to allow transfer of momentum (via viscous coupling at the channel-cavity interface) between it and the channel. (b) Streamlines in the rotating cavity fluid (visualized using fluorescent beads). The scale bar is 25 μm. Figures pending permission from authors and journal [4].

thesis will explore methods to perform two such operations: rotation of a microcavity of fluid and mixing of a binary component fluid, dubbed “spinning” and “mixing”, respectively.

Relevant Examples

The results presented in this thesis build upon and make reference to many previous works. However, there are several articles in particular that merit a general review in order for the reader to aquaint themselves with the research and better understand the thesis. The first set of articles are by a group led by Daniel T. Chiu at the University of Washington, Seattle, USA and concern the rotation of a cell of fluid which is coupled to a flow in a microchannel. The second set of relevant research publications concern a hydrodynamics study by Wang *et al.* at the Industrial Research Istitute, Swinburne University of Technology, Victoria, Australia on the effects of obstacle arrangements in microchannels on the mixing characteristics of a binary component fluid.

Fluid Rotation: Microvortices

The Chiu group has demonstrated the ability to generate large radial accelerations of fluid in a microcavity (which they term a microvortex) by coupling it to the flow in a microchannel. The

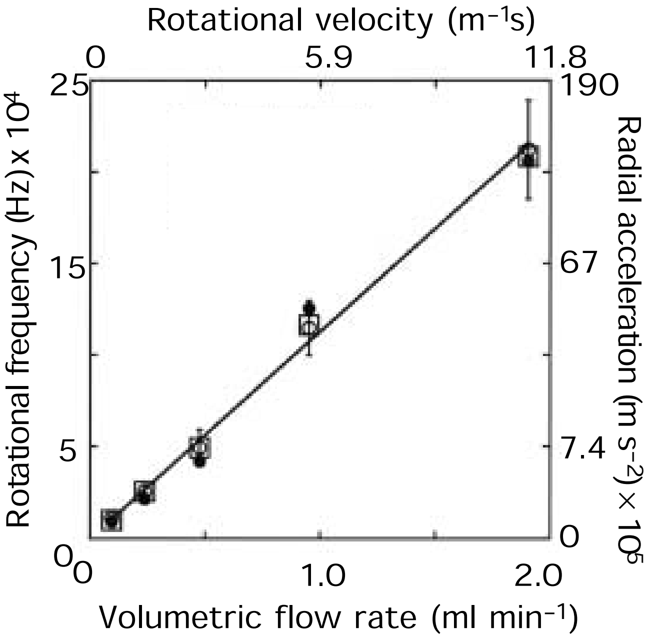

FIGURE 1.2 Results demonstrating a linear dependence of radial acceleration in the microcavity with flow rate in the channel. Figure pending permission from authors and journal [4].

basic system geometry can be seen in Fig. 1.1a. There are two large resevoirs on the left- and the right-hand side connected by a channel of length 150 μm and square cross-sectional width 30 μm. A pressure difference is set up between the large resevoirs which creates a Poiseuille flow in the channel with flow rates on the order of 10 m/s. A small cavity of diameter 50 μm is coupled to the channel and the fluids in each region are allowed to exchange matter and momentum. Consequently, the fluid in the cavity is driven by the fluid in the channel into rotational motion. The streamlines in the cavity have been visualized by injecting fluorescent beads into the fluid and monitoring their flow path (see Fig. 1.1b) where it is clear that the fluid is undergoing rotational motion. Chiu *et al* have measured the radial acceleration in the cavity as a function of the flow rate in the channel and observed a linear relationship (see Fig. 1.2). Furthermore, for the largest flow rates (~ 45 m/s) the radial acceleration was measured to be 1.4×10^7 m/s or 1.4×10^6 g! One interesting aspect of the experiment is the existence of a vortex in laminar flow; vortices are usually only observed in turbulent flows. Over the course of three published studies [4, 5, 6], this group has been the first to develop this technique and has used a device operating on the same principle to study the effect of stress on a biological cell placed in the cavity.

Our first research study in this thesis is on simulating and extending this project. As the Chiu group mentioned in their papers, the flow in the channel is damped near the wall, which is characteristic of pressure-driven flow, and this has a direct effect on the driving force coupled to the channel. They observe that the maximum fluid rotational velocity is only about 20% of the average flow speed in the channel. By simulating the system with Molecular Dynamics we can explore methods of increasing the flow speed at the wall and thus try to increase the level of spin in the cavity without an significant increase in average flow speed. We have experimented with modifications to the wall-fluid interaction in order to simulate hydrophobicity. As we shall demonstrate, reducing the wall-fluid interaction will allow for enhanced spin generation for the same flow rate. Furthermore, simulating using Molecular Dynamics will allow for explorations of the system on the nanoscale.

Mixing With Obstacles

Efficient mixing in microchannels has been an open problem in microfluidics for many years now. In channels of microscale cross section, flows are generally in the laminar regime. Laminar flow lacks eddies and other instabilaties that allow turbulent flows to mix fluids efficiently (think of pouring cream into your cup of coffee). The only natural process that remains to mix the fluids is diffusion, which is quite slow relative to the flow speed. Many methods have been proposed to increase mixing efficiency in laminar flows including active processes (such as moving parts), splitting the flow into multiple segments (thus reducing the channel width needed to diffuse) and channels with significant lateral convection caused by radial acceleration. A recent study has proposed the use of obstacles placed in the channel to increase the level of mixing.

Wang *et al* has studied binary, miscible fluid flow in a microchannel using numerical solutions to the Navier-Stokes equations for macroscopic hydrodynamics [7, 8]. They operate in the laminar flow regime and parameters are chosen such that advection dominates over diffusion and so mixing is very difficult to achieve. A schematic of their system can be seen in Fig. 1.3a and consists of two arms on the left containing distinct fluid species which, under the influence of a pressure difference, flow into the main channel and initiate mixing. With the aim to enhance mixing, cylindrical obstacles (isotropic in the direction perpendiular to x and y) are placed in the channel to disrupt the flow. These obstacles are arranged in many different schemes (seen in Fig. 1.3b) with, according to the authors, the most succesful one being when the obstacles are arranged in a prism-like configuration. Also, in that figure they show a visual representation of the fluids from which we can

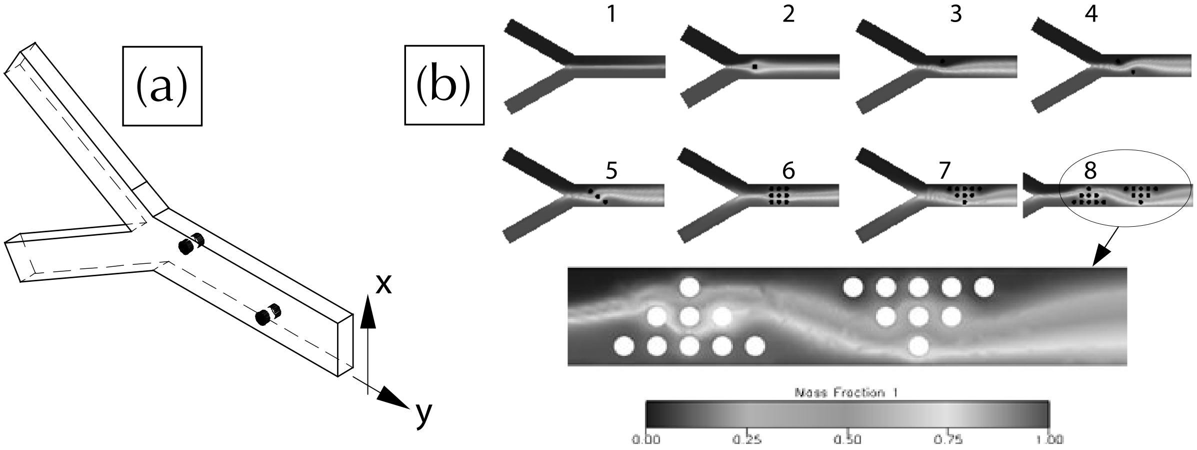

FIGURE 1.3 (a) System used to explore mixing of a binary fluid using obstacles. Two fluid species enter from the arms on the left into the main channel and commence mixing. (b) Numerical results for fluid mixing from various obstacle configurations. Prism-like configurations are the most promising. Figures pending permission from authors and journal [7].

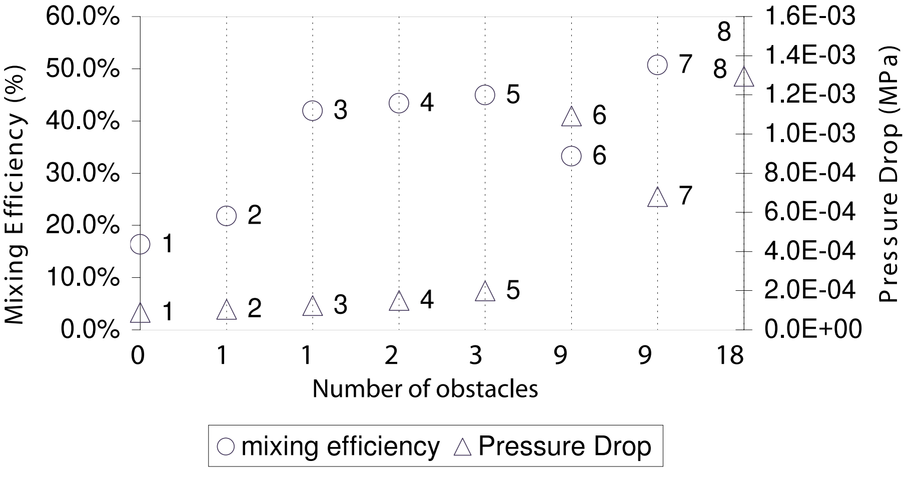

FIGURE 1.4 Mixing results of the various obstacle conformations with the mixing level measured at the outlet of the channel. In general the mixing eficiency increases with the number of obstacles in the channel. Also, the pressure difference required to maintain the same flow rate also increasess with the number of obstacles. Figure pending permission from authors and journal [7].

observe how the obstacles disrupt the streamlines of the fluid. Using a phenomenological function based on concentration they calculate the mixing at the outlet for each obstacle configuration as well as the pressure difference required to maintain the same flow rate (see Fig. 1.4). The mixing efficiency, 0% being unmixed and 100% being fully mixed, rises with the number of obstacles. Their claim is that since laminar flow cannot be turbulent the obstacles induce lateral motion in the fluid which effectively pushes one fluid species into the other, thus enhancing mixing.

Simulations using Molecular Dynamics of mixing in microchannels can be used to examine several properties of such systems. Since we can tune the interaction potential, we can easily simulate fluid with different properties (such as viscocity and density) and even an immiscible fluids mixture. Also, Molecular Dynamics simulations will allow the testing of mixing properties of nanoscopic channels. In our second article we test the hypothesis presented by Wang *et al* using Molecular Dynamics simulations.

Theory

We will introduce several theoretical topics that are required for understanding the two projects presented in this thesis. For the mixing project, we will present the theory of diffusion in both microscopic and continuum formulations. Both projects, being studies of fluids, will rely on hydrodynamic predictions. The relavent subjects include the Navier-Stokes equation and fluid mechanics in the laminar flow regime. Finally, for the project relating to the fluid microvotices, we will make use of capillarity theory in understanding the wall-fluid interactions.

Diffusion

Molecular Dynamics deals with motion of matter on the molecular scale and of particular importance to dynamics is diffusion, the process by which matter is transported across a system through random molecular motions. The idea began with Brown[1] who, when examining pollen grains in solution, determined that the random motions he observed “arose neither from currents in the fluid, nor from its gradual evaporation, but belonged to the particle itself” [10]. Between the time of Brown and that of Einstein, it was conjectured that the individual particles of a fluid are knocked

---

[1] Robert Brown (1773-1858) was a British botanist who collected samples in Australia during the late 19th century. He is well known for is work in botany as well as his contributions to what would be known as Brownian motion and the theory of Diffusion. He is commemorated in Australia with the herb genus *Brunonia* and many Australian species such as *Eucalyptus brownii* [9].

in random directions by a series of collisions with other fluid particles. Einstein[2] later presented an expression for the average time $\langle t_{\mathrm{D}} \rangle$ a particle would take to diffuse a distance d from its starting point:

$$\langle t_{\mathrm{D}} \rangle = \frac{d^2}{2N_{\mathrm{d}}D}, \tag{1.1}$$

where D is the diffusion coefficient which can be related to viscosity and measures the rate of diffusion and N_{d} is the number of dimensions we are considering the diffusion to be constrained to. This shows that for a given diffusing particle, the distance it has travelled goes like the square root of the time which it has been diffusing.

Einstein's relation can also be deduced from the one-dimensional diffusion equation:

$$\frac{\partial C}{\partial t} = D\frac{\partial^2 C}{\partial x^2}, \tag{1.2}$$

where C is concentration. From this equation we can deduce that concentration will tend to even out over time, with a net flux from regions of high concentration to those with low concentration. With initial condition of all concentration condensed at the origin (a delta function: $C(x,t) = M\delta(x)$), the solution to this equation is

$$C(x,t) = \frac{M}{\sqrt{4\pi Dt}} \exp\left(-\frac{x^2}{4Dt}\right), \tag{1.3}$$

where M is the total amount of whatever substance we are considering: $M = \int_{-\infty}^{\infty} C(x,t)dx$ [12]. If we treat this expression as a Gaussian[3] probability distribution then we can extract the standard deviation as a function of time to be $\sigma = \sqrt{2Dt}$ which is equivalent to the earlier expression attributed to Einstein in one dimension. If more dimensions are considered in the diffusion equation, one can recover the general version given Eq. 1.1.

---

[2] Albert Einstein (1879-1955), a German-Jewish theoretical physicist, is one of the most celebrated scientists in History. In his "wonderful year" (1905) alone he published seminal works on Brownian motion, the photoelectric effect and special relativity. Ten years later, he would formulate the theory of General Relativity which was a cornerstone of twentieth-century physics. After leaving Nazi Germany and under fears of Nazi use of nuclear weapons, he urged US president F. D. R. to look into sponsoring research on nuclear fission. This eventually grew into the Manhattan project [11].

[3] Carl Friedrich Gauss (1777-1855), sometimes known as "the prince of mathematicans" was a prolific German mathematician and scientist born in Brunswick (now a part of Lower Saxony, Germany). He contributed to many fields, including number theory, analysis, differential geometry, geodesy, magnetism, astronomy and optics, and is considered one of history's greatest mathematicians. And so, for good reason, his name appears on many mathematical and scientific items including the Gaussian probability distribution and the physical unit of magnetic flux density [13].

Macroscopic Hydrodynamics

The vast majority of the fluid modelling in this thesis has been done using Molecular Dynamics to explicitly represent the fluid particles as interacting beads. However, for miscible fluids with wetting walls it is possible to recover the predictions of macroscopic hydrodynamics given by the Navier[4]-Stokes[5] (NS) equation within only a few particle layers. For example, in simulations of Poiseuille and Couette flow, the velocity and stress fields are in complete agreement with NS for systems with channel width larger than about 10 bead diameters [16]. Therefore, we will on occasion make reference to macroscopic predictions and it is worth discussing some of these topics.

The Navier-Stokes Equation

The Navier-Stokes equation describes the motion of a fluid (such as a liquid or gas) by expressing momentum changes in terms of pressure gradients, viscous forces and external fields. This equation is derived from laws of conservation (such as mass and momentum) and for incompressible fluids and can be expressed as

$$\rho\frac{d\boldsymbol{u}}{dt} - \rho\left(\boldsymbol{u}\cdot\nabla\right)\boldsymbol{u} = -\nabla p + \rho\boldsymbol{g} + \eta\nabla^2\boldsymbol{u}, \tag{1.4}$$

where $\boldsymbol{u} = u\hat{\mathrm{x}} + v\hat{\mathrm{y}} + w\hat{\mathrm{z}}$ is the velocity vector, ρ is the fluid density, η is the shear (or kinetic) viscosity, p is the pressure and $\rho\boldsymbol{g}$ is an external force per unit volume [17]. The Navier-Stokes equation, along with the continuity equation

$$\nabla\cdot\boldsymbol{u} = 0, \tag{1.5}$$

determines the flow properties of Newtonian fluids. In this work all modelling is done in two dimensions and as such it is possible to simplify the system for numerical purposes by using the

---

[4] Claude-Louis Navier (1785-1836) was a French physicist and engineer born in Dijon, France. He studied at the École polytechnique and the French Academy of Science in Paris. He is best known for his contributions to fluid mechanics, which along with George Stokes, led to the Navier-Stokes equation [14].

[5] Sir George Gabriel Stokes (1819-1903) was an Irish scientist born in Skreen, County Sligo. He studied at schools in Skreen, Dublin and Bristol and went on to hold a position at Pembroke College, Cambridge. He made significant contributions to the fields of mathematical physics (Stoke's theorem), optics (theory of diffraction, the Stokes line) and fluid mechanics (Stokes flow). He is most remembered for his contributions to fluid mechanics, which along with those of Claude-Louis Navier, led to the Navier-Stokes equation, a cornerstone of hydrodynamic theory [15].

vorticity-streamfunction formulation of the problem. The streamfunction ψ is defined as constant along streamlines which are everywhere tangent to the velocity field. This can be defined in the following way:

$$\frac{\partial \psi}{\partial y} = u \quad , \quad \frac{\partial \psi}{\partial x} = -v. \tag{1.6}$$

The vorticity $\boldsymbol{\omega}$, which can be thought of as a measure of circulation per unit area along streamlines, is defined as the curl of velocity field. In two dimensions this vector will always point in the z direction and so we use only the magnitude of the curl:

$$\omega \equiv ||\boldsymbol{\omega}|| = \frac{\partial v}{\partial x} - \frac{\partial u}{\partial y}. \tag{1.7}$$

If we take the curl of Eq. 1.4 and note that $\nabla \cdot \boldsymbol{u} = 0$ and $\nabla \cdot \boldsymbol{\omega} = 0$ (since the divergence of a curl is always zero) we can reduce the incompressible Navier-Stokes equation (ignoring the pressure gradient and any external forces) to

$$\frac{\partial \omega}{\partial t} + \boldsymbol{u} \cdot \nabla \omega = \frac{\eta}{\rho} \nabla^2 \omega. \tag{1.8}$$

Also, if we substitute the definitions for the streamfunction into the the vorticity equation (Eq. 1.7) we get

$$-\nabla^2 \psi = \omega. \tag{1.9}$$

Together, Eqs. 1.8 and 1.9 form the vorticity-streamfunction formulation of the Navier-Stokes equation previously defined in terms of velocities by Eqs. 1.4 and 1.5. We will use this formulation to compute macroscopic predictions for our MD simulations.

Dynamic Similarity and Nondimensional Parameters

We are working with MD simulations whose exact dimensions and values such as flow speed are not precisely defined since, in coarse-grain MD, there is always some freedom in the choice of parameters. However, under certain conditions, two systems with very different dimensions and parameter values can still be *dynamically similar*: meaning their basic flow characteristics will be the same [17]. Two systems are dynamically similar if the value of a certain nondimensional parameter is the same in both cases. The form of the nondimensional parameter depends on the nature of the problem and what effects one considers relevant (such as viscosity, diffusion, velocity, etc.).

For a given problem, the nondimensional parameters can be found either by nondimensionalizing the governing equation(s) (such as NS) or by simple dimensional analysis on the relevant parameters involved. For example, if we nondimensionalize the parameters in the Navier-Stokes equation (Eq. 1.4) by scaling as follows:

$$\boldsymbol{x}' = \frac{\boldsymbol{x}}{L} \quad , \quad \boldsymbol{u}' = \frac{\boldsymbol{u}}{U} \quad , \quad t' = \frac{t}{L/U} \quad , \quad p' = \frac{p}{\eta U/L}, \tag{1.10}$$

where L and U are the characteristic length and velocity of the system, then we have

$$\frac{\rho U L}{\eta}\frac{d\boldsymbol{u}'}{dt'} - \frac{\rho U L}{\eta}\left(\boldsymbol{u}' \cdot \nabla'\right)\boldsymbol{u}' = -\nabla' p' + \frac{\rho U L}{\eta}\frac{\boldsymbol{g}L}{U^2} + \nabla'^2\boldsymbol{u}'. \tag{1.11}$$

Now we can create two nondimensional parameters: the Reynolds[6] number and the Froude[7] number which are defined as

$$\mathrm{Re} \equiv \frac{\rho U L}{\eta} \quad , \quad \mathrm{Fr} \equiv \frac{U}{\sqrt{gL}} \tag{1.12}$$

and measure the effects of viscous and external forces, respectively, relative to the characteristic inertial force in the system. Thus, the Navier-Stokes equation becomes

$$\mathrm{Re}\left(\frac{d\boldsymbol{u}'}{dt'} - \left(\boldsymbol{u}' \cdot \nabla'\right)\boldsymbol{u}'\right) = -\nabla' p' + \frac{\mathrm{Re}}{\mathrm{Fr}^2} + \nabla'^2\boldsymbol{u}'. \tag{1.13}$$

The Reynolds number is of particular importance, as will be seen in the following section, since it allows one to differentiate between the regimes of laminar flow (where viscous forces are dominant) and turbulent flow (where inertial forces are dominant).

If we have diffusion in the presence of flow then the concentration profiles are governed by the the advection-diffusion equation

$$\frac{\partial C}{\partial t} = D\frac{\partial^2 C}{\partial x^2} + u\frac{\partial C}{\partial x}, \tag{1.14}$$

where u is the velocity of the flow. This is formulated by adding an advection term to Eq. 1.2. This equation has the result of transporting the solution to the diffusion equation along x at the constant

---

[6] Osbourne Reynolds (1842-1912) was a fluid dynamics engineer born in Belfast, Ireland. He studied mathematics at Cambridge and later became a professor in Manchester. He is best known for his studies on fluid flows in pipes, particularly the transition from laminar flow to turbulent flow. From his observations on the ratio of inertial to viscous effects in his experiments he formulated the Reynolds number to characterize the flow [18].

[7] William Froude (1810-1879) was born in Dartington, Devon, England and worked as an engineer, hydrodynamiscist and naval architect. Educated at Oxford, he formulated laws on water resistance to ships and predictions on their stability. The Froude number is named after him [19].

speed u (simply make the substitution $x \rightarrow x - ut$ in Eq. 1.3). Now if we apply the methods of nondimensionalization described above with the following substitution

$$x' = \frac{x}{L} \quad , \quad u' = \frac{u}{U} \quad , \quad t' = \frac{t}{L/U} \quad , \quad C' = \frac{C}{C_0}, \tag{1.15}$$

where L, U, and C_0 are the characteristic length, speed and concentration of the system then we have the following equation

$$\frac{\partial C'}{\partial t'} = \frac{1}{\mathrm{Pe}} \frac{\partial^2 C'}{\partial x'^2} + u' \frac{\partial C'}{\partial x'}. \tag{1.16}$$

We have recovered the Péclet[8] number (or *stirring number* [21]): $\mathrm{Pe} \equiv UL/D$. This number measures the relative effects of diffusive motion and advective (inertial) motion. If it is large then advection dominates and the concentration profile will be transported with little deformation due to diffusion and if it is small then diffusion dominates and we can reduce the equation to Eq. 1.2 where the concentration profile spreads with little advective transportation. This distinguishes between regimes where fluid is transported predominantly as a result of external forces or by internal Brownian motion.

Laminar Flow

As discussed above, the Reynolds number measures the relative effects of viscous and inertial forces. Generally speaking, most flows on the macroscopic scale are dominated by inertia and turbulent effects are easy to generate (such as the eddies as smoke billows through air). However, when viscous forces dominate, for approximately $\mathrm{Re} < 10^3$, the flow is referred to as laminar and such instabilities cannot occur.

Consider Eq. 1.13 for small Re and Fr (i.e., viscous forces dominate and there is significant external forcing ρg). Since the Reynolds number is small we can neglect the left-hand side and since the Froude number is also small we can leave the term proportional to the external force and we have

$$0 = -\nabla' p' + \frac{\mathrm{Re}}{\mathrm{Fr}^2} + \nabla'^2 \boldsymbol{u}' \tag{1.17}$$

which is the governing equation for steady state laminar flows. If we consider a two dimensional channel (parallel to the xy-plane, with walls at $\pm y_0$) with no pressure gradient ($\nabla p = 0$) and

---

[8] Jean Claude Eugène Péclet (1793-1857) was a French physicist born in Besançon, France. He taught physics widely in France during his time, including schools in Paris (École Normale) and Marseilles (Collège de Marseilles). The Péclet number is named in his honour [20].

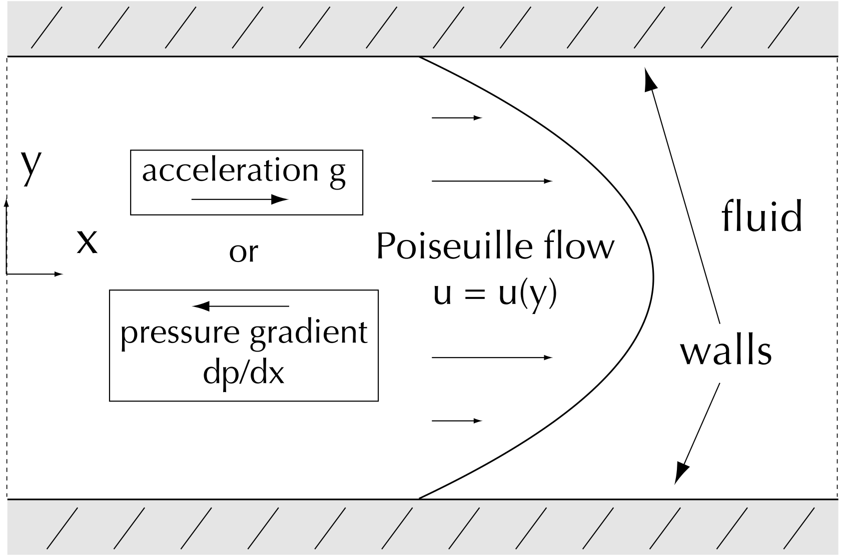

FIGURE 1.5 Fluid confined between two plates parallel to the xz-plane under the influence of either a gravity-like force or a pressure gradient. With no-slip at the wall the fluid will flow in the x direction with a quadratic Poiseuille flow profile across the channel.

an external force density ρg in the x-direction then the fully developed flow ($\partial u/\partial x = 0$) is described by

$$0 = \frac{\rho g}{\eta} + \frac{\partial^2 u}{\partial y^2}. \tag{1.18}$$

If we enforce no slip boundary conditions (i.e., $u(\pm y_0) = 0$), this differential equation has the solution,

$$u(y) = \frac{\rho g}{2\eta}\left(y_0^2 - y^2\right) \tag{1.19}$$

which is known as the Poiseuille[9] flow profile (see Fig. 1.5). Note that a pressure gradient along x would create a similar quadratic flow profile with the substitution $\rho g = -dp/dx$:

$$u(y) = -\frac{dp/dx}{2\eta}\left(y_0^2 - y^2\right). \tag{1.20}$$

If both a pressure difference and external acceleration exist, then the resulting flow profile will be the sum of Eqs. 1.19 and 1.20.

---

[9] Jean Louis Marie Poiseuille (1799-1869), a French mathematician and physicist, was born in Paris and studied at the École polytechnique. With interest in human blood flow in capillaries, he is best known for his formulation of Poiseuille's law. This law described the laminar flow of Newtonian fluids in cylindrical tubes of constant cross section [22].

We have enforced *no-slip* boundary conditions, which ensures that the fluid does not move along its contact point with the stationary walls. However, there are situations where this condition will not hold, such as water in contact with hydrophobic walls [23], and there will be a finite positive fluid velocity at the walls. We can characterize this *slip* by the *slip length*, δ: the distance outside the walls at which the fluid velocity is extrapolated to zero. A common measure of the slip length is through the following condition at the wall:

$$\left.\frac{du}{dy}\right|_{y_{\mathrm{wall}}} = \frac{u_{\mathrm{wall}}}{\delta}, \tag{1.21}$$

where y_{wall} is the position of the wall. Another measure would be to apply Eq. 1.19 where y_0 no longer represents the position of the wall but the position at which the velocity is zero (since the two are no longer the same). In both cases, the slip length is defined as $\delta = y_{\mathrm{wall}} - y_0$.

We can generalize the equation for Poiseuille flows in the case of slip. Assume the slip at the upper wall $(+y_0)$ is equal to δ_+ and the slip at the lower wall $(-y_0)$ is equal to δ_-, in other word $u(y_0 - \delta_+) = 0$ and $u(-y_0 + \delta_-) = 0$, then the solution to Eq. 1.17:

$$u(y) = \frac{\rho g}{2\eta}\left(y_0 + \delta_+ - y\right)\left(y_0 + \delta_- + y\right). \tag{1.22}$$

The profile retains its quadratic nature but now is nonzero at the walls and can be assymetric if $\delta_- \neq \delta_+$. We will observe such a phenomenon in our studies.

Capillarity Theory

In our MD simulations we will be experimenting with the interaction between solid and fluid phases of matter and will be measuring properties of interfaces between such phases. Therefore, it will be necessary to have an understanding of the physics under such conditions which can be found under the field of capillarity theory and draws on fields such as fluid mechanics and thermodynamics.

Between two phases of matter there exists an interface and an energy can be associated with this interface: the interfacial energy or *surface tension*. If we consider three phases of matter (solid, liquid and gas) in coexistence, then there are three interfaces, each with its own surface tension, and if the solid surface is flat, then the liquid-gas interface will make a specific contact angle with the solid surface (see Fig. 1.6 for a schematic representation). The three surface tensions, denoted by γ_{ij}, where i and j are two phases, and the contact angle, θ, can be related through Young's[10] equation [25]:

$$\gamma_{\mathrm{sg}} = \gamma_{\mathrm{ls}} + \gamma_{\mathrm{lg}} \cos\theta. \tag{1.23}$$

We will consider materials to interact via the Lennard-Jones potential (or 6-12, as it is sometimes known):

$$U(r_{ij}) = 4\epsilon \left[\left(\frac{\sigma}{r_{ij}} \right)^{12} - c_{ij} \left(\frac{\sigma}{r_{ij}} \right)^{6} \right] \tag{1.24}$$

where ϵ and σ are constants which set the energy and length scales [26] and i and j refer to two interacting materials. The two terms in the potential arise as follows: (a) the attractive term is due to the fact that induced dipole-dipole interactions, which scale as $1/r^6$, are the dominant attractive force on the molecular scale, and (b) the repulsive term is an empirical fit to experimental results where the repulsion is believed to arise predominantly from the Pauli exclusion principle [27]. We will use the constant c_{ij} to tune the strength of the attractive portion of the potential (the pure Lennard-Jones (LJ) potential normally takes $c_{ij} = 1$). For LJ materials where the fluid-solid and fluid-fluid interactions use the parameters c_{fs} and c_{ff} respectively, it has been shown that the contact angle can be calculated using

$$\cos\theta = 2\frac{\rho_{\mathrm{s}} c_{\mathrm{fs}}}{\rho_{\mathrm{f}} c_{\mathrm{ff}}} - 1, \tag{1.25}$$

where ρ_{s} and ρ_{f} are the densities of the solid and liquid, respectively [28] (see Fig. 1.6). This is done through the use of Laplace's[11] estimate of surface tension [25], which states that if one knows the interaction energy between two phases, let them be A and B, then the surface tension is [28]

$$\gamma_{\mathrm{AB}} = -\frac{1}{8}\rho_{\mathrm{A}}\rho_{\mathrm{B}} \int_{r_0}^{\infty} r U_{\mathrm{AB}}(\boldsymbol{r}) d\boldsymbol{r}, \tag{1.26}$$

---

[10] Thomas Young (1773-1829) was an English scientist who is sometimes referred to as "the last person to know everything". A master of languages, by the age of fourteen he knew Greek, Latin, French, Italian, Hebrew, Chaldean, Syriac, Samaritan, Arabic, Persian, Turkish and Amharic and introduced the term *Indo-European Languages* to characterize the super-family of related languages that stretch from Europe to India. His many contributions to science include the double-slit experiment, experiments on material stiffness and colour theory and he is commemorated by Young's modulus and Young's equation, among others [24].

[11] Pierre-Simon, Marquis de Laplace (1749-1847) was a French mathematician and astronomer who applied the study of mechanics (pioneered by figures such as Newton) to the celestial bodies in his work *Mécanique céleste*. He also made contributions widely in other fields of mathematics, physics and probability theory and has his namesake on many items including the Laplace equation (which he discovered), the Laplace transform and the Laplacian differential operator. His minor discovery of capillary action was integral in the development of the theory of fluid-solid interactions [29].

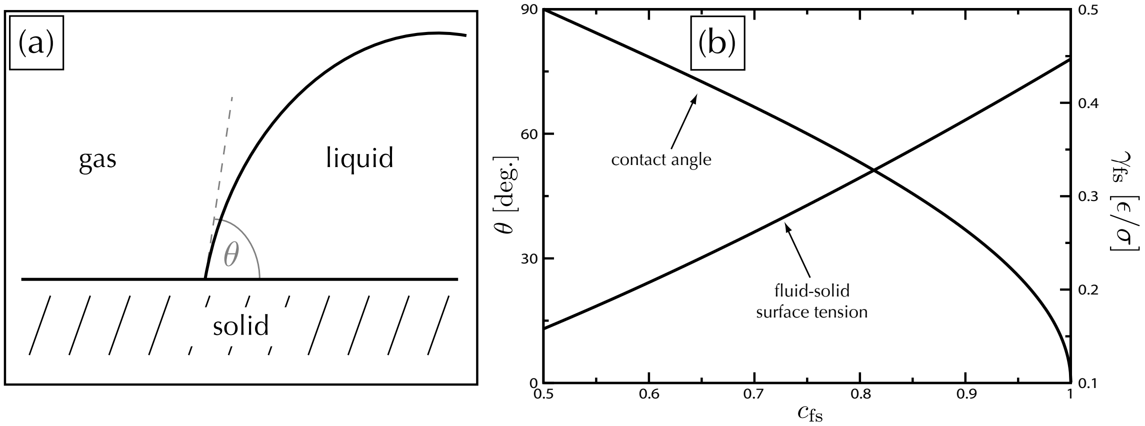

FIGURE 1.6 (a) Schematic showing a three-phase system and how the contact angle θ is defined. (b) Contact angle of a three-phase system with $\rho_{\rm s} = \rho_{\rm f}$ and $c_{\rm ff} = 1$ as a function of $c_{\rm fs}$. Also shown is the surface tension of a fluid-solid interface in a two-dimensional system with $\rho_{\rm f} = \rho_{\rm s} = 0.8/\sigma^2$ as a function of $c_{\rm fs}$. In two dimensions we are not dealing with a surface tension but actually a *line tension*: energy per unit length. Clearly, we can see in both cases that the properties of the solid-fluid system can be changed significantly by tuning $c_{\rm fs}$.

where r_0 is the collision radius: $U(r_0) = 0$. The integral is performed over all dimensions of space over the radial range specified. In this fashion, for Lennard-Jones interactions, only the attractive portion of the potential contibutes to the surface tension. If we consider the fluid-solid interface in a two-dimensional system, with the Lennard-Jones constant $c_{\rm fs}$, then the surface tension can be calculated to be

$$\gamma_{\rm fs} = \frac{2\pi}{9}\rho_{\rm s}\rho_{\rm f}\epsilon\sigma^3 c_{\rm fs}^{3/2}. \tag{1.27}$$

In other words, the surface tension increases with the constant $c_{\rm fs}$, which controls the attractive portion of the Lennard-Jones potential. We use a two-dimensional model since that is what we will be working with in the papers presented in this thesis. See Fig. 1.6 for a graphical representation of the dependence of $\gamma_{\rm fs}$ on $c_{\rm fs}$.

Molecular Dynamics Simulations

In order to model fluids and rigid walls, which we will use to contruct our nanochannel simulations, we will use the Molecular Dynamics (MD) algorithm. Molecular Dynamics allows one to examine the behaviour of an assembly of particles on the molecular scale as a collection of interacting particles. This is at the base of the MD method: we model fluids and solids as collections of many beads that interact through a pair potential. We will not take the beads as individual molecules or atoms of a particular material but rather they will be general representations of an element of the material (fluid or solid). This type of *coarse-grained* MD allows for the study of systems on larger length and time scales than *atomistic* MD. Our beads will interact through the Lennard-Jones[12] potential (presented above in the section on Capillarity Theory). For appropriate choices of the free parameters (which includes the mass of the particles, m, in addition to σ and ϵ), MD simulations using this potential have reasonably predicted the liquid properties of Argon [31]. For computational efficiency, we will cut off the potential such that $U(r > r_\mathrm{C}) = 0$ and shift the remaining potential up by a constant ϵ_0 so that it is continuous:

$$U_{ij} = \begin{cases} 4\epsilon\left[\left(\frac{\sigma}{r_{ij}}\right)^{12} - c_{ij}\left(\frac{\sigma}{r_{ij}}\right)^{6}\right] + \epsilon_0 & \text{, if } r_{ij} \leq r_c \\ 0 & \text{, if } r_{ij} > r_c \end{cases} \tag{1.28}$$

where $\epsilon_0 = -U(r_\mathrm{c})$ [26] (see Fig. 1.7). This is done for two reasons. First, it limits the number of particles involved in each force calculation to a limited region. Second, usually systems in MD simulations have periodic boundary conditions and so an infinite potential that wraps around the boundary would be problematic. Essentially, we ignore long-range interactions. There are two common choices for the cutoff radius: $r_\mathrm{c} = 2^{1/6}\,\sigma$ and $r_\mathrm{c} = 2.5\,\sigma$. The former choice cuts off the potential at its minimum so all that remains is the repulsive core. This essentially models the beads as soft spheres but is inadequate if properties involving the attractive nature of the beads are required. The latter choice cuts the potential along its attractive tail and allows the model to retain both repulsive and attractive properties of the system. Throughout this work we have chose $r_\mathrm{c} = 2.5\,\sigma$ as our cutoff radius. For systems where both the attractive and repulsive portions of the potential are considered, Meier *et al.* have shown that the particle ensemble exhibits phase changes as well as the expected interdependence of density, pressure, temperature, viscocity and diffusion coefficient [32, 33, 34] (see Fig. 1.7 for details on the LJ potential with different cutoffs).

The MD algorithm consists of calculating the trajectories of the participating particles, taking into account all internal and external forces. This is done by integrating Newton's equations of motion in the presence of the internal forces, induced by the LJ potential, and externally applied

---

[12] Sir John Edward Lennard-Jones (1894-1954) was a mathematician who held prominent chairs in Bristol and Cambridge, England. He was mainly interested in atomic and molecular structure about which he published celebrated works regarding intermolecular forces and valency. Some regard him as the father of computational chemistry and the Lennard-Jones potential, often used in Molecular Dynamics and Monte Carlo simulations, is named in his honour [30].

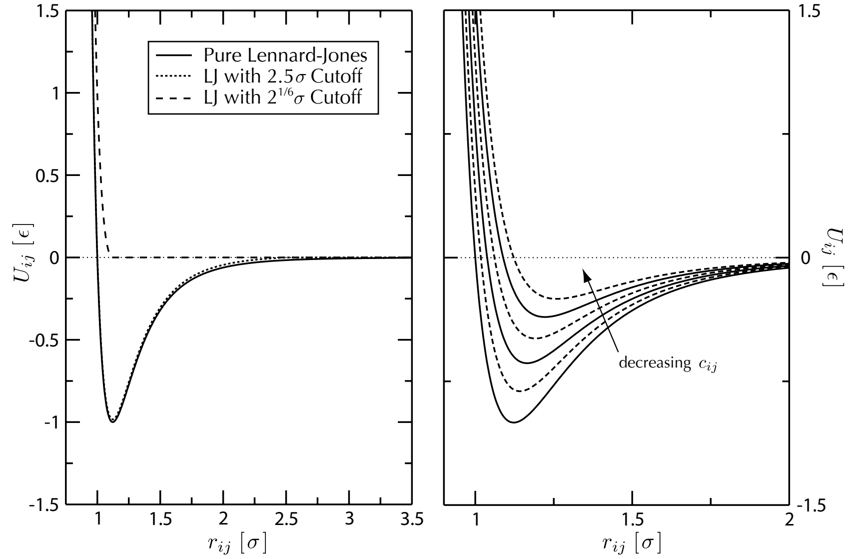

FIGURE 1.7 The Lennard-Jones potential is shown on the left with no cutoff (solid line), $r_\mathrm{c} = 2^{1/6}\ \sigma$ (dashed line) and $r_\mathrm{c} = 2.5\ \sigma$ (dotted line). We can clearly see that if the potential is cut off at $2.5\ \sigma$ it is very close to the full LJ. On the right we see the full LJ potential for various values of c_{ij} ranging from 1 to 0.5. As we decrease c_{ij} (the strength of the attraction) we raise the minimum of the potential and move it outwards. This can be used to simulate hydrophobicity between solids and fluids or immiscibility between fluids.

forces:

$$\frac{\partial \boldsymbol{r}_i}{\partial t} = \frac{\boldsymbol{p}_i}{m_i} \tag{1.29}$$

$$\frac{\partial \boldsymbol{p}_i}{\partial t} = -\nabla U_\mathrm{tot} + \boldsymbol{F}_\mathrm{ext}. \tag{1.30}$$

where $\boldsymbol{r}_i$ and $\boldsymbol{p}_i$ are the position and momentum of the i^th particle and m_i is its mass. U_tot is the total effective potential felt by particle i, calculated from all other particles within the interaction range and $\boldsymbol{F}_\mathrm{ext}$ is an external force. These equations are integrated by approximating the time derivatives with finite differences. The equations of motion are initialized by placing the particles according to some lattice structure and intitializing the momentum randomly according to the Maxwell distribution such that the mean corresponds to a desired thermal energy (temperature). The system is allowed to equilibrate for several steps before external forces are applied. After, the system has reached a steady state data collection is commenced.

Oftentimes, keeping the temperature constant at the desired value can be a problem. This can be particularly problematic if, as in our case, one is pumping energy into the system by applying an external force which is then dissipated into heat. There are various methods used to thermostat the system such as coupling the particles to an additional degree of freedom that acts as a heat resevoir (the Nosé-Hoover thermostat [35, 36]) or by coupling the system to friction and stochastic forces through the Langevin[13] equations (the stochastic dynamics Langevin thermostat (SD) [38]). In this study, we have opted to use a thermostat based on the principles of Dissipative Particle Dynamics (DPD) [39]. This thermostat adds two forces to Eq. 1.30, a damping force, $\boldsymbol{F}_i^{\mathrm{D}}$, and a random force, $\boldsymbol{F}_i^{\mathrm{R}}$. These forces are expressed as follows:

$$\boldsymbol{F}_i^{\mathrm{D}} = \sum_{j\neq i} \boldsymbol{F}_{ij}^{\mathrm{D}} \quad , \quad \boldsymbol{F}_{ij}^{\mathrm{D}} = -\zeta w(\hat{r}_{ij} \cdot \boldsymbol{u}_{ij})\hat{r}_{ij} \tag{1.31}$$

$$\boldsymbol{F}_i^{\mathrm{R}} = \sum_{j\neq i} \boldsymbol{F}_{ij}^{\mathrm{R}} \quad , \quad \boldsymbol{F}_{ij}^{\mathrm{D}} = sw\theta\hat{r}_{ij}, \tag{1.32}$$

where θ is a Gaussian white noise variable, $\boldsymbol{u}_{ij} = \boldsymbol{u}_i - \boldsymbol{u}_j$, w is a weighting function (equal to one for $r < r_{\mathrm{c}}$ and zero otherwise) and ζ and s represent the strengths of the forces and are related by

$$s^2 = 2k_{\mathrm{B}}T\zeta. \tag{1.33}$$

In a similar fashion to the SD thermostat, the random and damping forces act along the axis between particles and functions by slowing down particles that are too “hot” and speeding up particles that are too “cold”. Furthermore, this method helps stabilize the numerical method by damping instabilities and also retains Galilean invariance and correct hydrodynamics, which the SD thermostat lacks. It should be noted that the DPD thermostat in its originally proposed form contained errors due to a finite timestep. It has been shown that these errors can be compensated by scaling the applied random force by a factor dependent on the temperature, timestep and parameters of the thermostat [40].

In our review of capillarity theory we mentioned that we can control the interaction between various Lennard-Jones materials by tuning the constant c_{AB} (where A and B are two different species of Lennard-Jones material). We will present two examples that will serve as demonstrations of this mechanism. First, we can simulate fluid immiscibility if we have two fluid species, A and B, with the following property: $c_{\mathrm{AB}} < c_{\mathrm{AA}} = c_{\mathrm{BB}}$. Since the constant c controls the attractive portion of the LJ potential (see Fig. 1.7 for details), this situation results in fluid particles preferring

---

[13] Paul Langevin (1872-1946) was a French physicist who studied in Paris and later at Cambridge under J. J. Thompson. He is remembered for his work on paramagnetism and diamagnetism and their modern interpretations in terms of electrons and atoms. He also worked on ultrasonic sounds using Pierre Curie’s piezoelectric effect. He and Marie Curie supposedly had an affair in 1910 [37].

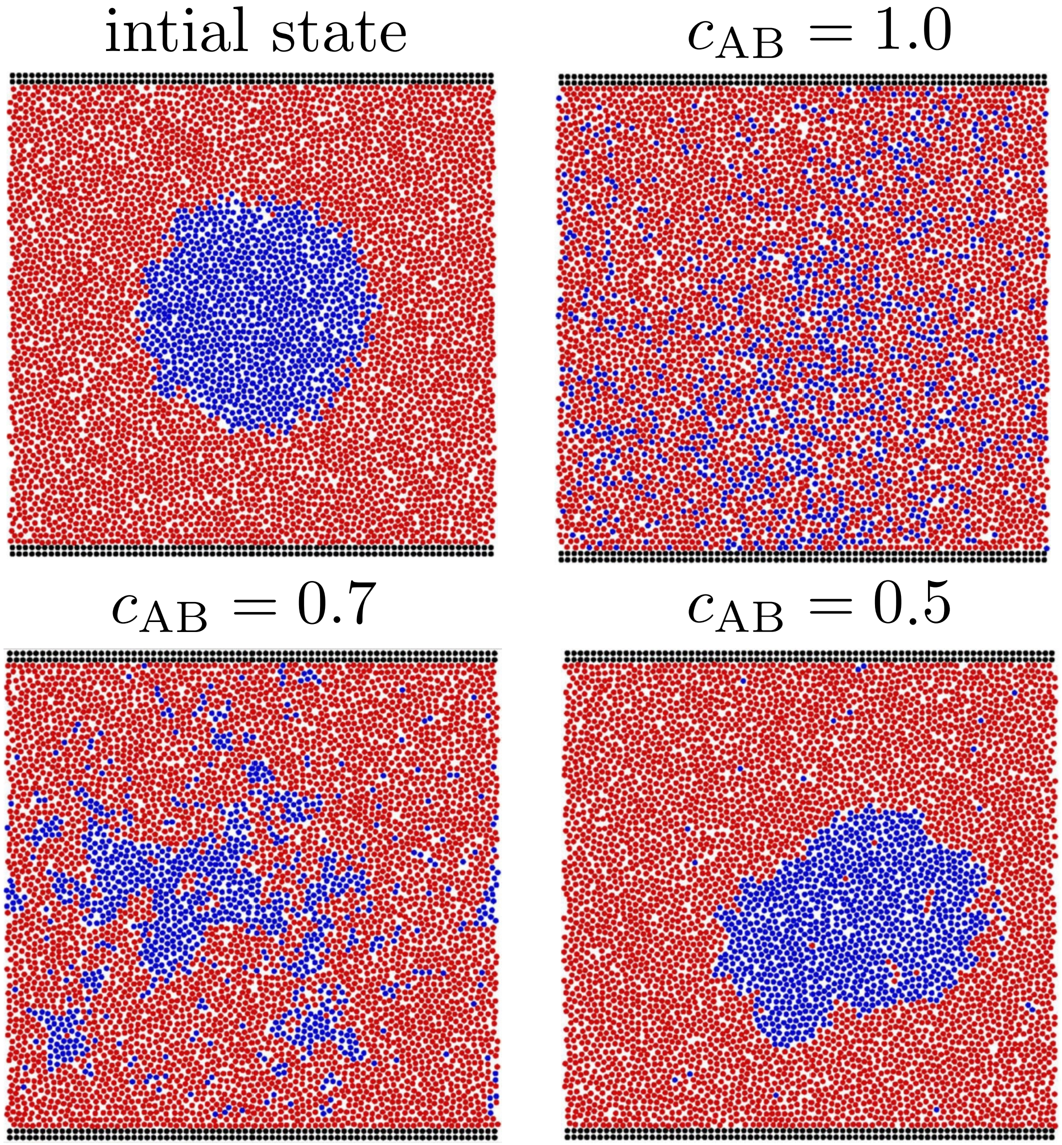

FIGURE 1.8 Molecular Dynamics simulations of two fluid species (A and B, blue and red respectively) and fixed wall particles (shown in black) in a 75 by 75 particle channel. There are periodic boundary conditions along the x direction, all particles interact with the LJ potential, the densities are all $\rho = 0.8/\sigma^2$ and the temperature is kept constant at $k_{\mathrm{B}}T = 1\,\epsilon$. All interactions except between unlike fluid species has the constant $c = 1$ and we set $c_{\mathrm{AB}} \leq 1$. The first frame shows the initial state for all simulations and the other frames are the final state for various simulations. We see that as c_{AB} is decreased from a value of one, the two fluid species become less miscible until there is nearly no mixing between them at all.

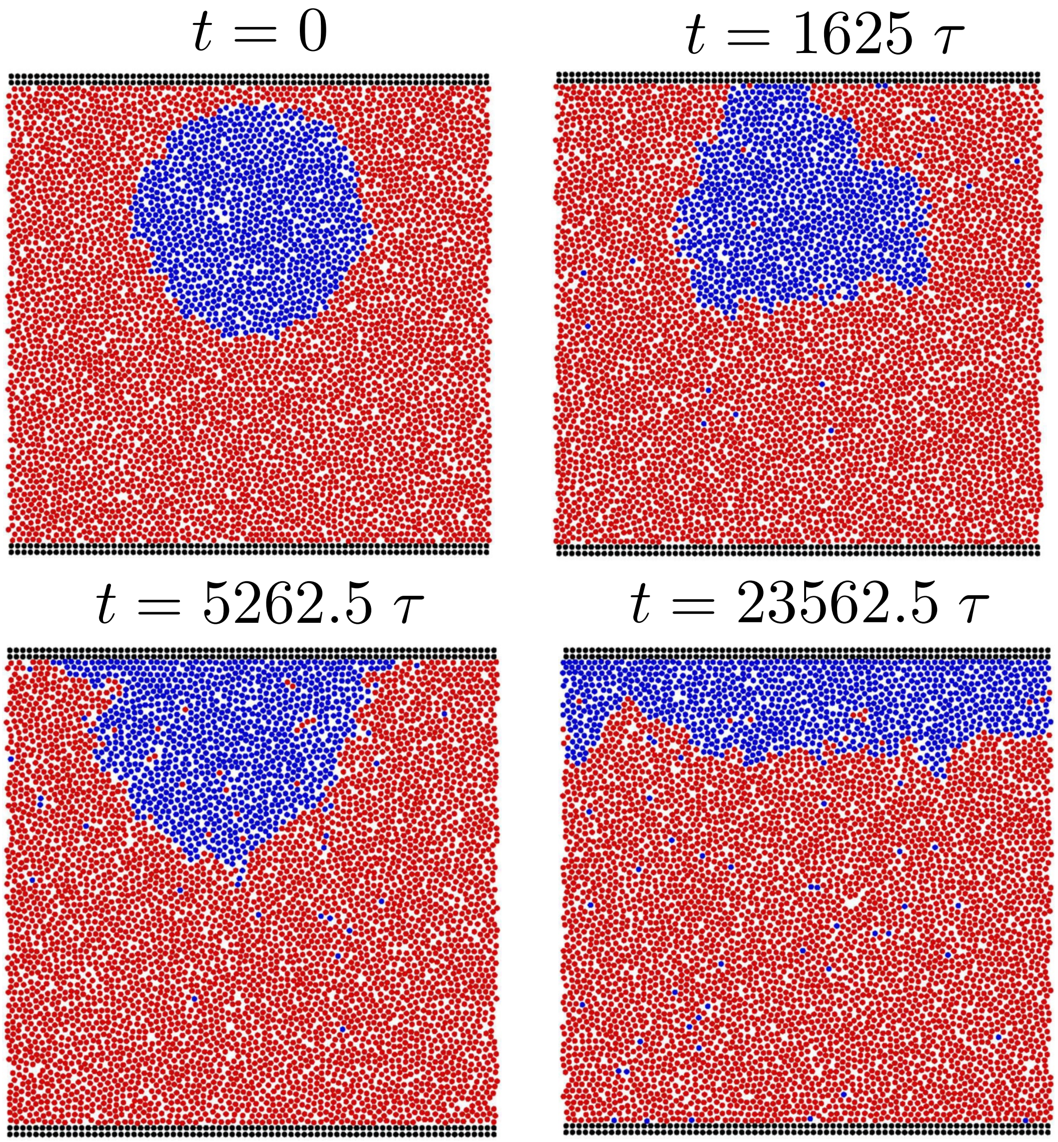

$t = 0$

$t = 1625\ \tau$

$t = 5262.5\ \tau$

$t = 23562.5\ \tau$

FIGURE 1.9 Molecular Dynamics simulations of two fluid species (A and B) and fixed wall particles in a 75 by 75 particle channel. There are periodic boundary conditions along the x direction, all particles interact with the LJ potential, the densities are all $\rho = 0.8/\sigma^2$ and the temperature is kept constant at $k_{\mathrm{B}}T = 1\ \epsilon$. The fluids are immiscible with $c_{\mathrm{AA}} = c_{\mathrm{BB}} = 1$ and $c_{\mathrm{AB}} = 0.5$. The wall has a preferential attraction to fluid A with the parameters: $c_{\mathrm{wA}} = 1.2$ and $c_{\mathrm{wB}} = 0.8$. The frames show different points in time during the simulation. We see that the droplet of fluid type A finds the wall through random motion and proceeds to wet it. The final state is fluid A completely adsorbed to the wall and wrapping around the periodic boundary conditions.

to be near particles of the same type since the attraction will be larger than for a particle of unlike type. Simulations were performed on a small channel of 75 by 75 particles at density $\rho = 0.8/\sigma^2$ and were run for 1×10^6 timesteps at $\Delta t = 0.005\,\tau$. Figure 1.8 shows that as c_{AB} is decreased the fluids become more immiscible. Using this technique it would be possible to study the mixing properties of immiscible fluids (such as oil and water) in microchannels.

A second example shows the preferential wetting of wall particles by a fluid species. We have two immiscible fluids, A and B, with parameters $c_{\mathrm{AA}} = c_{\mathrm{BB}} = 1$ and $c_{\mathrm{AB}} = 0.5$. Furthermore, fluid type A is preferentially attracted to the wall with wall-fluid interactions $c_{\mathrm{wA}} = 1.2$ and $c_{\mathrm{wB}} = 0.8$. The channel properties (size, density, etc.) are the same as those used above and the simulation is run run for 5×10^6 timesteps with $\Delta t = 0.005\,\tau$. The results, shown in Fig. 1.9, clearly show that fluid A wets the wall after it makes contact and in the steady state results in the fluid completely adsorbed to the wall. We can control the degree of wetting by the value of the wall-fluid interaction constants. This technique will be used to control fluid slip along microchannel walls.

Presentation of the Thesis

The main chapters of the thesis, Chapters 2 and 3 (affectionately dubbed “spinning” and “mixing”, respectively), are manuscripts for articles that have been submitted to journals. These articles are the culmination of most the work I have done during the course of my M. Sc. studies. Here is a list of the articles along with abstracts:

- **1)** E. C. J. Oliver and G. W. Slater, *Forced Rotational Motion of Fluid in a Cavity: A Molecular Dynamics Study*, submitted to *The Journal of Chemical Physics*, July 14 2006.

  We have performed Molecular Dynamics simulations of microscale laminar flow in a coupled channel-cavity system in order to explore forced rotation of the fluid in the cavity by the flow in the channel. These simulations have reproduced experimental observations well. We have extended our treatment to explore how modifying the surface tension (hydrophobicity) along the walls of the channel affects the slip length. By applying this to the coupled channel-cavity system we can affect the effeciency of spin generation in the cavity fluid. For a constant flow rate, we find that we can generate a larger spin in the cavity by increasing the hydrophobicity of the walls (using two possible schemes) by about 80% using this method.

- **2)** E. C. J. Oliver and G. W. Slater, *A Theoretical and Molecular Dynamics Study of Mixing in Microchannels with Obstacles*, submitted to *Journal of Micromechanics and Microengineering*, July 26 2006.

  A system consisting of two miscible fluids in a microchannel under laminar flow has been examined with theoretical techniques and simulated using Molecular Dynamics (MD). We have applied the theory of diffusion to predict the displacement of particles as they diffuse across a channel perpendicular to a Poiseuille flow. Using MD simulations, we have studied the presence of obstacles in the flow path and shown, contrary to what has been proposed recently, that they do not significantly increase mixing efficiency in microchannels. Their effect is such that (i) the flow profile becomes flattened within a certain range of the obstacles and (ii) the fluid flow acquires lateral components and so follows a sinuous path through the channel. From our theoretical predictions and numerical simulations, we show that the former results in increased levels of partial mixing when compared to a system lacking obstacles. However, obstacles do not reduce the length required for full mixing. Furthermore, the second effect increases contact between the fluids but the mixing increase is negligible.

Statement of Originality and Research Performed

As far as I am aware, excepting portions of the review presented in this introduction, the material presented in this thesis is original. It is the product of my own research with the supervision and input of my supervisor. I have not reproduced or taken other's work without giving credit where it is due.

I have contributed to the following presentations during the course of my Master's degree:

- **E. C. J. Oliver**. *Forced Rotational Motion of a Fluid in a Nanocavity: A Molecular Dynamics Study*. Ottawa Carleton Institute for Physics Spring Graduate Student Seminar, Ottawa, ON, May 2006

- **G. W. Slater**, Frédéric Tessier and Eric C. J. Oliver. *Polymers, electrophoresis and electroosmotic flows in nanochannels: A molecular dynamics study*. 231st American Chemical Society National Meeting, Atlanta, GA, March 2006.

- **E. C. J. Oliver** and G. W. Slater. *Enhanced Fluid Mixing in Nanochannels: A Molecular Dynamics Study* (poster). American Physical Society March Meeting, Baltimore, MD, March 2006.

- **E. C. J. Oliver** and G. W. Slater. *Mixing of Fluids in Nanochannels*. American Physical Society March Meeting, Los Angeles, CA, March 2005.

In addition to research relating to what is presented here, during my Master's degree I have also worked on the following side projects and interests:

- Fluid immiscibility and mixing of immiscible fluids in Molecular Dynamics simulations by tuning the Lennard-Jones interaction potential.

- Preferential wetting and droplet formation of binary fluid mixtures in Molecular Dynamics simulations inside a microchannel by tuning the Lennard-Jones potential (simulations of results presented by Balazs *et al* in Ref. [41]).

- Enhanced fluid mixing in microchannels by modifications to the channel geometry (bumps, ridges, etc.) and chemistry (hydrophobicity, hydrophilicity) using Molecular Dynamics simulations.

- Dependence of polyelectrolyte electrophoretic mobility on confinement in capillaries. This work was in response to recent experimental observations by Bernard Tinland, CNRS, Marseilles, France (personal communication with the Slater research group).

- Dependence of polyelectrolyte electrophoretic mobility on conformation. Generally, mobility is assumed to be conformation independent although there have been no studies demopnstrating it. Molecular Dynamics simulations have produced promising results and will hopefully result in a publication. (This work is in collaboration with fello Masters in Physics student Martin Bertrand, also of the Slater Group).

References

[1] TM Squires, SR Quake. *Microfluidics: Fluid physics at the nanoliter scale*, ***Rev. Mod. Phys.*** **77**, 977–1026 (2005).

[2] JCT Eijkel, A Berg. *Nanofluidics: what is it and what can we expect from it?*, ***Microfluid. Nanofluid.*** **1**, 249–267 (2005).

[3] P Tabeling. *Introduction to Microfluidics*. Oxford University Press, USA, Oxford (2006).

[4] JP Shelby, DSW Lim, JS Kuo, DT Chiu. *High radial acceleration in microvortices*, ***Nature*** **425**, 38 (2003).

[5] JP Shelby, DT Chiu. *Controlled rotation of biological micro- and nano-particles in microvortices*, ***Lab Chip*** **4**, 168–170 (2004).

[6] JP Shelby, SA Mutch, DT Chiu. *Direct manipulation and observation of the rotational motion of single optically trapped microparticles and biological cells in microvortices*, ***Anal. Chem.*** **76**, 2492–2497 (2004).

[7] H Wang, P Iovenitti, E Harvey, S Masood, R Deam. *Mixing of liquids using obstacles in microchannels*, ***Proceedings of SPIE*** **4590**, 204 (2001).

[8] H Wang, P Iovenitti, E Harvey, S Masood. *Optimizing layout of obstacles for enhanced mixing in microchannels*, ***Smart Mate. and Struct.*** **11**, 662–667 (2002).

[9] “Robert Brown (Botanist)”. *Wikipedia*, ***http://en.wikipedia.org/wiki/Robert_Brown_%28botanist%29*** (accessed 20 July 2006).

[10] RM Mazo. *Brownian Motion: Fluctuations, Dynamics and Applications*. Oxford University Press, Oxford (2002).

[11] “Albert Einstein”. *Wikipedia*, ***http://en.wikipedia.org/wiki/Einstein*** (accessed 20 July 2006).

[12] J Crank. *The Mathematics of Diffusion*. Oxford University Press, Oxford second edition, (1995).

[13] “Carl Friedrich Gauss”. *Wikipedia*, ***http://en.wikipedia.org/wiki/Carl_Friedrich_Gauss*** (accessed 20 July 2006).

[14] “Claude-Louis Navier”. *Wikipedia*, ***http://en.wikipedia.org/wiki/Navier*** (accessed 19 July 2006).

[15] “George Gabriel Stokes”. *Wikipedia*, ***http://en.wikipedia.org/wiki/George_Gabriel_Stokes*** (accessed 19 July 2006).

[16] J Koplik, JR Banavar. *Continuum deductions from molecular hydrodynamics*, ***Annu. Rev. Fluid Mech.*** **27**, 257–292 (1995).

[17] PK Kundu, IM Cohen. *Fluid Mechanics*. Academic Press, San Diego, CA second edition, (2002).

[18] “Osbourne Reynolds”. *Wikipedia*, ***http://en.wikipedia.org/wiki/Osborne_Reynolds*** (accessed 19 July 2006).

[19] “William Froude”. *Wikipedia*, ***http://en.wikipedia.org/wiki/William_Froude*** (accessed 19 July 2006).

[20] “Jean Claude Eugene Peclet”. *Wikipedia*, ***http://en.wikipedia.org/wiki/Jean_Claude_Eugene_Peclet*** (accessed 19 July 2006).

[21] EM Purcell. *Life at low reynolds number*, ***Am. J. Phys.*** **45**, 3–11 (1977).

[22] "Jean Louis Marie Poiseuille". *Wikipedia*, ***http://en.wikipedia.org/wiki/Poiseuille*** (accessed 20 July 2006).

[23] CH Choi, JA Westin, KS Breuer. *Apparent slip flows in hydrophilic and hydrophobic microchannels*, ***Phys. Fluids*** **15**, 2897–2902 (2003).

[24] "Thomas Young (scientist)". *Wikipedia*, ***http://en.wikipedia.org/wiki/Thomas_Young_%28scientist%29*** (accessed 20 July 2006).

[25] JS Rowlinson, B Widom. *Molecular Theory of Capillarity*. Oxford University Press, Oxford (1987).

[26] DC Rapaport. *The Art of Molecular Dynamics Simulation*. Cambridge University Press, Cambridge (1995).

[27] C Kittel. *Introduction to Solid State Physics*. John Wiley & Sons, New York seventh edition, (1996).

[28] JL Barrat, Lydéric Bocquet. *Large slip effect at a nonwetting fluid-solid interface*, ***Phys. Rev. Lett.*** **82**, 4671 (1999).

[29] "Pierre-Simon Laplace". *Wikipedia*, ***http://en.wikipedia.org/wiki/Laplace*** (accessed 20 July 2006).

[30] "Sir John Lennard-Jones". *Wikipedia*, ***http://en.wikipedia.org/wiki/Sir_John_Lennard-Jones*** (accessed 21 July 2006).

[31] MP Allen, DJ Tildesley. *Computer Simulation of Liquids*. Oxford University Press, Oxford (1987).

[32] K Meier, A Laesecke, S Kabelac. *A Molecular Dynamics Simulation Study of the Self-Diffusion Coefficient and Viscosity of the Lennard–Jones Fluid*, ***Int. J. Thermophys.*** **22**, 161–173 (2001).

[33] K Meier, A Laesecke, S Kabelac. *Transport coefficients of the Lennard-Jones model fluid. I. Viscosity*, ***J. Chem. Phys.*** **121**, 3671 (2004).

[34] K Meier, A Laesecke, S Kabelac. *Transport coefficients of the Lennard-Jones model fluid. II Self-diffusion*, ***J. Chem. Phys.*** **121**, 9526 (2004).

[35] WG Hoover. *Canonical dynamics: Equilibrium phase-space distributions*, ***Phys. Rev. A*** **31**, 1695–1697 (1985).

[36] S Nosé. *An extension of the canonical ensemble molecular dynamics method*, ***Mol. Phys.*** **57**, 187–191 (1986).

[37] "Paul Langevin". *Wikipedia*, ***http://en.wikipedia.org/wiki/Paul_Langevin*** (accessed 20 July 2006).

[38] T Schneider, E Stoll. *Molecular-dynamics study of a three-dimensional one-component model for distortive phase transitions*, ***Phys. Rev. B*** **17**, 1302–1322 (1978).

[39] T Soddeman, B Dünweg, K Kremer. *Dissipative particle dynamics: A useful thermostat for equilibrium and nonequilibrium molecular dynamics simulations*, ***Phys. Rev. E*** **68**, 046702–1–8 (2003).

[40] EAJF Peters. *Elimination of time step effects in dpd*, ***Europhys. Lett.*** **66**, 311–317 (2004).

[41] AC Balazs, R Verberg, CM Pooley, O Kuksenok. *Modelling the flow of complex fluids through heterogeneous channels*, ***Soft Matter*** **1**, 44 (2005).

2

Project I: Spinning

E. C. J. Oliver and G. W. Slater
Forced Rotational Motion of Fluid in a Cavity: A Molecular Dynamics Study
Status: submitted to *The Journal of Chemical Physics*, July 14 2006

Forced Rotational Motion of Fluid in a Cavity: A Molecular Dynamics Study

Eric C. J. Oliver* and Gary W. Slater†

Department of Physics,

University of Ottawa,

150 Louis-Pasteur, Ottawa,

ON, Canada, K1N 6N5

(Dated: July 30, 2006)

Abstract

We have performed Molecular Dynamics simulations of microscale laminar flow in a coupled channel-cavity system in order to explore forced rotation of the fluid in the cavity by the flow in the channel. These simulations have reproduced experimental observations well. We have extended our treatment to explore how modifying the surface tension (hydrophobicity) along the walls of the channel affects the slip length. By applying this to the coupled channel-cavity system we can affect the effeciency of spin generation in the cavity fluid. For a constant flow rate, we find that we can generate a larger spin in the cavity by increasing the hydrophobicity of the walls (using two possible schemes) by about 80% using this method.

I. INTRODUCTION

The miniaturization of fluidic systems to the micro- and nano-scale is proving its usefuleness across the laboratory spectrum and there is much research on the physics occuring on these scales[1]. Recent developments are progressing towards the point where all operations on microfluidic systems will be done “on-a-chip” and laboratories will use micro-devices that can perform operations such as chemical reactions, mixing, molecular separations and other basic functions.

An example of one such function we consider is the centrifugation of a small quantity of fluid. An experimental situation has already been devised by Shelby *et al.*[2] where a small fluid-filled cavity approximately 50 μm across has been forced into rotation by coupling it to pressure-driven flow in a channel of similar cross-section dimensions and a length of 150 μm. With average fluid velocities of up to 45 m/s in the channel, rotational velocities as high as 12 m/s at a distance of 12 μm from the core of the resulting vortex were observed. This corresponds to a radial acceleration of 1.4×10^6 g! It was also observed that the rate of fluid rotation in the cavity increases with the flow rate in the channel. In later experiments, this group has demonstrated a practical use for a device operating on this principle by placing a biological cell in the cavity and using the rotational flow to test the effects of stress on the cell[3,4]. Other uses for such a device that will be practical in microfluidic systems are apparent. Such applications could include the centrifugation and separation of a multi-component fluid mixture and the possibilities of mixing or dilution of a solution using rotating cavity fluid and possible mass exchange between the cavity and the channel.

In this paper, we simulate this experimental system using a Molecular Dynamics computational algorithm. The basic physics that were observed experimentally are reproduced in our simulations. In addition, we explore avenues to enhance the efficiency of spin generation in the cavity fluid by changing the surface tension between the solid wall and the fluid. To maximize the radial acceleration in the microcavity, surface tension was minimized and thus the fluid slips along the wall near the coupling region with the cavity. We also look to predictions from macroscopic hydrodynamics in situations where experimental results give no indication of what is expected.

This paper is organized in four sections. First, we will present the fluidic system along with the relavent hydrodynamic theory. Then, we will review our Molecular Dynamics sim-

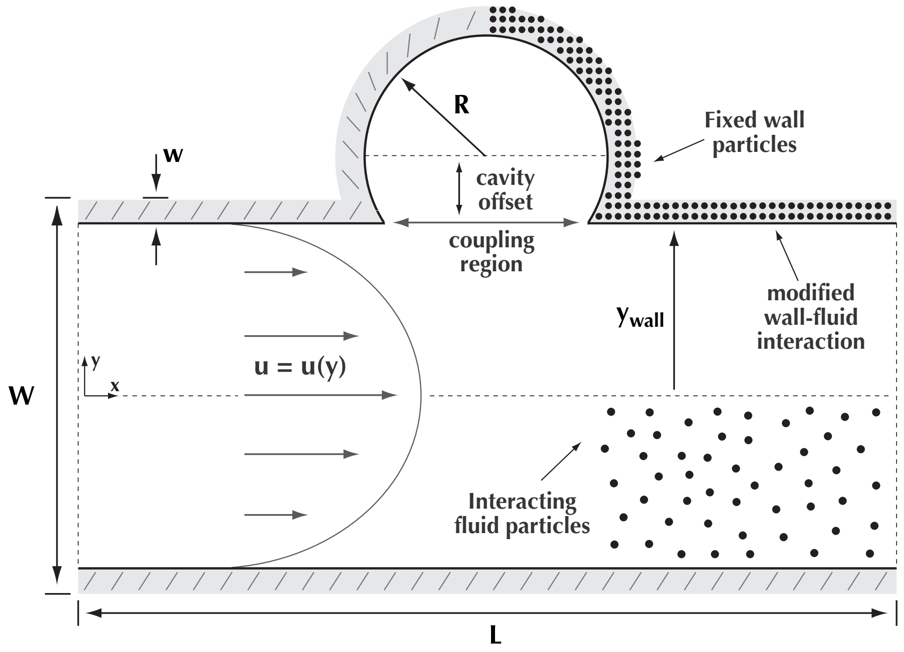

FIG. 1: Schematic of the coupled channel-cavity system. The channel is $W = 55.9\ \sigma$ in width (including the walls of thickness $w = 2.23\ \sigma$) and $L = 134.16\ \sigma$ in length. The circular cavity has a radius $R = 12.3\ \sigma$ and is offset from the position of the channel wall by $11.18\ \sigma$. A Poiseuille flow is generated in the channel which is coupled to the cavity and drives rotational motion of the fluid in the cavity. Also presented here are representations of the wall and fluid in terms of interacticting particles which are used in the Molecular Dynamics simulations.

ulation method and how we apply it to our system. The last two sections deal with the simulation results. In the third section, we discuss the channel alone, such as its hydrodynamic properties and measurements of slip length. Finally, we present the cavity results, including measurements of its spin and how we can increase the efficiency of spin generation.

II. SYSTEM

The system we are modelling is a simplified version of the experimental setup used by Shelby *et al.*[2–4] and consists of a narrow channel with flow driven by a pressure gradient which is coupled to a small circular cavity situated along one of the channel walls (see Fig. 1 for details). Viscous coupling is achieved through a small opening in the upper wall which allows contact and thus transfer of momentum between the fluid in the channel and the cavity. The problem essentially consists of the classic lid-driven cavity[5,6] but with the driving lid replaced by coupling the cavity to the fluid flow in the channel. The width of the opening which serves as the coupling region is chosen to be on the order of the radius of the cavity so that there can be substantial channel-cavity coupling but not reduce the cavity to a mere indentation along the wall. If the channel flow is nonzero along the upper wall, then the fluid in the cavity will be dragged along its outer edge and driven into rotational motion. A simple property of the system is that the tangential velocity, u_{t}, in the cavity, and thus the radial acceleration, a_{r}, is limited by the fluid flow in the coupling region: $u_{\mathrm{t}} \leq u_{\mathrm{wall}}$, where u_{wall} is the fluid velocity at the wall. With a circular vortex generated in the cavity of radius R this implies a maximum radial acceleration $a_{\mathrm{r}} \leq u_{\mathrm{wall}}^2/R$.

We will model the system in two dimensions for the following reasons: efficient computation and simplicity without loss of essential physics for comparing the results to experiments and three-dimensional simulations. Essentially, we are implying that our results should hold for systems which are very large in the z-direction (perpendicular to the figure) such that we are observing the physics of a single slice parallel to the xy-plane. The physics within each slice will be very similar if not identical and thus by modelling in only two dimensions we can recover the dynamics within one of these slices.

As is well known, flow is laminar in systems with low Reynolds numbers (for $\mathrm{Re} \lesssim 10^3$). If the fluid is confined by two plates parallel to the xz-plane positioned at $\pm y_0$ and is driven by an external acceleration g in the x-direction then the resulting Poiseuille flow assumes the following quadratic profile[7]:

$$u(y) = \frac{\rho_0 g}{2\eta}\left(y_0^2 - y^2\right), \tag{1}$$

where η is the shear viscosity (or dynamic viscosity, sometimes denoted by μ) of the fluid and ρ_0 is the average density of fluid. Note that more commonly, Poiseuille flow is generated by applying a pressure gradient dp/dx. In this case, the form of the flow profile will be the same as Eq. 1 except with the substitution of $\rho_0 g = -dp/dx$.

The Poiseuille velocity profile is such that the velocity vanishes at the walls. This is called the *no-slip* boundary condition, a common assumption used in continuum fluid dynamics. In reality, depending on the wall-fluid interaction and the external force or pressure difference, there can be a small amount of slip at the wall. We can characterize the extent of the slip using the *slip length*, which is the distance from the wall where the velocity profile is extrapolated to zero.

III. SIMULATION METHOD

In order to simulate the system described in Section II, we use Molecular Dynamics (MD) computer simulations which allow us to resolve the processes that occur on the molecular scale; in this regime the precepts of macroscopic fluid dynamics may no longer hold. As a side note, it has been shown that the predictions of continuum hydrodynamics are recovered from MD within a few particle layers[8], a claim upheld by the smooth Poiseuille-like flow we generate. However, due to the inherently coarse-grained nature of the MD model, we are studying a generic fluid and cannot make claims to the exact system dimensions and parameter values. As will be seen, we observe the structure of the fluid to be based on finite particles and so we are very close to the nanoscale; however, a large portion of the system exists in bulk conditions and reproduces the predictions of macroscopic hydrodynamics. It is possible to reduce the system dimensions so that we observe only the finite structure of the fluid but we will remain in a regime that exhibits both this nanostructure as well as bulk properties.

We model the fluid and wall constituents by using Lennard-Jones (LJ) beads (see Fig. 1 for an example) which interact through the pair potential:

$$U_{ij} = \begin{cases} 4\epsilon \left[\left(\frac{\sigma}{r_{ij}} \right)^{12} - c_{ij} \left(\frac{\sigma}{r_{ij}} \right)^{6} \right] + \epsilon_0 & \text{if } r_{ij} \leq r_{\text{c}} \\ 0 & \text{if } r_{ij} > r_{\text{c}}, \end{cases} \tag{2}$$

between any two particles i and j, where σ and ϵ are constants which set the length and energy scales, respectively. For computational efficiency we have cut off the potential for $r_{ij} > r_{\text{c}} = 2.5\,\sigma$ and shifted the potential up by a small amount $\epsilon_0 = -U(r_{\text{c}})$ to ensure that U is continuous. This is a common choice and retains both the repulsive core and most of the attractive tail of the potential[9]. All parameters herein are quoted in natural MD units: $m = \epsilon = \sigma = 1$ (m is the particle mass) and the unit of time is $\tau = \sqrt{m\sigma^2/\epsilon}$. The particles are initialized on a square lattice with an average density (for both the fluid and the wall) of $\rho_0 = 0.8/\sigma^2$. The temperature is set by initializing the fluid particle velocities about a mean of $k_{\text{B}}T = 1\,\epsilon$ according to the Maxwell distribution and it is kept constant through the use of a thermostat based on the principles of dissipative particle dynamics (DPD)[10]. Care was taken to avoid known timestep issues with this thermostat[11]. The factor c_{ij} in Eq. 2 is a constant, of order one, which controls the strength of the attractive tail of the LJ potential, and we will use it to tune the strength of the wall-fluid interactions. The Newtonian equations of motion for the particles are integrated using the velocity-Verlet algorithm with a timestep of $\Delta\tau = 0.01\,\tau$. The wall particles are kept fixed in position. In many other models the wall particles are kept in a deep potential well and allowed to exchange momentum and energy with the fluid particles. While our choice is less realistic, we are confident it has no effect on the object of this study other than having the thermostat exercising larger influence since the wall particles are unable to cool the fluid by extracting energy. The walls confine the fluid in the y-direction and we impose periodic boundary conditions in the x-direction.

Two types of channels are considered: one with only fluid and channel walls and another with a cavity placed along one of the walls. The size of the channel-only system is $L = 111.8\,\sigma$ by $W = 55.9\,\sigma$ (with two layers of wall particles taking a width $w = 2.23\,\sigma$ of that on each side). This system is used to measure the effect of both the wall-fluid interaction strength and the fluid flow rate on slip length. The size of the system with the cavity extends to $L = 134.16\,\sigma$ long with the 'spin-cavity' placed halfway along down the channel at the upper wall. It is circular with a radius of $R = 12.3\,\sigma$ and its centre is offset by $11.18\,\sigma$ from the fluid-wall interface (see Fig. 1). This allows the cavity to have a localised section of its perimeter open to the flow in the channel. In order to simulate a Poiseuille flow which is created experimentally by a pressure drop along the channel we applied a constant acceleration to all particles in the channel (but not to the particles in the cavity). As will be demonstrated, this creates a flow profile that varies quadratically across the channel as expected according to Eq. 1.

Technically speaking our simulations consist of $N = 5000$ particles for simulations in Section IV (consisting of 4600 fluid particles and 400 wall particles) and $N = 8400$ particles for simulations in Section V (consisting of 5898 fluid particles and 2502 wall particles). The MD algorithm is executed on two 3.4 GHz Intel Pentium 4 CPU with 1 and 2 GB of RAM each. Each simulation takes aproximately one to three days to complete.

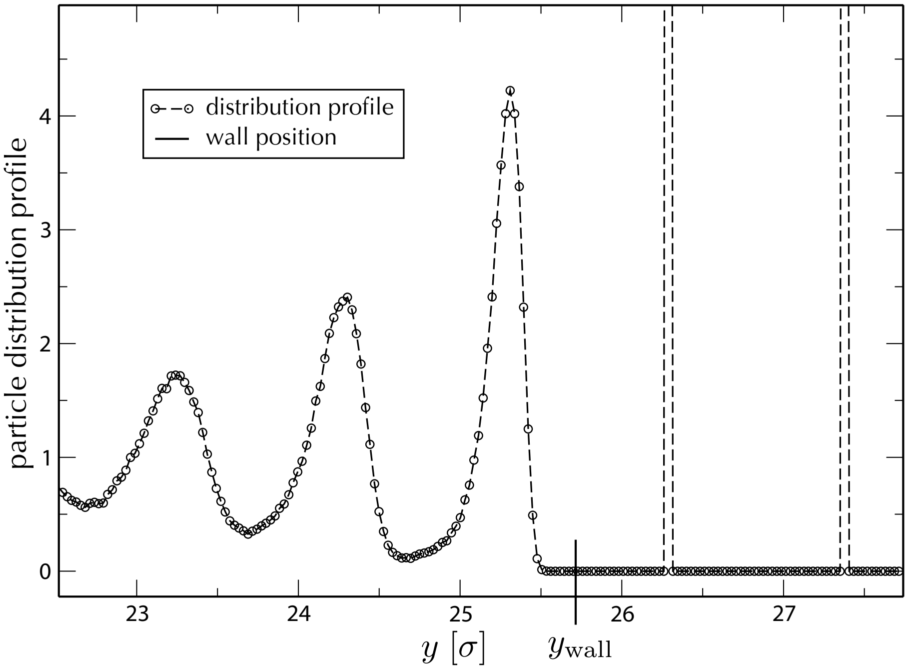

FIG. 2: Particle distribution profile across the channel. Note the presence of the two fixed layers of wall particles at $y = 26.27\,\sigma$ and $y = 27.39\,\sigma$ as well as the layering of the fluid induced by the rigid wall (layers shown peak at $y = 23.24\ \sigma$, $y = 24.30\ \sigma$ and $y = 25.31\ \sigma$). The distribution profile is normalized such that it goes to 1 in the central region of the channel (about $y = 0$, see Fig. 3). The geometric position of the wall, denoted by y_{wall}, is shown in the figure at $y = 25.71\ \sigma$.

IV. RESULTS I: THE CHANNEL PROPERTIES

A. Wall Position

In order to analyse the slip length and measure the velocity at the wall, it is necessary to determine the effective position of the wall surface. Since we have a rough, molecular wall this is not a trivial task. A simple measure is to say that the wall begins at the centre of the first particle of the wall but this is not a robust measure of the wall position as there will be a finite region around the centre of the wall particles where no fluid will ever exist. This is clear from the particle distribution function taken near the wall (see Fig. 2). We opt instead for an unambiguous measure rooted in a sound geometrical argument[12]. The area the fluid occupies can be computed as the number of fluid particles N divided by the mean density,

ρ_0. The area is also equal to the total length of the system (since it is periodic along x), L, times the width of the channel, which can be expressed as twice the distance to the wall $2y_{\text{wall}}$, and so we have the relation $2Ly_{\text{wall}} = N/\rho_0$, from which we can find the wall position:

$$y_{\text{wall}} = \frac{N}{2L\rho_0}. \tag{3}$$

Using $N = 4600$, $L = 111.8\ \sigma$ and $\rho_0 = 0.8/\sigma^2$ we find the result: $y_{\text{wall}} = 25.71\ \sigma$ (which is noted on the particle distribution profile in Fig. 2).

B. Hydrodynamic Properties

We can use the wall position to predict some of the hydrodynamic properties of the fluid. For a basic channel with straight walls and an external acceleration of $g = 0.025\ \sigma/\tau^2$ we recover a nearly quadratic flow profile (see Section IV D for more discussion on this). Using Eq. 1 with the parameters $\rho_0 = 0.8/\sigma^2$ and $y_0 = y_{\text{wall}} = 25.71\ \sigma$, we can perform a fit to the flow profile data and recover the shear viscosity $\eta = 7.08 \pm 0.02\ \sqrt{m\epsilon}/\sigma$. Furthermore, the Reynolds number is defined as

$$\text{Re} = \frac{\rho_0 \bar{u} d}{\eta} \tag{4}$$

where $\bar{u}$ is the fluid velocity averaged over the cross section of width d. Using $d = 2y_{\text{wall}}$ and $\bar{u} \simeq 1\ \sigma/\tau$ (which is appropriate for what we observe) we can calculate the Reynolds number for our flow to be $\text{Re} \simeq 6 \ll 10^3$. This demonstrates that our MD fluid flow simulations are certainly in the laminar regime of the predictions from macroscopic hydrodynamics.

C. Fluid-wall Surface Tension

In order to vary the interaction between the fluid and the wall particles, and consequently the slip length, it is important to have a physical representation for this variation. Essentially, what characterises the fluid-wall interface is the effective interaction energy U_{fw} between the wall and the fluid. From Laplace's formulation for surface tension[13] we can use this to calculate the surface energy density or surface tension. The surface tension, γ_{fw}, can be expressed as[14]

$$\gamma_{\text{fw}} = -\frac{1}{8}\rho_{\text{w}}\rho_{\text{f}} \int_d^\infty r U_{\text{fw}}(\boldsymbol{r}) d\boldsymbol{r} \tag{5}$$

where $U_{\mathrm{fw}}(r)$ is the Lennard-Jones interaction energy between the fluid and wall particles, ρ_{w} and ρ_{f} are the wall and fluid densities and d is the point at which $U_{\mathrm{fw}}(r) = 0$. In two dimensions we have $d\boldsymbol{r} = r d\theta dr$ where we integrate θ over a full circle. From Eq. 2 we can calculate $d = \sigma / c_{\mathrm{fw}}^{1/6}$, and by substituting this and the interaction energyinto Eq. 5, we can derive the surface tension of our interface:

$$\gamma_{\mathrm{fw}} = \frac{2\pi}{9} \rho_{\mathrm{w}} \rho_{\mathrm{f}} \epsilon \sigma^3 c_{\mathrm{fw}}^{3/2}. \tag{6}$$

Thus, the surface tension is expected to increase monotonically (but not linearly) with the strength of attractive interaction, c_{fw}. It should be noted that since we are working in 2D, this is not technically a “surface” tension but actually a “line” tension with units of energy per unit length.

D. Slip Length

As described in Section II, the maximum radial acceleration inside the cavity is limited by the fluid velocity at the channel-cavity interface. If the applied acceleration, g, of the fluid is increased we would expect the velocity at the wall to increase accordingly. Thus, as is observed experimentally, the rate at which cavity fluid rotates should increase with flow rate[2,4] and thus g (according to Eq. 1). However, rather than use g to achieve larger radial accelerations in the cavity, we are proposing that one can simply modify the surface tension at the wall and achieve a larger fluid velocity than for an unmodified wall at the same acceleration (or flow rate).

In order to vary the slip length and thus the velocity at the wall, we tune the c_{ij} parameter in Eq. 2 for fluid-wall interactions. Reference simulations were performed in a test channel with no cavity (as described in Section III). The lower wall always has fluid-wall interactions with $c_{\mathrm{fw}} = 1$ (the pure LJ, or wetting[15], case) while the upper wall is varied in separate simulations from $c_{\mathrm{fw}} = 0.5$ to $c_{\mathrm{fw}} = 1$ in steps of size $\Delta c_{\mathrm{fw}} = 0.05$. The resulting velocity profiles, taken as an average after the system has reached a steady state velocity, is shown in Fig. 3. For $c_{\mathrm{fw}} = 1$ we recover a quadratic Poiseuille flow profile which vanishes in the vicinity of the wall. As expected, we see that decreasing the value of c_{fw} on the upper wall increases the velocity of the fluid near the wall and thus the slip length. Similar phenomena have been observed by Koplik *et al.*[16]. Furthermore, and as a comparison, we have performed

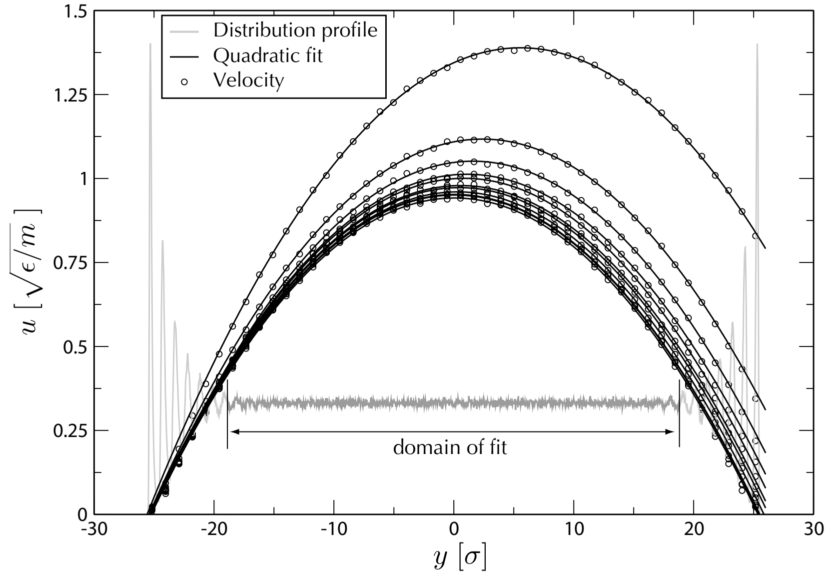

FIG. 3: Equilibrium velocity profiles for various levels of interaction between the fluid and the wall particles (with $g = 0.025\ \sigma/\tau^2$). Included in the figure is the particle distribution profile (arbitrary units) for the $c_{\rm fw} = 1.0$ case. The domain of the fit is limited to where this density profile is approximately constant and the fluid should resemble bulk conditions. For these simulations the system size is $L = 111.8\ \sigma$ and $W = 55.9\ \sigma$ and there is no cavity (just plain walls at $\pm y_{\rm wall}$.)

simulations with $c_{\rm fw} = 1$ at both walls and varied g in order to see the slip produced by increasing the acceleration.

The speed of the fluid at the wall, $u_{\rm wall} \equiv u(y_{\rm wall})$, which will be related to the slip length, is likely to be a significant factor in driving the rotation of the fluid in the cavity. Thus, we explore how the slip length depends on the fluid-wall interaction. The slip length, δ, for Poiseuille flow can be determined in two ways: by linear extrapolation or by quadratic fitting. The first method involves extrapolating the velocity linearly using a slope taken from the flow profile at the wall and determining at what value of y the velocity goes to zero. This can be expressed as a boundary condition:

$$\left.\frac{du}{dy}\right|_{y_{\rm wall}} = \frac{u_{\rm wall}}{\delta}. \tag{7}$$

The second method involves fitting the velocity profile data set with a quadratic and then finding the point at which the function vanishes. In both cases the slip length is defined as the difference between the position of the wall, $y_{\rm wall}$, and the position at which the extrapolated

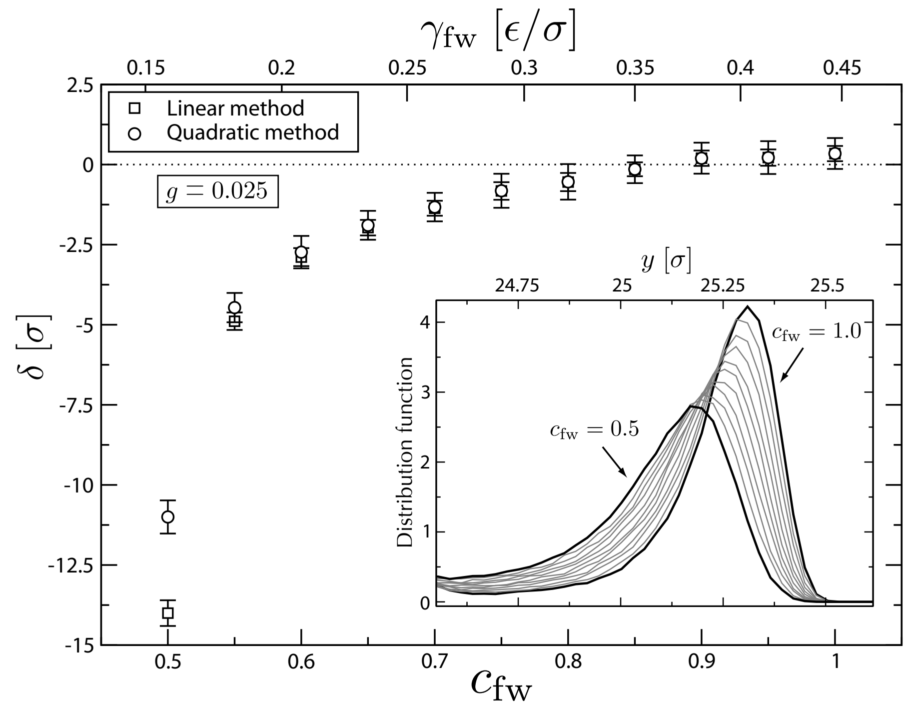

FIG. 4: Slip length δ at upper wall as a function of fluid-wall interaction for both the linear extrapolation and the quadratic fit methods. The magnitude of slip length increases with decreasing c_{fw} (interaction strength) or γ_{fw} (surface tension). The inset shows the distribution profile for particles near the wall. The rightmost curve corresponds to $c_{\mathrm{fw}} = 1.0$ and each neighbouring curve decreases by $\Delta c_{\mathrm{fw}} = 0.05$ until the last curve at $c_{\mathrm{fw}} = 0.5$ (always with a constant $g = 0.025\ \sigma/\tau^2$). As c_{fw} is decreased the position of the peak of the distribution moves further from the wall. Interestingly, we note that for the smallest surface tensions, the slip length is on the order of the size of the cavity which will be placed along that wall (i.e., $\delta \sim R$).

velocity goes to zero, y_0: $\delta = y_{\mathrm{wall}} - y_0$. The former method benefits from simplicity whereas the latter is more consistent with quadratic nature of pressure-driven flow profiles. Clearly, both methods will yield a different result, and in that sense the quantitative value of the slip length becomes a matter of definition.

To extract the slip length we fit the velocity profile using one of the above methods, for each value of c_{fw} and g. We expect the velocity profile to be fit well by a quadratic in accordance with macroscopic Poiseuille flow, with the exception that the velocity does not go to zero at the walls. Also, near the wall the fluid particles exist in layers and thus in

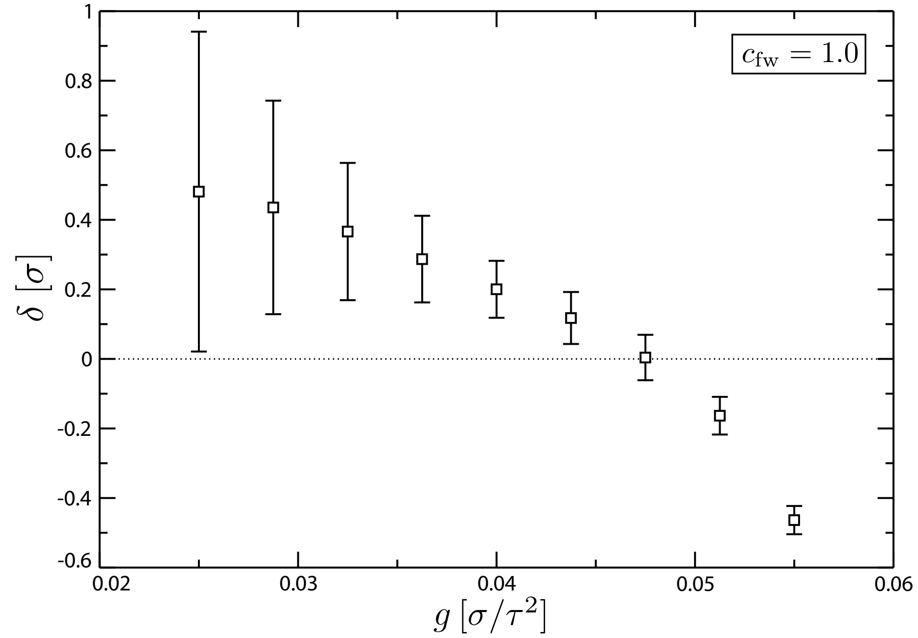

FIG. 5: Slip length δ as a function of applied acceleration g using the linear extrapolation method. The parameter c_{fw} is always constant at a value of 1.0. The quadratic method yields nearly identical values so we have left them off this figure for simplicity. As expected, the slip length becomes more negative as g increases. When $g \to 0$ the slip length corresponds to the position of the first layer of fluid near the wall.

that region we cannot expect the macroscopic prediction of hydrodynamics to hold (since the predictions were all derived assuming constant density, viscosity, etc.). Therefore, the quadratic fit to the data is restricted to the subset of points that lie within the region of the channel where the particle distribution is approximately constant rather than across the whole channel which would include the layered fluid seen near the wall (see Fig. 3). For the simulations where g is varied, the data is fit with a fourth order polynomial (ignoring the linear and cubic terms) to better capture the form of the flow profile. This is because as g becomes large we may generate viscous heating in the fluid and induce variations in the fluid viscosity, which will appear as higher nonlinearities in the spatial dependence of velocity[17]. We observe remarkable agreement between this fit and the data points which lie outside the fitting domain. The average relative errors between the fit and the data outside the domain is 6.4% (for the c_{fw} data) and 7.8% (for the g data).

The calculated slip lengths as a function of c_{fw} and g can be seen in Figs. 4 and 5. It is clear that a reduced wall-fluid interaction results in a larger slip length. We also observe that as c_{fw} is increased the slip length crosses from the negative region (outside the wall position that we defined in Section IV A) to the positive region (inside the walls) at $c_{\mathrm{fw}} \simeq 0.85$. This is intuitive as we expect that, as c_{fw} increases, the first fluid layer begins to immobilize and behave almost as if it were another layer of wall particles. As the acceleration is varied we also observe an increase of slip with g as well as the crossover from positive slip to negative slip (which has been observed in similar MD simulations by others[18]).

Note that the first fluid layer in Fig. 2 is approximately $\frac{1}{2}\sigma$ from the wall position and also that the slip lengths in Figs. 4 and 5 go to approximately this value for $c_{\mathrm{fw}} = 1$ and $g \rightarrow 0$. If the first liquid layer is immobile, which should be the case under conditions of pure LJ interaction and low acceleration, then it is intuitive that the slip length should equal the position of this monolayer. The value of c_{fw} also affects the layering of the particle distribution function near the wall. We can see in the inset of Fig. 4 that the first layer of fluid is further and further from the wall particles as c_{fw} increases. From Eq. 2 we can derive that the position of the minimum in the potential, and thus the point of zero force, where a pair of equilibrium particles would prefer to sit is given by $r_{\mathrm{min}} = (2/c_{\mathrm{fw}})^{\frac{1}{6}}\,\sigma$. However, this fluid layer will still feel pressure from fluid inside the channel. Nevertheless, the observed increase in r_{min} with decreasing c_{fw} is indeed expected. The fluid pressure causes this shift to be less than 1% whereas the calculated shift in r_{min} should be 12%. Note that as the attractive interaction is reduced, the first fluid layer moves away from the wall but its probability distribution broadens. This reflects the fact that these particle layers are increasingly acting like bulk fluid, as opposed to tightly packed layers.

V. RESULTS II: THE CHANNEL PLUS CAVITY

A. Angular Momentum in the Cavity

Surprisingly, it takes very few MD timesteps to accelerate the cavity fluid into equilibrium rotational motion. However, to err on the conservative side and ensure the data represents equilibrium, we neglect data for a significant early portion of the simulation. To quantify the level of "spin" in a given simulation we have calculated the total angular momentum

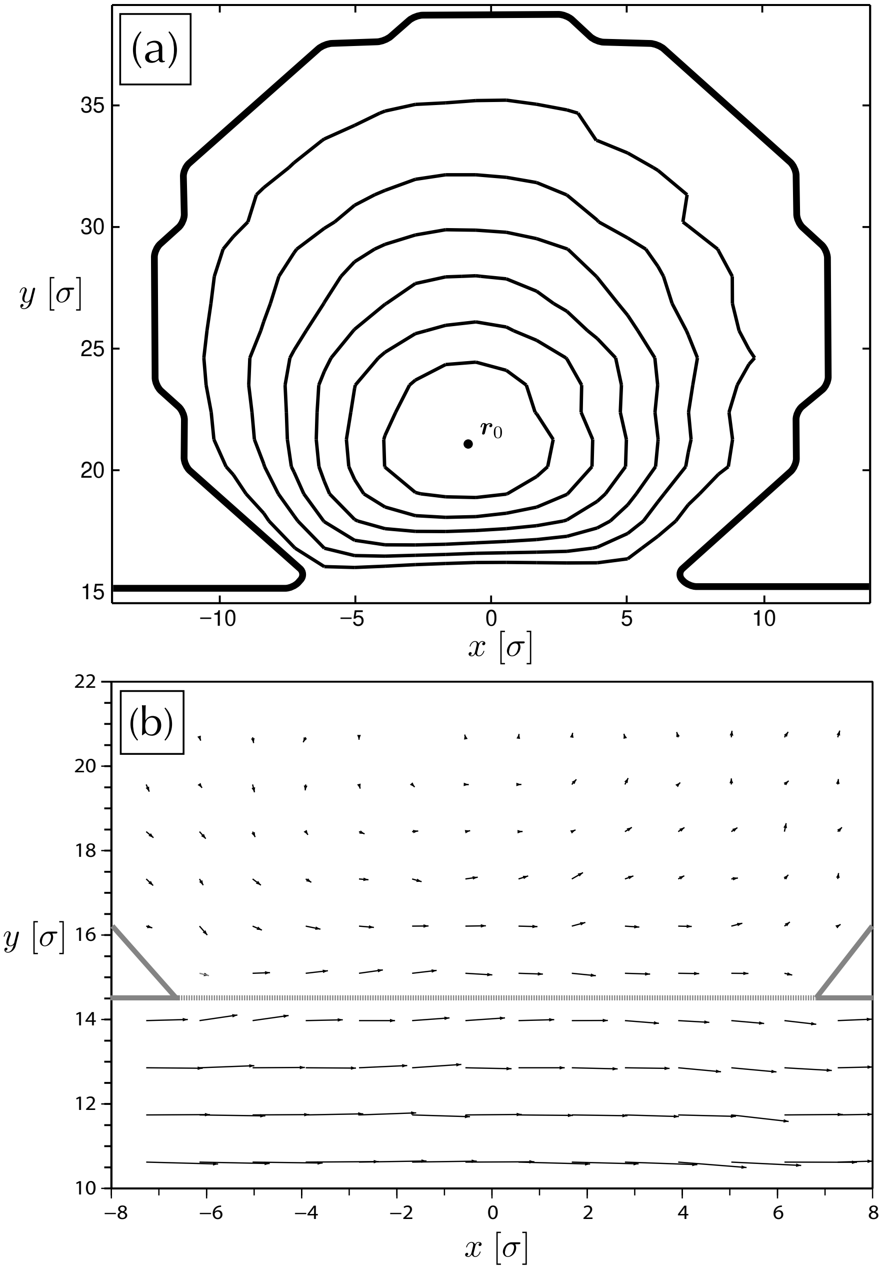

FIG. 6: Time-averaged velocity field and streamlines computed from the velocity field for $c_{\mathrm{fw}} = 0.5$ and $g = 0.025\ \sigma/\tau^2$ using scheme B. (a) shows the rotation of the fluid in the cavity. Closed streamlines, of course, represent circulation of fluid particles. The thick black line represents the approximate location of boundary between the fluid and the cavity walls. (b) shows the continuity of velocity across the coupling region. The solid gray lines denote the approximate location of the fixed wall and the dotted gray line shows the coupling region between the cavity and the channel.

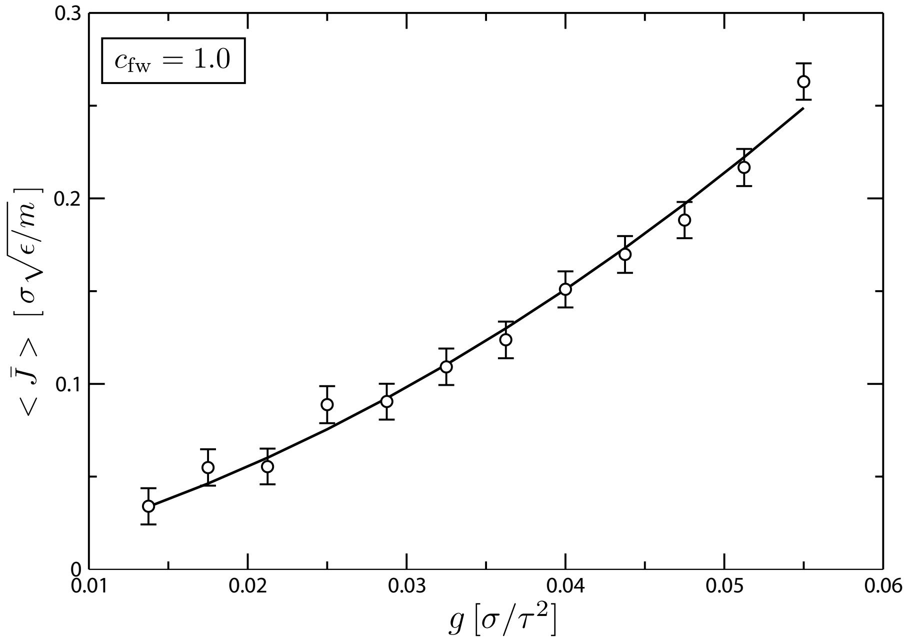

FIG. 7: Average angular momentum per particle in the cavity for various accelerations with no modification of wall-fluid interactions (i.e., $c_{\mathrm{fw}} = 1$). As expected, the average angular momentum of the fluid inside the cavity increases as a function of g. The empirical fit $\langle \bar{J} \rangle = ag(1 + g/g_0)$ is shown with parameters $a = 1.77 \pm 0.13\sigma\ \sqrt{\epsilon/m}$ and $g_0 = 0.0353 \pm 0.0026\ \sigma/\tau^2$. The latter value is thus an estimate of the critical acceleration which indicates the onset of nonlinearity.

of the cavity particles (those particles whose positions lie above the position of the upper wall) with respect to the point of zero rotation. This point, $\boldsymbol{r_0}$, is determined from velocity fields and streamlines such as those shown in Fig. 6 and the total angular momentum per particle (i.e., mass-averaged since all particles have the same mass, $m = 1$) is calculated as a sum over each using the basic relation $\bar{J} = \left|\left|\sum_{i=1}^{N} \boldsymbol{r_i} \times \boldsymbol{p_i}\right|\right| /N$, where $\boldsymbol{r_i}$ is the position of the i^{th} particle from $\boldsymbol{r_0}$ and $\boldsymbol{p_i}$ is its momentum. For better statistics, we have used the time-averaged angular momentum per particle: $\langle \bar{J} \rangle$.

The angular momentum is calculated from several simulations with varying interaction strengths and accelerations. We observe that as g is increased (with a constant $c_{\mathrm{fw}} = 1$) there is a corresponding increase in $\langle \bar{J} \rangle$ since the slip at the wall becomes significant (Fig. 7). In order to explore how c_{fw} influences the rotation of the cavity fluid, we use two different schemes. In the first scheme (hereafter referred to as scheme A), only the particles along

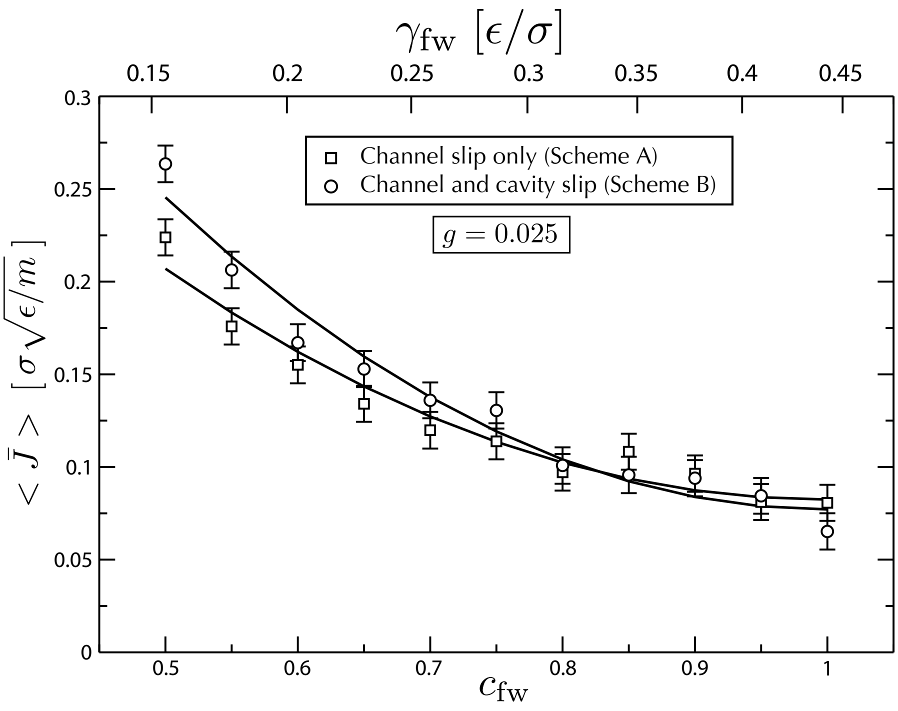

FIG. 8: Average angular momentum per particle in the cavity for various wall-fluid interaction strengths (acceleration is constant at $g = 0.025\ \sigma/\tau^2$). Results are shown from simulations where only the channel walls have modified interaction and those where both the channel and cavity walls are modified. The average angular momentum of the fluid inside the cavity increases when $c_{\rm fw}$ increases. We also observe that the two schemes differ from each other as $c_{\rm fw}$ decreases. The empirical fit $\langle \bar{J} \rangle = J_0(1 + c^{*2}/c_0^{*2})$ where $c^* = 1 - c_{\rm fw}$ is shown. The parameters are $J_0 = 0.0824 \pm 0.0055\ \sigma\sqrt{\epsilon/m}$ and $c_{\rm fw,0} = 0.593 \pm 0.040$ for scheme A and $J_0 = 0.0771 \pm 0.0065\ \sigma\sqrt{\epsilon/m}$ and $c_{\rm fw,0} = 0.662 \pm 0.051$ for scheme B.

the upper channel wall have a reduced interaction strength ($0.5 \leq c_{\rm fw} < 1$). In the second scheme (scheme B), both the channel wall and the cavity wall particles have been modified. In scheme A, the effect should be that observed above: the slip length and thus the fluid velocity increases at the wall. This will result in a larger force coupled to the cavity fluid and thus we would expect an increase in angular momentum with increasing slip length (i.e., a decrease in $c_{\rm fw}$). Scheme B will compound the previous effect with a simultaneous reduction in friction between the fluid and the cavity wall. In both schemes we have used the same values of $c_{\rm fw}$ as those used in Section IV D and the results can be seen in Fig. 8 (for a constant $g = 0.025\ \sigma/\tau^2$). We see a clear increase in angular momentum with decreasing surface tension.

We would expect the system to behave simply (perhaps linearly) in well understood regimes where we use parameter values commonly seen in the literature (i.e., pure Lennard-Jones with $c_{\mathrm{fw}} = 1$, low acceleration g). As we move away from this regime we should start to observe the onset of nonlinearity at some critical value of these parameters. We estimate this critical value by performing the following empirical fits: $\langle \bar{J} \rangle = ag(1 + g/g_0)$ for varying g and $\langle \bar{J} \rangle = J_0(1 + c^{*2}/c_0^*)$ for varying c_{fw}, where $c^* = 1 - c_{\mathrm{fw}}$. We have chosen to fit c^*, as defined, rather than c_{fw} directly since the system should exhibit "normal" properties about the pure LJ regime which is $c_{\mathrm{fw}} = 1$ and thus $c^* = 0$ (the origin). The results are shown in Figs. 7 and 8 and yield the critical values of $g_0 = 0.0353 \pm 0.0001\ \sigma/\tau^2$, $c_{\mathrm{fw},0} = 0.593 \pm 0.001$ for scheme A and $c_{\mathrm{fw},0} = 0.662 \pm 0.001$ for scheme B. The critical value of g_0 matches well with the data seen in Section IV D as it represents the point at which the slip length begins to level off to $\delta \sim \sigma/2$ in Fig. 5. The critical values of c_{fw} are also relavent as they indicate where the slip length becomes highly nonlinear in Fig. 4.

We would expect that since scheme A has a weaker wall-fluid interaction overall, it will be less effective than scheme B at spinning the cavity fluid. It is not clear that we observe this as a generality across all parameter values. For low surface tensions, where the cavity is being driven hard, scheme B is clearly more effective than scheme A but not by much (at most there is a 19% increase, at $c_{\mathrm{fw}} = 0.5$). However, for higher values of surface tension where the cavity is being driven less hard (i.e., the slip at the wall is smaller) the difference between the two schemes is no longer systematic and is on the order of the noise in the data.

We can visualize the fluid motion in the cavity by looking at the two-dimensional velocity field. This can be seen in Fig. 6 for a simulation with $c_{\mathrm{fw}} = 0.5$ using scheme B. Figure 6a demonstrates the rotational motion of the fluid in the cavity with streamlines, found by integrating the velocity field. It should be noted that the stagnation point of the flow is not in the centre of the circular cavity and is in fact closer to the coupling region: presumably, this is dependent on the fluid properties, such as viscosity, the cavity size and offset although we are not exploring this in the current work. Also presented in Fig. 6b is a higher resolution velocity field focussed on the coupling region of the channel-cavity system illustrating the continuity of the velocity field across the interface and clear coupling between the cavity and channel fluids.

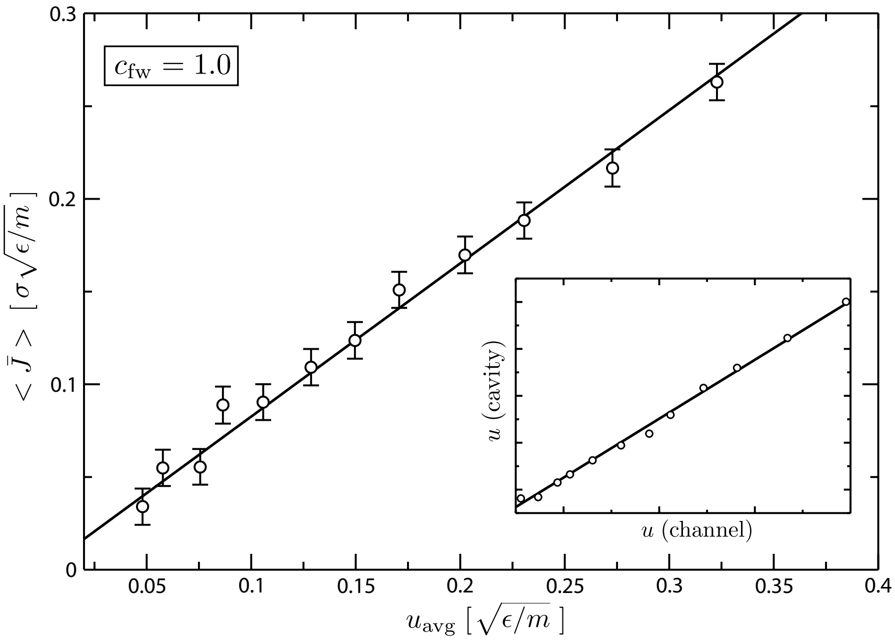

FIG. 9: The dependence of average angular momentum $\langle \bar{J} \rangle$ from the MD simulations on average forcing velocity ($u_{\mathrm{avg}} = (u_{\mathrm{chan}} + u_{\mathrm{cav}})/2$). The wall-fluid interaction is kept constant with $c_{\mathrm{fw}} = 1.0$. The fit is linear with zero intercept: $\langle \bar{J} \rangle = (0.83 \pm 0.01) u_{\mathrm{avg}}$. The inset shows the linear relationship between u_{cav} and u_{chan} with a slope of 0.63 ± 0.01.

B. Velocity Dependence of Angular Momentum

In order to predict how the angular momentum of the cavity fluid should depend on the properties of the system we performed calculations based on the predictions of macroscopic hydrodynamics. The 2D incompressible Navier-Stokes equation for a Newtonian fluid[7] can be expressed in terms of vorticity ω and the streamfunction ψ as

$$\frac{\partial \omega}{\partial t} + \boldsymbol{u} \cdot \nabla \omega = \frac{\eta}{\rho_0} \nabla^2 \omega, \tag{8}$$

$$-\nabla^2 \psi = \omega, \tag{9}$$

where $\boldsymbol{u} = u\hat{\mathrm{x}} + v\hat{\mathrm{y}}$, $\partial\psi/\partial y = u$, $\partial\psi/\partial x = -v$ and $\omega = ||\nabla \times \boldsymbol{u}||$. To model our system we use a circular boundary with a piece cut out by intersecting a horizontal straight line near the lower edge. The boundary conditions are zero velocity around the circular edge and a constant tangential velocity $\boldsymbol{u} = V\hat{\mathrm{x}}$ at the straight edge. This latter condition emulates the external forcing at the coupling region we see in our MD simulations (at equilibrium).

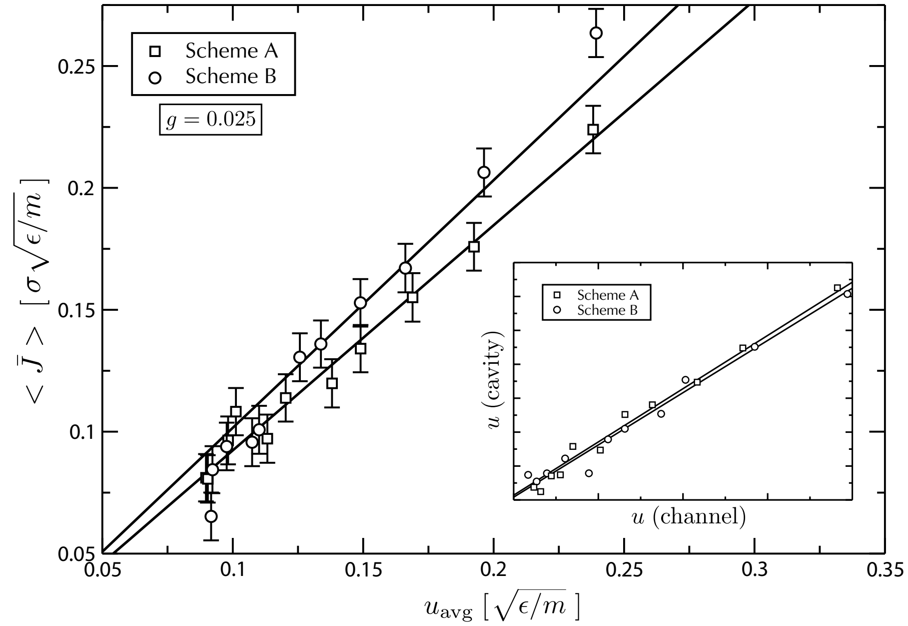

FIG. 10: The dependence of average angular momentum $\langle \bar{J} \rangle$ from the MD simulations on average forcing velocity ($u_{\mathrm{avg}} = (u_{\mathrm{chan}} + u_{\mathrm{cav}})/2$). The acceleration is constant at $g = 0.025\ \sigma/\tau^2$ and the wall fluid interaction ranges from $c_{\mathrm{fw}} = 0.5$ to $c_{\mathrm{fw}} = 1.0$. The fit is linear with zero intercept: $\langle \bar{J} \rangle = \alpha u_{\mathrm{avg}}$ with proportionality constants $\alpha_{\mathrm{A}} = 0.92 \pm 0.01$ and $\alpha_{\mathrm{B}} = 1.02 \pm 0.01$. The inset shows the linear relationship between u_{cav} and u_{chan}. The slopes are 0.63 ± 0.01 for scheme A and 0.62 ± 0.01 for scheme B.

The total angular momentum is calculated, as before, by finding the stagnation point $\boldsymbol{r_0}$ and integrating $(\boldsymbol{r} - \boldsymbol{r_0}) \times \rho_0 \boldsymbol{u}$ over the area of the cavity. Equations 8 and 9 are solved using finite difference (FD) methods, with parameters chosen so that $\mathrm{Re} = O(1)$. We will not explicitly show the results of these calculations as they simply suggest that the average angular momentum $\langle \bar{J} \rangle$ should increase linearly with V such that $\langle \bar{J} \rangle = \alpha V$ (where α is some proportionality constant).

We will use this prediction to help explain our MD results and so must first determine how to relate the parameters from MD to those in the FD calculations. Clearly, the mass averaged angular momentum from the FD calculations is equivalent to the average angular momentum per MD particle: $\langle \bar{J} \rangle$. We will make the correspondence between the forcing speed V and the average speed of fluid at the wall in the vicinity of the cavity in the MD simulations. This velocity, $u_{\rm avg}$, is defined as the average over the region along x adjacent to the coupling interface and over two layers of fluid particles (both inside and outside the cavity, $u_{\rm cav}$ and $u_{\rm chan}$ respectively). From the FD predictions, we should observe a linear relationship between the velocity of two layers of fluid particles we average over and thus the average should not disrupt the linear relationship between angular momentum and velocity.

We present the average angular momentum plotted versus the average forcing velocity about the coupling region in Figs. 9 and 10 (for varying g and $c_{\rm fw}$, respectively). Also, the linear relationship between the two velocities is shown in the insets. For the angular momentum, each data set is fit with the expected relationship $\langle \bar{J} \rangle = \alpha u_{\rm avg}$, with good agreement especially using scheme A. It is not clear whether the results for scheme B should be linear in any case. The predictions from macroscopic hydrodynamics were for a system with zero velocity at the cavity walls but, as we observed in Section IV D, when the wall-fluid interaction is modified (as it is in scheme B) there exists a non-zero slip and thus the zero velocity boundary condition should not hold.

C. Effeciency of "Spin" Generation

To demonstrate that we are in a similar regime as that existing in previous experiments[2–4] we will formulate a nondimensional parameter to characterize the system based on the cavity spin, dimension and channel flow. Let us define the dimensionless pin number, S, as the ratio between the product GR, where G is the radial acceleration in the cavity and R is its radius, and the square of the average fluid velocity in the channel $\bar{u}$:

$$S \equiv \frac{GR}{\bar{u}^2}. \tag{10}$$

The values observed experimentally are $G = 1.4 \times 10^7$ m/s^2, $R \simeq 50$ μm and $\bar{u} = 45$ m/s^2 which yield a dimensionless Spin number of $S = 0.345$. From our simulation data for $c_{\rm fw} = 0.5$ and $g = 0.025\ \sigma/\tau^2$ we have $G = 0.00559\ \sigma/\tau^2$ (the maximum radial acceleration, which is observed just inside the coupling region), $R = 12.3\ \sigma$ and $\bar{u} = 0.819\ \sigma/\tau$. Using these values we calculate the Spin number to be $S = 0.103$ which is of the same order of magnitude as that observed experimentally.

In Figs. 9 and 10 we observe approximately the same range of angular momentum in the cavity over the same range of forcing speeds for all of the various schemes we have employed to spin the cavity fluid. In fact, our results indicate that by keeping g at a reasonable value and modifying the wall-fluid interaction we can achieve cavity spin comparable to that achieved by pushing the fluid harder. As an example, let us take simulations from all three cases with approximately the same flow rate in the channel: $\bar{u} \simeq 0.728 \pm 0.005\,\sigma/\tau$. If we keep the wall-fluid interaction as pure wetting ($c_{\rm fw} = 1$) then we need an acceleration of $g \simeq 0.029\,\sigma/\tau^2$ to achieve this flow rate and it results in an average angular momentum in the cavity of $\langle \bar{J} \rangle = 0.0904\,\sigma\sqrt{\epsilon/m}$. For the cases where the wall fluid interaction is modified we use an acceleration of $g = 0.025\,\sigma/\tau^2$ and to achieve the above flow rate we require $c_{\rm fw} = 0.6$ which results in average angular momenta of $\langle \bar{J} \rangle = 0.1573\,\sigma\sqrt{\epsilon/m}$ for scheme A and $\langle \bar{J} \rangle = 0.1679\,\sigma\sqrt{\epsilon/m}$ for scheme B. This is effectively an increase of 71% in scheme A and 82% in scheme B for a 54% decrease in surface tension.

VI. CONCLUSIONS

Shelby *et al.* have performed exciting experimental research and we have reproduced and expanded upon their basic idea. Ssing Molecular Dynamics, we have simulated spin generation in a coupled cavity-channel system which is in the same physical regime as that seen in experiments. From these simulations we observed the finite structure of the fluid and have shown that its hydrodynamic properties are laminar. We were able to make the connection between surface tension of the wall-fluid interface and the hydrophobicity of the wall by analysing the fluid slip along the wall. In particular, we can simulate systems with hydrophobicity without making assumptions about boundary conditions. These principles can be applied to a coupled cavity-channel system to control the angular momentum in the cavity. We were able to increase the level of spin in the cavity by over 80%. Predictions from macroscopic hydrodynamics were succesfully reproduced, showing that even when the finite structure of the fluid is observable these predictions can still hold. Molecular Dynamics has shown itself to be useful for exploring systems that would be difficult using traditional means (i.e., modelling hydrophobicity with hydrodynamics).

We are exploring how the spin depends on the size of the coupling region between the cavity and the channel. It is clear that there must be an optimal coupling length if we consider the extreme cases: if the length is very large (i.e., the cavity offset is less than zero), the channel fluid will simply stream into the cavity and back out again, producing no spin and if the length is very small, the coupling between the channel and the cavity will be weak and therefore spin will be very low. Between the two extreme cases there must be an optimal length for inducing spin with the least amount of input energy. Our simulations use an intermediate sized coupling region and so we believe the results to be representative of the physics near the optimal system. This study could be extended to explore the system as the width of the channel W or the cavity radius R are reduced to the nanoscale. (In other words, how do the physics scale as the system dimensions approach the nanometre regime.) Molecular Dynamics allows us to explore fluid layering which would be dominant on nanoscopic length scales. Also, there must be some exchange of mass between the channel and the cavity and so it would be interesting to explore this and how it might impact the use of the cavity as a centrifugation cell, particularly the centrifugation of polymeric substances which can be easily implemented in our Molecular Dynamics model.

VII. ACKNOWLEDGEMENTS

G. W. S. would like to acknowledge the financial support of a Natural Science and Engineering Research Council (NSERC) Discovery grant. E. C. J. O. would like to acknowledge the financial support of the Sun Microsystems of Canada Scholarship, the Nunatsiavut Government PSSSP and the University of Ottawa Admissions Scholarship. Furthermore, E. C. J. O. would like to thank F. Tessier, M. Kenward, S. Casault, M. Bertrand and L. Taylor for discussions, assistance and support in the preparation of this work.

---

[*] Electronic address: `eoliv087@uottawa.ca`

[†] Electronic address: `gary.slater@uOttawa.ca`

[1] T. Squires and S. Quake, Rev. Mod. Phys. **77**, 977 (2005).

[2] J. P. Shelby, D. S. W. Lim, J. S. Kuo, and D. T. Chiu, Nature **425**, 38 (2003).

[3] J. P. Shelby and D. T. Chiu, Lab Chip **4**, 168 (2004).

[4] J. P. Shelby, S. A. Mutch, and D. T. Chiu, Anal. Chem. **76**, 2492 (2004).

[5] A. Prasad and J. Koseff, Phys. Fluids A-Fluid **1**, 208 (1989).

[6] J. Koseff, A. Prasad, C. Perng, and R. Street, Phys. Fluids A-Fluid **2**, 619 (1990).

---

[7] P. K. Kundu and I. M. Cohen, *Fluid Mechanics* (Academic Press, San Diego, CA, 2002), 2nd ed.

[8] J. Koplik and J. R. Banavar, Annu. Rev. Fluid Mech. **27**, 257 (1995).

[9] D. C. Rapaport, *The Art of Molecular Dynamics Simulation* (Cambridge University Press, Cambridge, 1995).

[10] T. Soddeman, B. Dünweg, and K. Kremer, Phys. Rev. E **68**, 046702 (2003).

[11] E. A. J. F. Peters, Europhys. Lett. **66**, 311 (2004).

[12] F. Tessier and G. W. Slater, Macromolecules **39**, 1250 (2006).

[13] J. S. Rowlinson and B. Widom, *Molecular Theory of Capillarity* (Oxford University Press, Oxford, 1987).

[14] J.-L. Barrat and L. Bocquet, Phys. Rev. Lett. **82**, 4671 (1999).

[15] J. Koplik and J. R. Banavar, Phys. Rev. Lett. **84**, 4401 (2000).

[16] J. Koplik and J. R. Banavar, Phys. Rev. Lett. **80**, 5125 (1998).

[17] K. Travis, J. Chem. Phys. **112**, 1984 (2000).

[18] Y. L. Gratton and G. W. Slater, Eur. Phys. J. E **17**, 455 (2005).

3

Project II: Mixing

E. C. J. Oliver and G. W. Slater
A Theoretical and Molecular Dynamics Study of Mixing in Channels with Obstacles
Status: submitted to *Journal of Micromechanics and Microengineering*, July 26 2006

A Theoretical and Molecular Dynamics Study of Mixing in Microchannels with Obstacles

E C J Oliver

E-mail: `eoliv087@uottawa.ca`
Department of Physics, University of Ottawa, 150 Louis-Pasteur, Ottawa, ON, Canada, K1N 6N5

G W Slater

E-mail: `gary.slater@uOttawa.ca`
Department of Physics, University of Ottawa, 150 Louis-Pasteur, Ottawa, ON, Canada, K1N 6N5

Abstract. A system consisting of two miscible fluids in a microchannel under laminar flow has been examined with theoretical techniques and simulated using Molecular Dynamics (MD). We have applied the theory of diffusion to predict the displacement of particles as they diffuse across a channel perpendicular to a Poiseuille flow. Using MD simulations, we have studied the presence of obstacles in the flow path and shown, contrary to what has been proposed recently, that they do not significantly increase mixing efficiency in microchannels. Their effect is such that (i) the flow profile becomes flattened within a certain range of the obstacles and (ii) the fluid flow acquires lateral components and so follows a sinuous path through the channel. From our theoretical predictions and numerical simulations, we show that the former results in increased levels of partial mixing when compared to a system lacking obstacles. However, obstacles do not reduce the length required for full mixing. Furthermore, the second effect increases contact between the fluids but the mixing increase is negligible.

PACS numbers: 64.75.+g

1. Introduction

The essential problem with efficient mixing on small scales is that, in general, flow is laminar and thus the instabilities produced by turbulent flow that accelerate the fluid mixing on macroscopic scales (such as stirring cream into coffee) are no longer present. In the absence of these mixing accelerants, diffusion is the only natural drive to mixing. Laboratories would like to develop methods to enhance the effects of diffusion or introduce other phenomena into the system in order to facilitate efficient mixing at low Reynolds numbers where viscous effects dominate over inertial ones. This problem has been well studied recently and there have been many successful attempts which involve processes such as vortices induced by curved flow [1], electroosmosis [2], electro-hydrodynamics [3], chemically and geometrically patterned channel walls [4, 5], hydrodynamic focussing (nanojets) [6] and chaos [7]. A nice review of work in this field (as well as other fields in microfluidics) can be found in a recent publication by T. M. Squires and S. R. Quake [8].

In a recent study, Wang *et al.* investigated how the presence of obstacles in a microchannel might enhance the mixing level at the output [9, 10]. They claim that certain obstacle configurations modify the fluid flow laterally and force one species into the other and thus promote an increase in mixing. We will demonstrate, however, that this claim is contrary to what one expects from laminar flow and in actuality what they are observing are the effects of flow profile distortion and increased contact area between the two fluid species on the dynamics of diffusion in the presence of flow.

This paper is organized in three main segments. First, we will present the fluidic system along with the relavent hydrodynamic theory outlining laminar flow, the behaviour of diffusion in channels and the concept of mixing in channel flows. Then, we will review the simulation method and how it is applied to our system. Following that, we present the results in three sections. First, we explore the laminar hydrodynamic and diffusive properties of the system. Next, we examine the mixing properties in channels without obstacles. Finally, we will introduce obstacles into the system and show that their presence affects the mixing characteristics of the system by lenghtening the mixing interface as well as deforming the flow profile. It is this last effect that will be the focus of our claim that obstacles do not increase mixing efficiency in channels where complete mixing is required.

2. System and Theory

Consider a fluidic system such as the one shown in Fig. 1 consisting of two miscible fluid species (labelled A and B) confined between two parallel plates spaced a distance W apart. We are examining only a section of length L in the x direction. The fluid is moving in the x direction with a Poiseuille flow profile. The channel dimensions are on the order of micrometres and the flow is laminar.

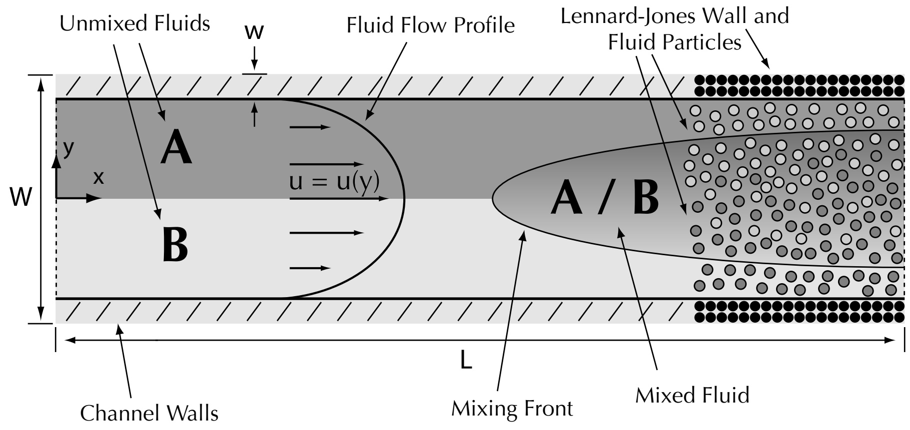

Figure 1. Schematic of the fluid-channel system. The two miscible fluid species (A and B) are seperated along the midplane of the channel and travel through the channel with a Poiseuille flow profile. The fluids are allowed to mix via diffusion which produces a mixing front between the mixed and unmixed fluid. Also shown here is an example of the finite bead structure of the channel walls and fluid used in our simulations.

2.1. Laminar Flow

The Reynolds number determines the basic hydrodynamic behaviour when considering fluid flow confined in channels and can be expressed as

$$\mathrm{Re} \equiv \frac{\rho_0 \bar{u} h}{\eta}, \tag{1}$$

where $\bar{u}$ is the average fluid velocity (the flow rate) over the channel cross-section of width h, η is the shear viscosity (or dynamic viscosity, sometimes denoted by μ) and ρ_0 is the average fluid density. The transition from laminar to turbulent flow can be indicated by the Reynolds number, laminar flow ocurring for $\mathrm{Re} \lesssim 10^3$ and turbulent flow for $\mathrm{Re} \gtrsim 10^3$. For hydrodynamic flow in channels whose cross section is on the order of or less than micrometers, then for reasonable $\bar{u}$ the system is firmly rooted in the realm of laminar flow. In the laminar flow regime, the flow is smooth and predictable and lacks any of the instabilities and rich eddy structure that is found in turbulent flow. The dynamics are dominated by the viscosity of the system rather than by inertial forces and the dynamics of all flows are reversible (if we neglect diffusion, which is topic of the next section).

Consider a fluid confined between two plates parallel to the xz-plane with the origin of the coordinate system midway between them. For low Reynolds numbers, the flow profile generated by a pressure difference, p', along the x-direction in a channel is of the Poiseuille type and has the quadratic form

$$u(y) = u_0 \left(1 - \frac{y^2}{y_0^2}\right), \tag{2}$$

where $u_0 = -y_0^2 p'/2\eta$ and $\pm y_0$ are the positions of the two channel walls. Note that we are assuming no-slip at the boundaries, which will be sufficient for our studies (see Refs. [11, 12, 13, 14] for explorations of slip length in Molecular Dynamics simulations of laminar flow). In practice, Poiseuille flow is usually generated by a pressure gradient along the channel but it can also be generated by a gravity-like acceleration g in which case we can make the substitution $-p' = \rho_0 g$ in Eq. 2.

2.2. Diffusion

Since turbulence does not exist in a laminar flow environment, we cannot rely on it to mix the fluids as we would in a turbulent system. Therefore, the drive behind fluid mixing is the relatively slow diffusion of one fluid into the other. The Peclet number, Pe, is a measure of the relative influences of advection and diffusion for flows in channels and is defined as

$$\mathrm{Pe} \equiv \frac{\bar{u} y_0}{D}, \tag{3}$$

where D is the diffusion coefficient. We use the length scale $y_0 = h/2$ (half the cross-sectional width) since it is the largest distance in our system that particles need to diffuse in order to initiate mixing. Large Pe implies that fluid motion is dominated by advection (flow) rather than diffusion. When Pe is large, it is difficult to mix fluids by diffusion alone as a long channel (i.e., much longer than its width) is required to allow diffusion to take its course.

The average time, $\langle t_\mathrm{D} \rangle$, needed for molecular diffusion to transport fluid a distance d in one dimension is given by the Einstein relation

$$\langle t_\mathrm{D} \rangle = \frac{d^2}{2D}. \tag{4}$$

If the fluid is being transported along the channel at a constant velocity u then we can deduce the average distance $\langle l \rangle$ the fluid travels along the channel in the flow direction while diffusing a distance d in the perpendicular direction:

$$\langle l \rangle = u \langle t_\mathrm{D} \rangle = \frac{ud^2}{2D}. \tag{5}$$

Given channel geometry and flow speed and using Eqs. 4 and 5 we can calculate both the time required $\langle t_\mathrm{D} \rangle$ and the total distance travelled $\langle l \rangle$ along the channel for particles diffusing a distance d from the channel centre. The choice of the initial position is important since the result shown above will be dependent on the velocity which itself is position dependent. We choose the original position to be the centre since, as we will see later, the mixing interface originates as particles in the channel centre diffuse towards the wall). Let L_0 be the channel length where the particles have diffused the full width required: y_0. From Eq. 5 this length is given by $L_0 = uy_0^2/2D$ from which we can derive the Peclet number to be $\mathrm{Pe} = L_0/y_0$. This interpretation of Pe is such that it represents the aspect ratio of a channel whose length L_0 is the minimum required for particles to diffuse all the way to the wall ($d = y_0$).

It should be noted that the above expression relating $\langle l \rangle$ and d (Eq. 5) only applies for a constant velocity profile (i.e., $u(y) = u \equiv \text{const.}$). We will be examining diffusion in a channel where the flow is not flat but spatially dependent, namely a Poiseuille flow profile. The equivalent expression to Eq. 5 becomes

$$\langle l \rangle = \frac{u_0 d^2}{2D} \left(1 - \frac{1}{2} \frac{d^2}{y_0^2} \right) . \tag{6}$$

The first term is identical to Eq. 5 and the second term involves a correction due to the quadratic nature of the flow profile. The derivation of this expression can be found in Appendix A and a graphic representation of Eqs. 5 and 6 can be found in Fig. 2. The phenomena presented in this figure will be discussed in the following section. We will refer to curves showing the average length along the channel a particle has travelled, $\langle l \rangle$, while diffusing a distance d (such as those deduced from Equations such as Eq. 5 and Eq. 6) as *flow-diffusion profiles.* Note that this entire discussion assumes that the diffusion coefficient D is independent of spatial position. In reality, due to the presence of the rigid walls, there may be some spatial dependence [15, 16] but we will assume its effect to be negligible.

2.3. Mixing

Diffusion is inherently linked to mixing in laminar flow systems of multiple fluid species. As mentioned above, due to the lack of instabilities caused by turbulence, diffusion is the only mechanism that can mix fluids in simple laminar channel flows. As fluids of different species diffuse into each other we can qualitatively describe the level of mixing to have increased, until the point where both concentrations are equal and we would consider the fluid to be fully mixed. Later we will present a quantitative mixing function to be used with our numerical simulations, but for the following discussion consider a hypothetical measure that is maximized when the fluids are fully mixed and zero when they are completely separated. If we examine the flow-diffusion profiles due to various flow profiles we can think of the curves as roughly corresponding to the position of the *mixing front.* By mixing front we refer to the division between unmixed fluid and mixed fluid (the region containing the latter widens as the fluids flow along the channel). In practice this front is not clearly defined since diffusion is a process which results in a wide distribution of particle positions; however this expression would correspond to the mean position of the front.

Now, consider different flow profiles, $u(y)$, but with the same flow rate, $\bar{u} = \int_{-y_0}^{y_0} u(y) dy / 2y_0$. Equations 5 and 6 predict that if the average flow rate is the same then a particle diffusing from the centre of the channel (where we are considering the initial interface between different fluid species to be) will travel the same length down the channel, $L_0 = \bar{u} y_0^2 / 2D$, when it reaches the position of the wall, y_0. This is intuitive as the time taken to diffuse that distance is always the same (simply Einstein's relation $\langle t_{\mathrm{D}} \rangle = y_0^2 / 2D$) and so if the average velocity felt is always the same then the average distance travelled will be the same (there is no coupling between the motion in x and

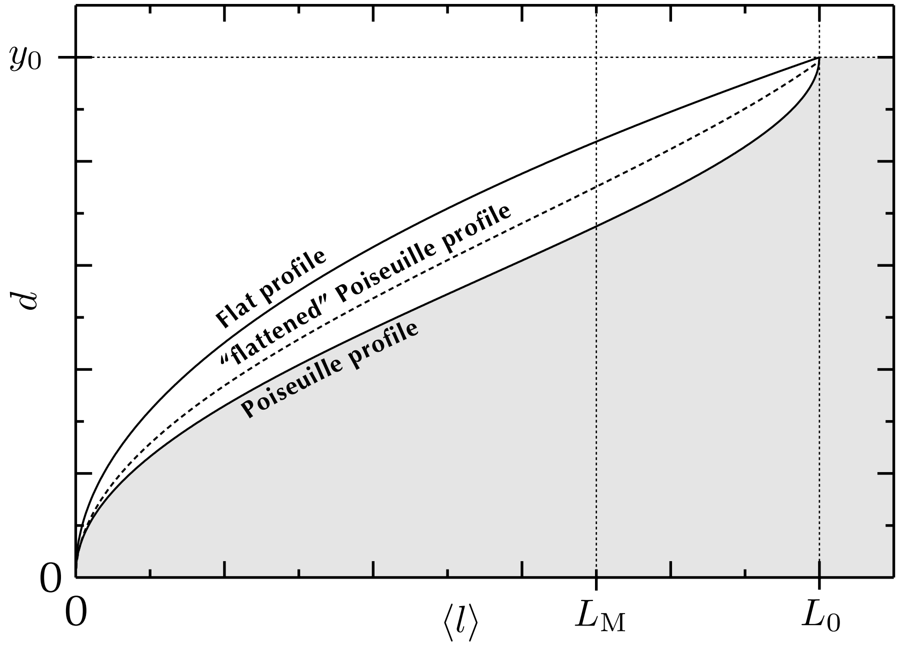

Figure 2. The flow-diffusion profiles for various flows. The results are shown for both a flat profile, $u(y) = u_0/2$, and a Poiseuille profile, $u(y) = u_0(1 - y^2/y_0^2)$, as well as a general "flattened" Poiseuille flow profile lying somewhere in between. For flow profiles with the same average velocity, $\bar{u}$, particles will on average take the same channel length, L_0, to reach the channel wall, y_0, by diffusion.

y). As a demonstration we have shown a hypothetical "flattened" Poiseuille flow profile (with the same average flow rate), whose d-vs-$\langle l \rangle$ curve should lie somewhere between the flat profile and the pure Poiseuille profile (as seen in Fig. 2). (A numerical method of determining this curve from the flow profile data is outlined in Appendix B.) Therefore, as long as the channel length, L, is greater than L_0 then the measured level of mixing at the channel outlet will always be 100%. However, if the channel length is less than L_0 then the measured level of partial mixing will depend on the shape of the flow profile. A flat profile will yield a higher level of mixing than a Poiseuille profile. Similarly, so will a flattened Poiseuille profile.

We will show that the primary effect produced by placing obstacles in the flow path, which is what was studied in Refs. [9, 10], is to flatten its quadratic flow profile so that the level of partial mixing observed at some measuring length, $L_M < L_0$, is greater than that observed by a perfectly quadratic flow profile. However, as demonstrated above, if $L_M \geq L_0$ then the measured level of mixing for any profile will be 100%.

3. Simulation and Measurement Method

In order to substantiate our claim in Section 2.3 we will explore the mixing properties of channels with and without obstacles by explicit simulation of the fluid and solid walls. We consider the size of the system presented in Section 2 to be very large in the z direction. All forces and geometries will be isotropic in z and so we will make the approximation that the flow in any two-dimensional slice of the system parallel to the xy-plane will be identical. Therefore, we will confine our simulations to two dimensions which will both retain the essential physics as well as increase computational efficiency.

3.1. Molecular Dynamics

We model the system described in Section 2 as an ensemble of interacting beads and simulate their dynamics using the Molecular Dynamics (MD) computational algorithm. The beads obey the Lennard-Jones (LJ) potential that acts between a pair of particles i and j

$$U_{ij} = \begin{cases} 4\epsilon\left[\left(\frac{\sigma}{r_{ij}}\right)^{12} - c_{ij}\left(\frac{\sigma}{r_{ij}}\right)^{6}\right] + \epsilon_0 & ,\text{if} r_{ij} \leq r_c \\ 0 & ,\text{if} r_{ij} > r_c \end{cases} \tag{7}$$

where ϵ and σ are constants that set the energy and length scales for a particular substance. All particles in the system interact with the LJ potential except for wall-wall interactions since the positions of the wall particles are fixed (their interactions with each other are ignored). For efficient numerical operation, we do not consider the pure LJ potential up to $r = \infty$ but instead neglect long range interactions. We do this by cutting it off at a certain radius r_c so that the potential is zero for $r > r_\mathrm{c}$ and a constant $\epsilon_0 = -U(r_\mathrm{c})$ is added to ensure continuity [17]. We choose $r_\mathrm{c} = 2.5\,\sigma$ which retains the repulsive core and most of the attractive tail. The parameters of the system were chosen as follows: $\epsilon = 1$, $\sigma = 1$, the average density of the fluid is $\rho_0 = 0.8/\sigma^2$, the thermal energy is $k_\mathrm{B}T = 1\,\epsilon$ and all particles have mass $m = 1$.

The Molecular Dynamics algorithm consists of integrating Newton's equations of motion for each particle in the system using finite difference methods. Methods such as linked neighbour and cell lists are used to facilitate the efficient operation of the algorithm [17]. It should be noted that in order to keep the temperature of the system constant a thermostat is employed and since the system we are studying is not in equilibrium we must choose a thermostat that can be applied to nonequilibrium MD. The thermostat used here is based on the method of dissipative particle dynamics (DPD) which conserves momentum and reproduces hydrodynamic interactions [18]. Care has been taken to ensure that known time step effects when using DPD are avoided [19].

As mentioned earlier, we have chosen to work in two dimensions (xy) for the simplicity of the algorithm. This can be justified as follows: if the channel size in the dimension perpendicular to the two dimensions considered (z) is much larger than its width in y then any xy slice we take should be identical. Therefore, by simulating this slice independently we can recreate its flow characteristics. The channel we consider is rectangular in xy with walls containing the fluid along y and periodic boundary conditions along x. Three system lengths were used: $L = 55.9\,\sigma$ (for a small test system demonstrating laminar flow), $L = 447.21\,\sigma$ (for mixing in channels with obstacles) and $L = 559.02\,\sigma$ (for mixing in channels without obstacles) and the width is always $W = 55.9\,\sigma$ with the wall particles taking up a width $w = 2.2\,4\sigma$ (two particle layers) on each side. The total number of particles in these three systems are $N = 2500$, $N = 20000$ and $N = 25000$, respectively. Simulations were performed on two 3.2 GHz Pentium 4 workstations with one and two GB of RAM each. Each simulations took between 2 days and one week to complete.

3.2. Mixing Value: A Per-particle Quantification of the Mixing Level

Mixing is a highly qualitative state; qualitatively fluids can be *mixed* or *unmixed* but mixing does not have a rigid scientific definition. In the past, measures have been proposed to quantify the level of mixing between two fluids inlcuding those based on concentration in slices across the channel [9, 10] or entropy [20]. We propose an expression that will quantify the local level of mixing associated with each particle in a system of binary fluids. From there, one is free to average in many different ways in order to represent the mixing of the bulk fluid.

Our model is composed of discrete particles that have a type associated with them which defines which fluid species that particle belongs to. The method we have employed is to associate a level of mixing with each individual particle based on its surrounding environment. Consider all the particles contained within a radius r_{mix} about a given particle (particle i) *ignoring* the centre particle. In a binary mixture, we will have N_{L_i} particles of the same type as particle i and N_{U_i} particles of different type from particle i such that $N_i = N_{\text{L}_i} + N_{\text{U}_i}$ is the total number of particles contained in r_{mix}. We propose, as the expression to quantify the local level of mixing, M_i, associated with particle i, the product of N_{U_i}/N_i and N_{L_i}/N_i (both of which run from 0 to 1) and normalized to equal 1 at $N_{\text{U}_i} = N_{\text{L}_i} = N_i/2$:

$$M_i = 4\frac{N_{\text{U}_i} N_{\text{L}_i}}{N_i^2}, \tag{8}$$

So, $M = 1$ when the fluids are perfectly mixed and $M = 0$ when they are completely unmixed. This produces a function that is quadratic in N_{U_i} (or N_{L_i} since they sum to the constant N_i) with zeros at $N_{\text{U}_i} = 0$ ($N_{\text{L}_i} = N_i$) and $N_{\text{U}_i} = N_i$ ($N_{\text{L}_i} = 0$) and a value of 1 at $N_{\text{U}_i} = N_{\text{L}_i} = N/2$. Note that we ignore the centre particle in these calculations, otherwise there is an error on M_i of the order N_i^{-2}. Clearly, M_i is a function of r_{mix} (since the number of particles will be a function of r_{mix}) and so it is necessary to choose r_{mix} larger than the average interparticle spacing but smaller than the bulk features of the system such as fluid spacing or obstacle sizes. If r_{mix} is too small then we will have poor statistics but if it is too large it will no longer be local.

The utility of the expression presented above can be illustrated with a few test cases. Consider a particle i surrounded by particles of the same type. We would consider this particle to be completely unmixed and thus the expression gives us $M_i = 0$. Next, consider a case less obvious than the first, that the same particle is surrounded by particles all of a different type. The fluid is definitely not mixed as both species are not

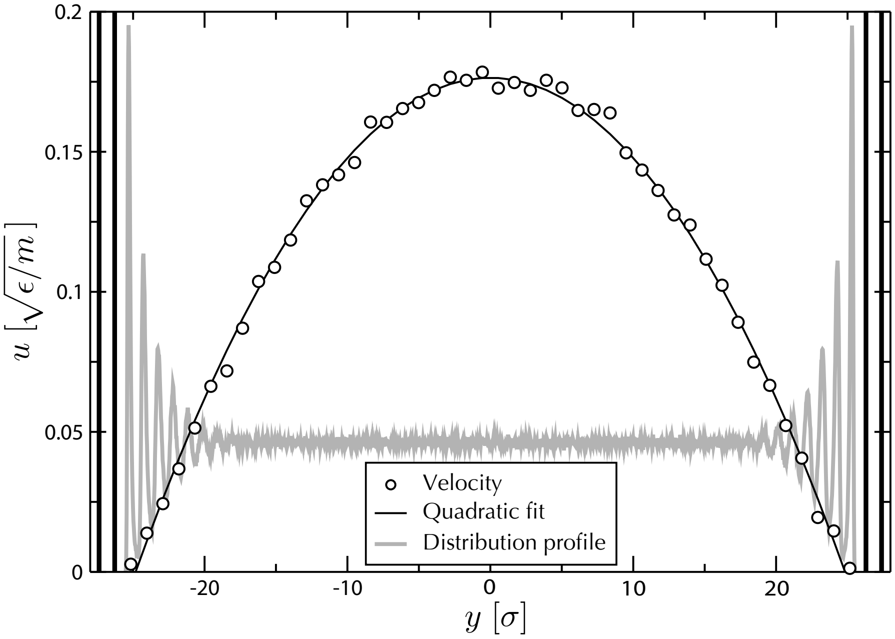

Figure 3. Velocity data taken as averages along 50 slices in the x direction (circular data points) and a fit to the data using Eq. 2 (solid black curve) with y_0 and η as free parameters yielding $y_0 = 24.83 \pm 0.20\,\sigma$ and $\eta = 12.20 \pm 0.10\,\sqrt{m\epsilon}/\sigma$. The force on each particle is $mg = 0.005\,m\sigma/\tau^2$. Also shown, with arbitrary units, is the particle distribution profile demonstrating the positions of the fixed wall particles (black vertical lines) and the fluid layering near the walls (grey oscilating curve which levels off in the centre, demonstrating bulk properties there). We can see that the first layer of liquid is essentially immobile.

present in equal amounts. Therefore, our mixing function also gives a value of $M_i = 0$. Finally, consider half the particles surrounding particle i to be of like type and the other half to be of unlike type. Conceptually, this particle would be considered to be fully mixed and appropriately we obtain a mixing value of $M_i = 1$. The function $M_i(r_{\text{mix}})$ will blur the mixing level at an interface over a distance r_{mix}. Particles at an interface between two segregated fluids will have $M > 0$ when they are clearly not mixed but this is a minor point.

4. Results I: Hydrodynamic Properties

In order to generate a Poiseuille flow we have applied a constant force on each particle in the system. In a similar fashion to a pressure difference, and due to friction at the walls, this method has been shown to reproduce the desired Poiseuille flow characteristics in MD simulations [21]. For a basic channel with straight, molecularly smooth walls, no obstacles (so $L = 559.02\,\sigma$), an external acceleration of $g = 0.005\,\sigma/\tau^2$ or force mg applied to each fluid particle, and periodic boundary conditions along x we recover a nearly quadratic flow profile (see Fig. 3). Using Eq. 2 we can perform a fit to the

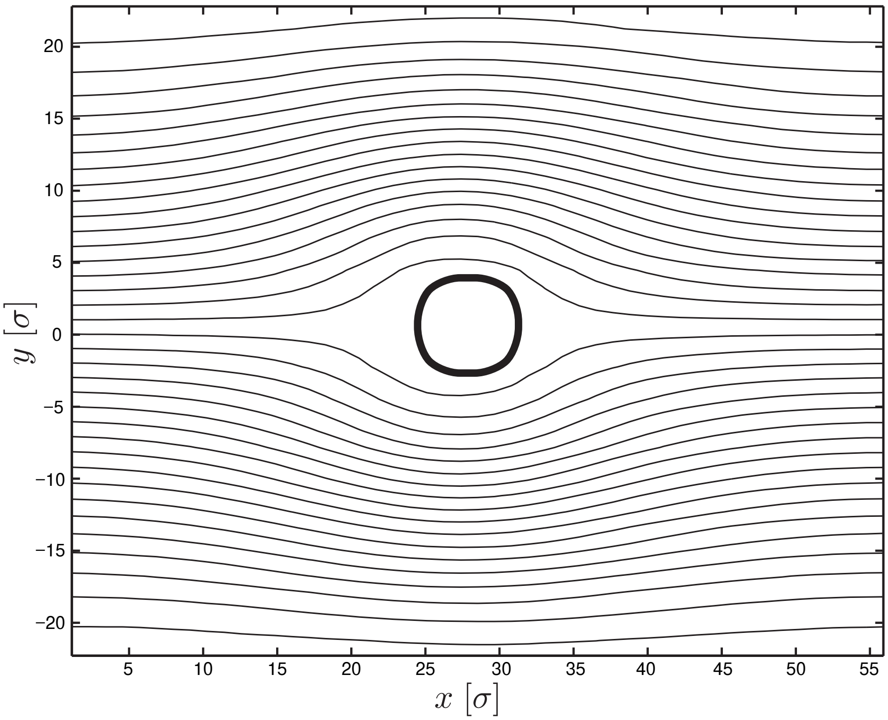

Figure 4. Streamlines demonstrating laminar flow around post of radius $R = 3.77\ \sigma$. Flow is generated by applying a force of $mg = 0.025\ m\sigma/\tau^2$ to fluid in a $W = 55.9\ \sigma$ by $L = 55.9\ \sigma$ channel. Streamlines were found by taking contours of the streamfunction ψ which itself was found by integrating the velocity field according to the definitions $\partial\psi/\partial y = u$ and $\partial\psi/\partial x = -v$ where u and v are the x and y components, respectively, of the fluid velocity. The simulation was run for 4×10^7 steps ($t = 4 \times 10^5\ \tau$) in order to get smooth data.

flow profile data and recover the position of the wall (which is indeterminate due to the soft nature of our MD beads) $y_0 = 24.83 \pm 0.20\ \sigma$ and the shear viscosity $\eta = 12.20 \pm 0.10\ \sqrt{m\epsilon}/\sigma$. We have defined the position of the wall as the position of no fluid slip (i.e., $u(y_0) = 0$). Furthermore, with the viscosity we can determine the Reynolds number from Eq. 1. Using $h = 2y_0$ and $\bar{u} \simeq 0.1\ \sigma/\tau$ (which is appropriate for what we observe, see Fig. 3) we can calculate the Reynolds number for our flow to be approximately $\mathrm{Re} \simeq 2.84 \sim O(1)$, which is clearly in the laminar flow regime. This demonstrates that our MD fluid flow simulations are certainly in the laminar regime of the predictions from macroscopic hydrodynamics.

As a further demonstration of laminar flow, we have performed simulations of fluid flow around a single obstacle. These simulations were on a system of dimensions $W = 55.9\ \sigma$ by $L = 55.9\ \sigma$ and with an applied force of $mg = 0.025\ m\sigma/\tau^2$ (which is larger than that used above to calculate Re and so this system will have a slightly larger Reynolds number). In the centre of the channel a circular post of radius $R = 3.77\ \sigma$ is placed (consisting of 32 LJ beads fixed in position) and the fluid is forced to flow past the post. According to laminar flow, we should see smooth streamlines around the post as well as identical streamlines at the input and output, indicating that the presence of the post has not disrupted the flow before and after the post (this has been observed previously in 2D MD simulations [22]). We observe exactly this in Fig. 4 where the streamlines are presented (calculated from the time-averaged velocity field). It is due to this property that we believe posts will not enhance mixing in channels (contrary to what has been reported previously [9, 10]).

From a simulation of a system similar to the one above but lacking the solid post the diffusion coefficient D was calculated from the Einstein expression [17]. For diffusion in one dimension across the channel in the y-direction the diffusion coefficient is $D_y = (3.25 \pm 0.14) \times 10^{-2}\,\sigma\sqrt{\epsilon/m}$. From this value we can calculate the Peclet number from Eq. 3 (again, using $\bar{u} \simeq 0.1\,\sigma/\tau$ and $y_0 = 24.83 \pm 0.20\,\sigma$) which yields $\mathrm{Pe} \simeq 75 \gg 1$. This clearly demonstrates that advection is dominant over diffusion in this system and mixing will be slow.

5. Results II: Purely Diffusive Mixing With No Obstacles

As a benchmark result, we ran simulations of two physically identical fluid types (A and B) in a channel with a Poiseuille flow profile (generated by a uniform force $mg = 0.005\,m\sigma/\tau^2$ in the x direction). The fluids are initially separated along the midplane of the channel (type A for $y > 0$ and type B for $y < 0$) and they are bounded by walls at $y = \pm y_0$. We have applied periodic boundary conditions in the x direction with the modification that particles flowing past the boundary on the right side have their type (A or B) reset so that the two fluids are always entering the channel in a completely unmixed state (again, type A for $y > 0$ and type B for $y < 0$). The channel length is $L = 559.02\,\sigma$ and we have $y_0 = 24.83 \pm 0.20\,\sigma$.

The flow is purely laminar and thus, as described in Section 2.1, the only drive for mixing is the diffusion of one fluid species into the other. We calculate the mixing associated with each particle using Eq. 8 (with $r_{\mathrm{mix}} = 6\,\sigma$, a value we found to strike a balance between computational efficiency and good statistical averaging) and take averages both in small xy bins as well as in slices along x and these data can be seen in Fig. 5. We can see that as the fluid travels further down the channel its mixing level rises (Fig. 5a) as the two fluid species diffuse into each other. Furthermore, we can visualize the mixing front in two dimensions in Fig. 5b which exhibits an initial $\sqrt{x}$ form and then displays an inflection point about midway along the channel, the same qualitative structure as the flow-diffusion profile for Poiseuille flow given by Eq. 6. This is expected since the mixing front should roughly correspond to the average position of the diffusing particles in Poiseuille flow. Clearly, with our channel we do not achieve 100% mixing but we can use the Peclet number in order to obtain an estimate on the length of channel L_0 required in order to obtain full mixing, $L_0 = \mathrm{Pe} \cdot y_0 \simeq 1850\,\sigma$, which is about three times the channel length we use.

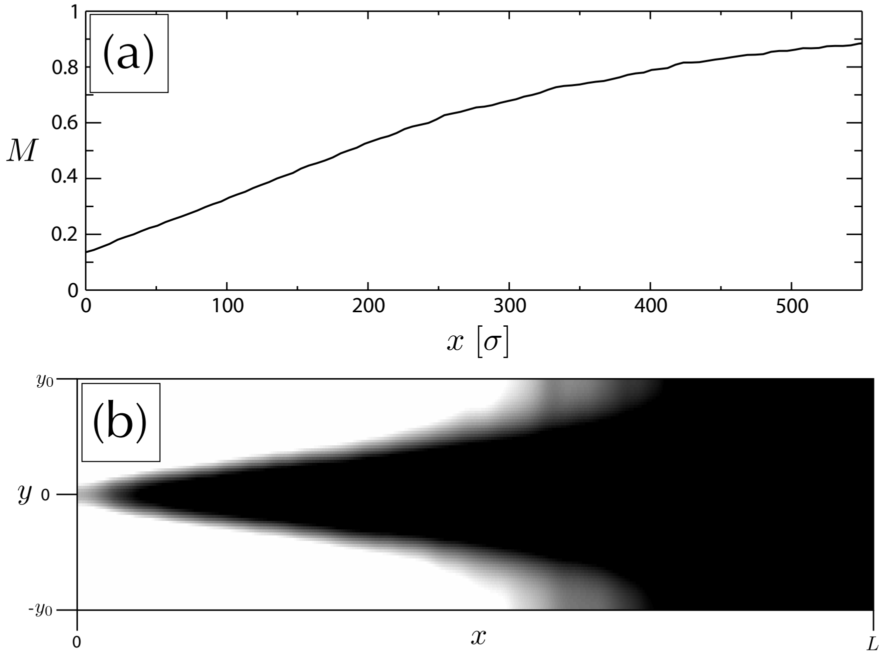

Figure 5. Mixing levels (using $r_{\text{mix}} = 6\ \sigma$) for a channel with no obstacles and smooth Poiseuille flow. (a) demonstrates average mixing level along the length of the channel in one hundred 5.59σ-wide slices. We observe the mixing level increase as the fluids flow along the channel and diffuse into each other. Note that $M \neq 0$ at $x = 0$ since there will be a finite level of mixing measured due to the contact between fluids at the initial interface (r_{mix} is finite). (b) demonstrates the mixing level averaged in a one hundred by ten 5.59σ-a-side square bins in xy and over time once the system has reached equilibrium. White represents $M < 0.5$ and black represents $M > 0.68$ with a grayscale continuum in between (therefore, white does not represent *unmixed* nor does black represent *mixed*). The values are chosen so that we can best observe the qualitative inflected shape of the mixing front which matches what is expected from the flow-diffusion profile for Poiseuille flow (see Fig. 2). The data contributing to this image has been modified by applying a Gaussian blur and increasing the image resolution.

6. Results III: Mixing With Obstacles

6.1. Prism-like Obstacle Configurations

Now, we take the previously mentioned system and place arrays of obstacles in the channel to explore their effect on the mixing efficiency of the channel. We have considered *prism*-like obstacle configurations (similar to those used by Wang *et al.* [9, 10]) as well as deconstructions of these configurations in order to test the effect of prisms versus simplified obstacle placement. The exact configurations used as well as their dimensions can be found in Fig. 6. Due to the reversibility of laminar flows the streamlines will be identical at the inlet and outlet of the channel whether or not obstacles are present (for a good discussion on this point, see the recent microfluidics

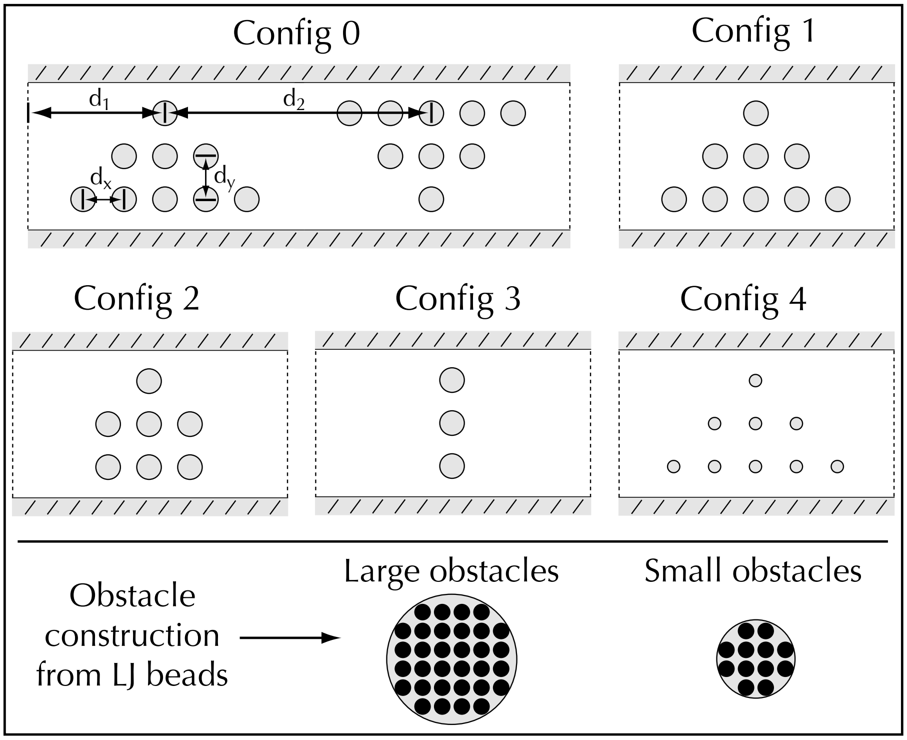

Figure 6. Schematics of the 5 obstacle configurations used in the MD simulations. Configuration 0 is used as the base and has two prism like structures inverted from each other. The centre of the first prism is a distance $d_1 = 67.08\,\sigma$ from the channel inlet and the centre of the second prism is a distance $d_2 = 100.62\,\sigma$ from the centre of the first. The obstacles are placed $d_\mathrm{x} = 16.77\,\sigma$ apart along x and $d_\mathrm{y} = 15.09\,\sigma$ apart along y and have a radius of $R = 3.77\,\sigma$. Each configuration following configuration 0 is formed by succesively removing some obstacles: First, the second prism. Then, obstacles from each end of the prism (so that configuration 3 is symmetric in the y direction). The final configuration is produced by reducing the radius of the circular obstacles in configuration 1 (radius is now $R = 2.26\,\sigma$). Also shown here is the exact Lennard-Jones bead configuration for each obstacle size.

book by Tabeling [23]). This concept was mentioned in the discussion of the Reynolds number in Section 2.1 and demonstrated for a single post in Section 4. The flow obstruction by the presence of obstacles has two effects: (i), a local disruption (i.e., flattening) of the flow profile that decays back into a parabolic profile eventually well past the obstacles, and (ii), increasing the contact region between fluid species by inducing a weak and localized lateral component to the flow.

6.2. Mixing Levels

We performed simulations on channels similar to those in Section 5 except with a shorter length ($L = 447.21\,\sigma$) and a stronger force ($mg = 0.01\,m\sigma/\tau^2$). As before, fluids enter the channel separated and diffuse as they flow down the channel except that now

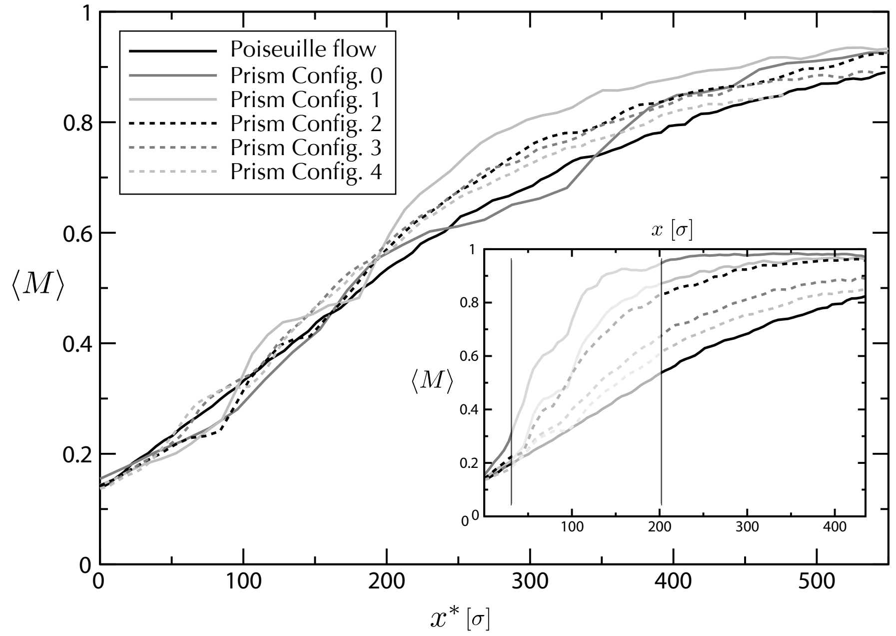

Figure 7. Mixing levels for all channels simulated ("Poiseuille flow" refers to the channel with no obstacles). The inset shows the raw data for each simulation averaged in 5.59σ-wide slices along x. The grey area shows the region affected by the presence of the obstacles (region defined as $x \in [33.54, 201.24]\ \sigma$, the maximum extent of the obstacles in configuration 0). The main figure compensates for different flow rates and the data for the obstacle-laden channels are scaled as if they have the same flow rate as the pure diffusion case. This is done for each case by the transformation: $x^* = x \cdot (\bar{u}_0/\bar{u})$ where $\bar{u}$ is the average flow rate for the simulation in question and $\bar{u}_0$ is the average flow rate for the Poiseuille case. The inset shows the data without this transformation.

there is an additional contribution to the flow characteristics due to the presence of the obstacles. Average mixing values along the length of the channel were computed and are presented in Fig. 7 along with the data for the channel with no obstacles (pure diffusion). The inset shows the raw data which demonstrates larger mixing for channels with obstacles. However, each simulation does not have the same flow rate since we are keeping g constant, not $\bar{u}$, and different obstacle configurations and numbers will result in different flow rates. In general, a stronger acceleration is needed as the number of obstacles increases since they will pose as barriers to the fluid flow. In fact, some flow rates are over 50% smaller than the pure Poiseuille case due to the hydrodynamic resistance created by the obstacles.

From Eq. A.4 (or Eq. 6), the average length along the channel a particle travels while diffusing a certain distance (or equivalently, achieving a certain level of mixing) is proportional to the average velocity: $\langle l \rangle \propto \bar{u}$; therefore we will scale the mixing data so that each obstacle-laden channel has the same flow rate as the channel with no obstacles

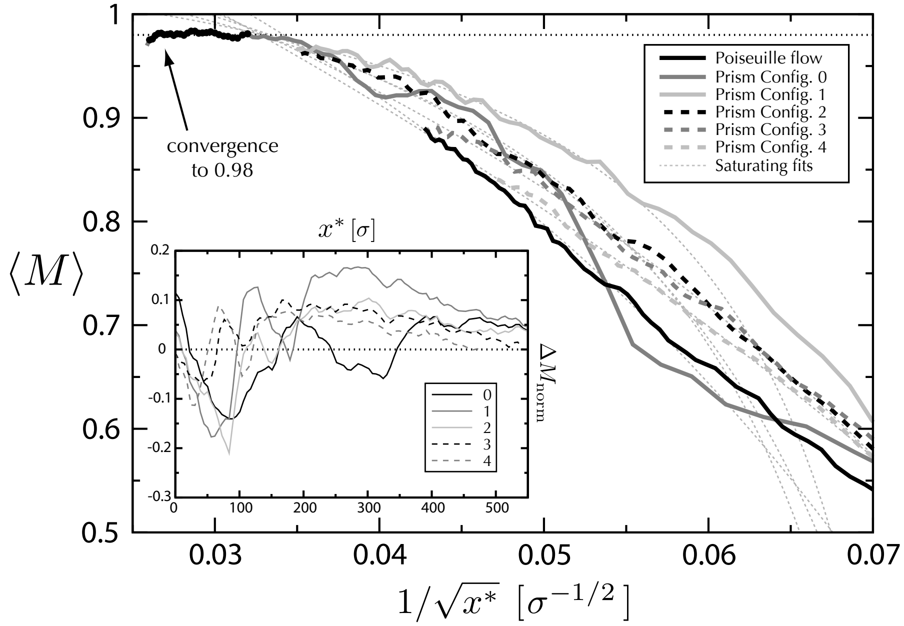

Figure 8. Inset: The difference between the mixing curves for the obstacle-laden channels and the purely Poiseuille flow channel. We can see a maximum of about 10%-20% difference in partial mixing about $x^* \in [200, 300]\ \sigma$ for obstacle configuration 1. For large x^* the difference decreases and we speculate that they will converge when $\langle M \rangle \simeq 1$ for all cases. Main plot: convergence to full mixing for large x^* using the transformation $1/\sqrt{x^*}$. We see the convergence to $\langle M \rangle \simeq 0.98$ for obstacle configuration 0 (the thin dashed line shows $\langle M \rangle = 0.98$)

(in absence of turbulence, such a rescaling can be done without changing the physics). This normalization operates as follows: $x^* = x \cdot (\bar{u}_0/\bar{u})$, where u is the velocity in an obstacle laden channel and u_0 is the velocity in the Poiseuille case. We observe that the channels with obstacles have a higher level of mixing for about $x^* > 150\ \sigma$ which is after the obstacles will begin affecting the mixing. However, since this difference decreases after about $x^* = 350\ \sigma$ the enhanced level of mixing is merely due to the fact that we are measuring before the natural point of 100% mixing (i.e., $L_{\mathrm{M}} < L_0$).

This theory suggests that if all we are doing is deforming the flow profile then all mixing curves should converge when $\langle M \rangle \simeq 1$. Our channels are too short to observe total convergence (since $\mathrm{Pe} > L/2y_0$) but there seems to be an onset of convergence for large x^* especially if we look at the normalized difference between the mixing curves in the obstacle-laden cases ($\langle M(x^*) \rangle$) and the Poiseuille case ($\langle M_0(x^*) \rangle$):

$$\Delta M_{\mathrm{norm}} = \frac{\Delta M}{\bar{M}} = \frac{\langle M \rangle - \langle M_0 \rangle}{\frac{1}{2}\left(\langle M \rangle + \langle M_0 \rangle\right)}. \tag{9}$$

This can be seen in inset to Fig. 8 for each of the obstacle configurations.

The mixing curves will converge eventually. However, our theory is that they should all converge at the same point and that should correspond to when they reach $\langle M \rangle = 1$.

The mixing level seems to saturate around $\langle M \rangle = 0.98$ rather than 1.0 which we believe is due to the presence of the walls and the finite nature of r_{mix}. To examine this closer we transform the position by taking $\xi = 1/\sqrt{x^*}$. This will allow us to extrapolate for large x^* (the square root is used to filter the first order behaviour of diffusion which is of that form, see Section 2.2 for details). Convergence can clearly be seen in Fig. 8 for configuration 0. If we take $\langle M \rangle = 0.98$ as the measure of full mixing, then configurations 0 reaches the maximum at $x^* \simeq 937.5\,\sigma$. For the other configurations we will extrapolate using an empirical fit to a saturating function constrained to the last ~15% of the transformed data. The fit follows the equation:

$$\langle M \rangle = \frac{M_1(\xi_0 - \xi)}{\xi_1 + (\xi_0 - \xi)} + M_0, \tag{10}$$

where M_0, M_1, ξ_0 and ξ_1 are the fitting parameters. The fits predict full mixing at $x^* \simeq 920.0\,\sigma$, $x^* \simeq 898.6\,\sigma$, $x^* \simeq 917.2\,\sigma$, $x^* \simeq 932.4\,\sigma$ and $x^* \simeq 856.0\,\sigma$ (for configurations 1, 2, 3, 4 and the purely diffusive case respectively). The fits can be seen as light dashed curves in Fig. 8. All of these values lie near the position $x^* = 896.8\,\sigma \pm 4.5\%$ and thus all reach full mixing around the same point.

6.3. Lengthening of Mixing Interface

An aspect of the system that may affect the mixing characteristics is the effective amount of contact between the two fluid species, the *contact length*: L_{C}. In a plain channel with no obstacles the interface between the fluids (effectively the streamline that passes through $(x, y) = (0, 0)$) is straight and thus the contact length is equal to the length of the channel: $L_{\mathrm{C}} = L$. However, if the fluids are perturbed laterally, then this streamline will follow a sinuous path down the channel and L_{C} will be the contour length of this streamline which will have the property: $L_{\mathrm{C}} > L$.

In the presence of an assymetric (in y) configuration of obstacles we observe that the fluid in the channel acquires a y component that is not present in absence of these obstacles (see Fig. 9a). Furthermore, by looking at the calculated mixing values in two dimensions we determine that the fluid follows a sinuous path down the channel (indicated by the white line in Fig. 9b). If we estimate where the interface is (by following the maximum in the mixing function) we can determine the contour length of the interface and thus L_{C}. For obstacle configuration 1 (which is representative of the others) we find $L_{\mathrm{C}} = 451.43\,\sigma$ which is $\sim 1\%$ longer than the channel length L. From Eq. 6, d and thus the position of the mixing front should scales (to first order) as $\sqrt{\langle l \rangle}$ and thus the difference in contact length we observe will result in the mixing front (approximately determined by d in Eq. 6) being closer to the wall by less than one percent. Therefore, the lengthening of the mixing interface we observe will not significantly affect the mixing properties.

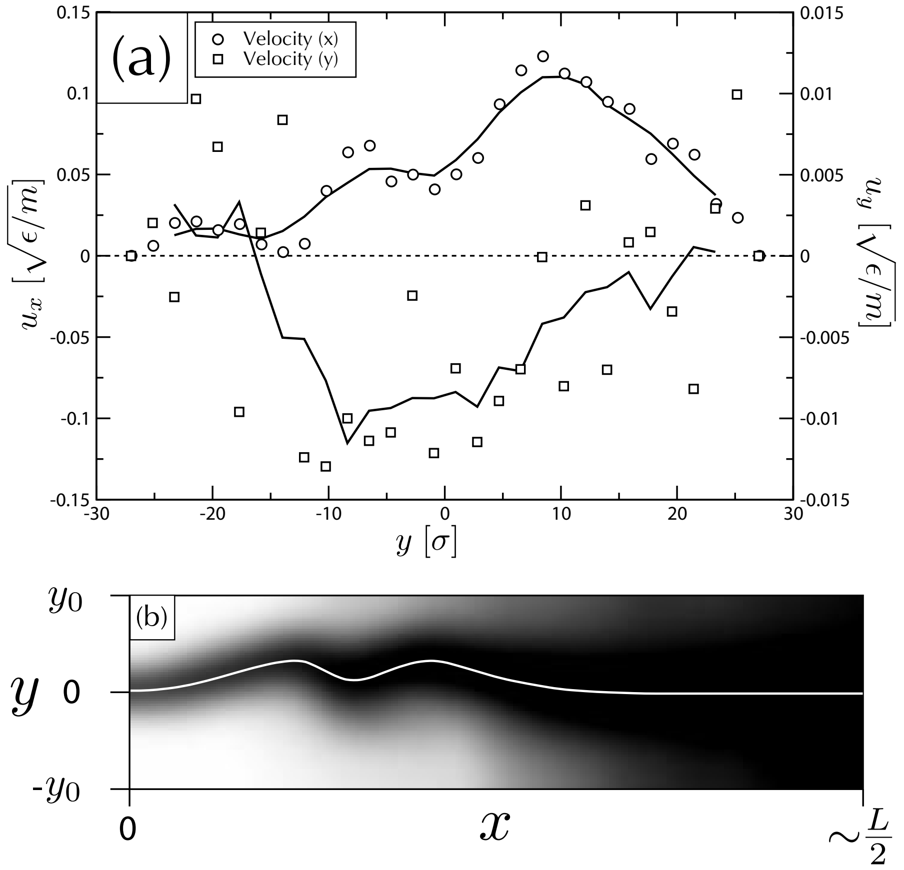

Figure 9. (a) The x and y components of the fluid velocity for obstacle configuration 1 (averaged over the regions in the vicinity of the prism and immediately after the prism, respectively). We clearly see that the obstacles resist the flow in regions (i.e., slices in y) containing more obstacles resulting in an assymetric flow profile. Also, we see that after the prism the fluid velocity has acquired a nonzero y-component. (b) The mixing observed in two-dimensions shown for x between 0 and $L/2$ and with the same averaging bins as in Fig. 5. The white line shows the central streamline (determined by eye) which exhibits sinous flow behaviour. The contour length of this line is ~1% longer than the length of the system: $L_{\mathrm{C}} \simeq 1.01L$. The sinuous flow is damped out far from the obstacles and begins to return to a Poiseuile-like flow profile with no transverse component.

6.4. Flattened Flow Profile

We measure the average flow profile over the range $67.08\ \sigma < x < 186.34\ \sigma$ immediately after the position of the obstacles configuration 3 (the symmetric obstacle configuration) in order to compare it with the flow profile from the Poiseuille case (see Fig. 10, where the flow has been normalized by $\bar{u}$ for comparison). It is clear by comparing the profiles that the presence of obstacles flattens the flow profile in the centre of the channel. This observation is less clear from the other obstacle configurations (not shown) as the assymetric obstacle placement (in the y direction) produces an assymetric flow

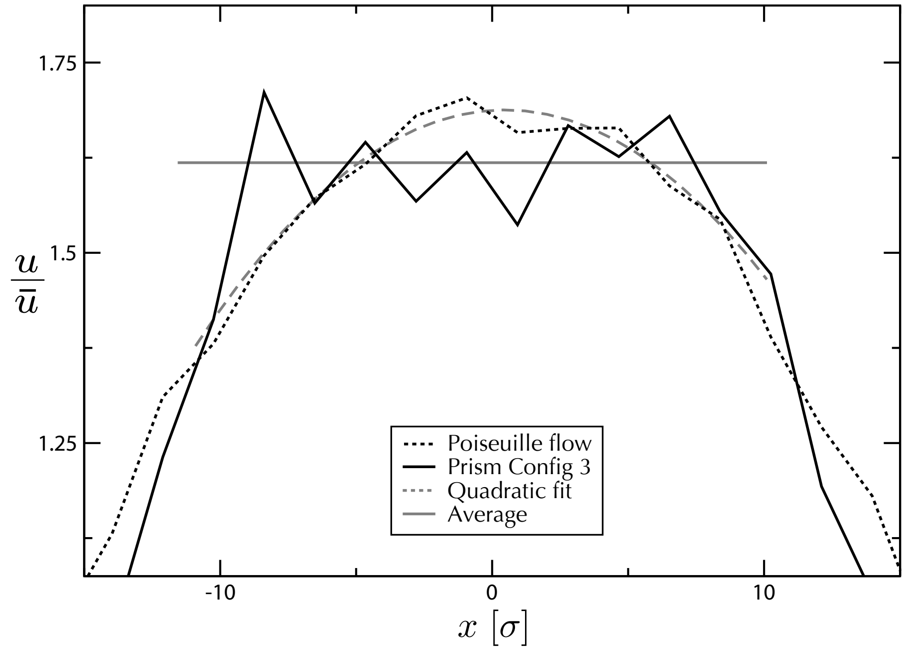

Figure 10. Flow profiles for the channel with no obstacles and for obstacle configuration 3. The each velocity profile has been normalized by its flow rate, $\bar{u}$. This representation allows us to see how the flow deforms in the presence of obstacles in comparison to the Poiseuille case. We can see that the obstacles deform the flow profile with repect to the quadratic Poiseuille case by flattening it. The solid grey line shows the average value of the flattened profile and the dashed grey line is a quadratic fit to the Poiseuille profile, both constrained to the region $x \in [-10, 10]\,\sigma$.

profile. Furthermore, as we saw in the previous section, the flow profile also varies along the length of the channel and recovers a Poiseuille-like profile far from the obstacles. Essentially, the flow deformations are damped as the fluid travels farther from the obstacles and we would expect to recover a Poiseuille flow far from the obstacles.

Since the flow profile is flattened in the centre of the channel, we expect this to affect the mixing. According to the theory outlined in Section 2.3, this effect should increase the level of partial mixing we observe. Clearly, the mixing levels we measured in Section 6.2 rise in the presence of obstacles, compared to the Poiseuille case, immediately after the position of the obstacles. Also, we observe that the configurations with assymetric profiles (not shown) also appear to increase the level of mixing. Overall, these profiles are also “flatter” than the Poiseuille case. If the channel length is such that the outlet is immediately after the obstacles, then it would give the impression that the presence of obstacles increases mixing efficiency, when in fact only the partial mixing will have been improved. Both flattened and non-flattened flow profiles will reach full mixing at the same point.

7. Conclusions

We have presented a basic theory for diffusion (and thus mixing) in channels with both flat and Poiseuille flow profiles. Under conditions where the flow rate is the same then all channels of length greater than L_0 (which has a universal value for channels with the same flow rate) will achieve 100% mixing by the outlet. We have also proposed a function to quantify the level of mixing in a fluid and associate a unique value to each element in a system consisting of an ensemble of particles (such as a Molecular Dynamics simulation of Lennard-Jones beads). In macroscopic models (or experimental observations) this expression can be generalized in terms of densities or concentrations of the individual species.

We have predicted using theory and demonstrated with MD simulations that the presence of obstacles in channels with fluid flow will disrupt the flow by flattening the profile across the channel (at least over a finite channel length) and introduce a lateral component to the velocity. In systems where the flow is composed of two identically-interacting species, the former effect causes the measured mixing to be larger if the point of measurement is less than L_0 and the latter effect lengthens the contact between fluids but does not contribute much to mixing. It is the former effect, the flow profile flattening, that has led to obstacles being considered as mixing enhancers in previous studies. This is true if one is aiming to enhance partial mixing but that is not usually the case. Normally one wishes to shorten the distance and time required to attain complete mixing and we have demonstrated that it cannot be accomplished by obstacles in microchannels.

At the present time, we are exploring modifications to the relative strengths of the attractive and repulsive components of the Lennard-Jones potential in order to simulate immiscible fluids. This technique can also simulate hydrophobicity and various degrees of wall wetting. We are also exploring the mixing properties of very small channels where the nanoscopic structure of the fluids becomes apparent and will affect the physical properties of the system. Furthermore, since we have used Molecular Dynamics to model ths system it is trivial to simulate complex fluids, such as those composed of dimers, oligomers and polymers, a task that is difficult using traditional macroscopic models.

8. Acknowledgements

G. W. S. would like to acknowledge the financial support of a Natural Science and Engineering Research Council (NSERC) Discovery grant. E. C. J. O. would like to acknowledge the financial support of the Sun Microsystems of Canada Scholarship, the Nunatsiavut Government PSSSP and the University of Ottawa Admissions Scholarship. Furthermore, E. C. J. O. would like to thank F. Tessier, M. Kenward, S. Casault, M. Bertrand and L. Taylor for discussions, assistance and support in the preparation of this work.

Appendix A. Probabilistic Derivation of the Poiseuille Flow-diffusion Profile

From the solution of the one-dimensional diffusion equation we have that the probability distribution for finding a particle in space and time is

$$p(y,t) = \sqrt{\frac{1}{4\pi Dt}} \exp\left(-\frac{y^2}{4Dt}\right). \tag{A.1}$$

For some parameter $\gamma(y,t)$ we can find its average value $\langle\gamma\rangle$ over all space and in the range $t \in [0,T]$ from the following [24]:

$$\langle\gamma\rangle = \frac{\int_{-\infty}^{\infty}\int_0^T p(y,t)\gamma(y,t)dtdy}{\int_{-\infty}^{\infty}\int_0^T p(y,t)dtdy}. \tag{A.2}$$

Let us define the distance along the channel a particle has travelled while diffusing a distance d across the channel as l. The average distance can be expressed as $\langle l\rangle = \langle u\rangle t_{\mathrm{D}}$ where $\langle u\rangle$ is the average velocity and $t_{\mathrm{D}} = d^2/2D$ is Eintein's relation for the average time taken for a particle to diffuse a distance d. We are assuming a Poiseuille flow profile that varies only in space given by

$$u(y) = u_0\left(1 - \frac{y^2}{y_0^2}\right).$$

Using the probabilistic arguments outlined above (with the temporal range $t \in [0, t_{\mathrm{D}}]$) we can calculate the average velocity to be

$$\langle u\rangle = u_0 - \frac{u_0 D}{y_0^2}t_{\mathrm{D}} = u_0\left(1 - \frac{1}{2}\frac{d^2}{y_0^2}\right). \tag{A.3}$$

This is as expected: the average speed at $d = 0$ should be the peak of the flow profile (u_0) since this is the centre of the channel and thus the maximum velocity and it reduces to $u_0/2$ at the wall ($d = y_0$) which is expected for Poiseuille flow. For particles starting in the centre ($y(t=0) = 0$) we calculate $\langle l\rangle$ by multiplying Eq. A.3 by t_{D}:

$$\langle l\rangle = \langle u\rangle t_{\mathrm{D}} = \frac{u_0 d^2}{2D}\left(1 - \frac{1}{2}\frac{d^2}{y_0^2}\right), \tag{A.4}$$

which demonstrates the correction to Eq. 5 due to the quadratic nature of Poiseuille flow.

Appendix B. Discretized Derivation of the Poiseuille Flow-diffusion Profile

Given a generic flow profile which varies as a function of y, $u = u(y)$, we derive a numerical as well as analytic method of finding the average position along the channel a particle has travelled, $\langle l\rangle$, while diffusing a distance d across the channel. We will discretize the profile $y > 0$ into N slices. We will define the following: Δh is the width of the slices and h_i is the distance to the i^{th} slice from the centre of the profile. The distance h_i can be expressed as $h_i = i\Delta h$ where $i = 0, 1, \ldots, N-1, N$ and $h_N = y_0$. The velocity profile is discretized as $u_i = u(h_i)$.

It can be useful to express the distance across the channel that a fluid particle diffuses as a function of the distance along the channel fluid has travelled due to imposed flow. This expression can give us an idea of the channel length required to mix two fluids when we rely solely on diffusion. We have discretized the velocity profile along y and consider each slice to have a constant velocity of u_i. Starting from the centre ($y = h_0 = 0$) the average time taken to diffuse to the end of the i^{th} slice can be found from Eq. 4:

$$\langle t_{D_i} \rangle = \frac{h_i^2}{2D}.$$

Therefore, the average time a particle spends in the ith slice, $\langle t_i \rangle$, is the time taken to diffuse to the end of that slice minus the time taken to diffuse to the beginning of that slice (or to the end of the previous slice): $\langle t_i \rangle = \langle t_{D_i} \rangle - \langle t_{D_{i-1}} \rangle$. Now, we can write the average distance travelled along the length of the channel (in the direction of the flow) while a particle is in the i^{th} slice, $\langle \lambda_i \rangle$, as this time multiplied by the velocity in the slice

$$\langle \lambda_i \rangle = u_i \langle t_i \rangle = u_i \left(\langle t_{D_i} \rangle - \langle t_{D_{i-1}} \rangle \right).$$

Therefore, the average distance travelled along the channel after diffusing to the n^{th} slice is

$$\begin{aligned}\langle l_n \rangle &= \sum_{i=1}^{n} \langle \lambda_i \rangle = \sum_{i=1}^{n} u_i \left(\langle t_{D_i} \rangle - \langle t_{D_{i-1}} \rangle \right) \\ &= \frac{1}{2D} \sum_{i=1}^{n} u_i \left(h_i^2 - h_{i-1}^2 \right).\end{aligned}$$

We can rewrite the inner portion as follows

$$h_i^2 - h_{i-1}^2 = (h_i + h_{i-1})(h_i - h_{i-1}) = \Delta h (h_i + h_{i-1})$$

and so the sum is now

$$\langle l_n \rangle = \frac{1}{2D} \sum_{i=1}^{n} u_i (h_i + h_{i-1}) \Delta h. \tag{B.1}$$

This equation represents a numerical method of solving $\langle l \rangle$ as a function of d (where $d = h_n$) by discretizing the spacial coordinate and the velocity profile.

If we take the limit of Eq. B.1 as $\Delta h \to 0$:

$$\lim_{\Delta h \to 0} \langle l_n \rangle = \lim_{\Delta h \to 0} \frac{1}{2D} \sum_{i=1}^{n} u_i (h_i + h_{i-1}) \Delta h \tag{B.2}$$

then we can turn it into an integral over h:

$$\begin{aligned}\langle l \rangle &= \frac{1}{2D} \int_0^d u(h)(h+h)dh \\ &= \frac{1}{D} \int_0^d u(h) h dh.\end{aligned} \tag{B.3}$$

This expression can give an analytic result but may not be useful in all cases (such as if $u(y)$ cannot be integrated or is only known numerically). Note that this entire treatment is for a particle diffusing from the centre of the channel towards the wall at $y = y_0$. However, due to the symmetry of the velocity profile the result will hold for a particle diffusing from the centre in the negative y direction as well.

As an example, we substitute the Poiseuille profile for $u(h)$ (from Eq. 2) and evaluate the integral in Eq. B.3:

$$\begin{aligned}\langle l \rangle &= \frac{u_0}{D}\int_0^d \left(1 - \frac{h^2}{y_0^2}\right) h dh \\ &= \frac{u_0 d^2}{2D}\left(1 - \frac{1}{2}\frac{d^2}{y_0^2}\right), \end{aligned} \tag{B.4}$$

which demonstrates the correction due to the quadratic nature of the profile. We can see that the method derived here gives the same result as the probabilistic method derived in Appendix A.

References

[1] A.P. Sudarsan and V.M. Ugaz. Multivortex micromixing. *Proceedings of the National Academy of Sciences*, 103:7228, 2006.

[2] C.H. Lin, L.M. Fu, and Y.S. Chien. Microfluidic T-Form Mixer Utilizing Switching Electroosmotic Flow. *Anal. Chem.*, 76:5265–5272, 2004.

[3] A.O. El Moctar, N. Aubry, and J. Batton. Electro-hydrodynamic micro-fluidic mixer. *Lab Chip*, 3:273–280, 2003.

[4] A.D. Stroock and G.M. Whitesides. Controlling flows in microchannels with patterned surface charge and topography. *Acc. Chem. Res*, 36:597–604, 2003.

[5] O. Kuksenok, JM Yeomans, and A.C. Balazs. Using patterned substrates to promote mixing in microchannels. *Phys. Rev. E*, 65:31502, 2002.

[6] J. B. Knight, A. Vishwanath, J. P. Brody, and R. H. Austin. Hydrodynamic focussing on a silicon chip: mixing nanoliters in microseconds. *Phys. Rev. Lett.*, 80:17, 1998.

[7] A.D. Stroock et al. Chaotic Mixer for Microchannels. *Science*, 295:647–651, 2002.

[8] T.M. Squires and S.R. Quake. Microfluidics: Fluid physics at the nanoliter scale. *Rev. Mod. Phys.*, 77:977–1026, 2005.

[9] H. Wang, P. Iovenitti, E. Harvey, S. Masood, and R. Deam. Mixing of liquids using obstacles in microchannels. *Proceedings of SPIE*, 4590:204, 2001.

[10] H. Wang, P. Iovenitti, E. Harvey, and S. Masood. Optimizing layout of obstacles for enhanced mixing in microchannels. *Smart Mate. and Struct.*, 11:662–667, 2002.

[11] P.A. Thompson and S.M. Troian. A general boundary condition for liquid flow at solid surfaces. *Nature*, 389:360–362, 1997.

[12] J. Koplik and J. R. Banavar. No-slip condition for a mixture of two liquids. *Phys. Rev. Lett.*, 80:5125–5128, 1998.

[13] N.V. Priezjev, A.A. Darhuber, and S.M. Troian. Slip behavior in liquid films on surfaces of patterned wettability: Comparison between continuum and molecular dynamics simulations. *Phys. Rev. E*, 71:41608, 2005.

[14] E. C. J. Oliver and G. W. Slater. Forced rotational motion of fluid in a cavity: A molecular dynamics study. *Submitted to J. Chem. Phys. July 14, 2006.*

[15] E.R. Dufresne, D. Altman, and D.G. Grier. Brownian dynamics of a sphere between parallel walls. *Europhys. Lett.*, 53:264–270, 2001.

[16] S. G. Anekal and M. A. Bevan. Self-diffusion in submonolayer colloidal fluids near a wall. *J. Chem. Phys*, 125:034906, 2006.

[17] D. C. Rapaport. *The Art of Molecular Dynamics Simulation.* Cambridge University Press, Cambridge, 1995.

[18] T. Soddeman, B. Dünweg, and K. Kremer. Dissipative particle dynamics: A useful thermostat for equilibrium and nonequilibrium molecular dynamics simulations. *Phys. Rev. E*, 68:046702–1–8, 2003.

[19] E. A. J. F. Peters. Elimination of time step effects in dpd. *Europhys. Lett.*, 66:311–317, 2004.

[20] M. Camesasca, I. Manas-Zloczower, and M. Kaufman. Entropic characterization of mixing in microchannels. *J. Micromech. Microeng.*, 15:2038–2044, 2005.

[21] J. Koplik and J. R. Banavar. Continuum deductions from molecular hydrodynamics. *Annu. Rev. Fluid Mech.*, 27:257–292, 1995.

[22] T. Ishiwata, T. Murakami, S. Yukawa, and N. Ito. Particle Dynamics Simulations of the Navier-Stokes Flow with Hard Disks. *Int. J. Mod. Phys. C*, 15:1413–1424, 2004.

[23] P. Tabeling. *Introduction to Microfluidics.* Oxford University Press, USA, Oxford, 2006.

[24] W. A. Strauss. *Partial Differential Equations: An Introduction.* John Wiley & Sons, Inc., New York, 1992.

4

Extra Material

This chapter will present material relating to both projects that was not included in the article manuscripts. The reasons for the fact that the material was not included are due to limitations on article length, it was completed after submission of said manuscripts or that it did not flow properly with the rest of the material.

Project I: Spinning

The nondimensional Spin number, S, presented in the first manuscript as Eq. 10 has some physical significance that was not explored in that paper. Firstly, it demonstrates the inherent interdependence of the system properties and, second, it can be thought of as analogous to another nondimensional number in fluid mechanics: the Froude number. On the first point, we demonstrated in our manuscript that the tangential velocity in the cavity, u_{cav}, is proportional to the velocity near the wall in the cavity, u_{wall}. Clearly, the latter should also be proportional to the mean velocity in the channel: $u_{\text{wall}} \propto \bar{u}$. So, we can deduce that u_{cav} should be proportional to the mean velocity: $u_{\text{cav}} \propto \bar{u}$. If we square this expression and call the proportionality constant S we have: $u_{\text{cav}}^2 = S\bar{u}^2$. Now, for a circular disc of radius R the radial acceleration can be expressed as $G = u_{\text{cav}}^2/R$ and so we can rewrite the expression as $GR = S\bar{u}^2$ from which we have the definition of the spin number presented in the manuscript:

$$S \equiv \frac{GR}{\bar{u}^2}. \tag{4.1}$$

We can also derive the Spin number by considering the Froude number (presented in the Introduction) which measures the relative effects of intertial forces and gravity forces in a hydrodynamic system. If we replace the external gravity force with our radial acceleration G, use a length scale corresponding to the radius of the cavity R and use the flow rate $\bar{u}$ as the inertial flow velocity we can create a nondimensional Spin-Froude number defined as

$$S_{\mathrm{Fr}} \equiv \frac{\bar{u}}{\sqrt{GR}}. \tag{4.2}$$

In this case we are relating the inertial force in the channel to the radial force in the cavity. This can be related to our Spin number as $S = S_{\mathrm{Fr}}^{-2}$. We can calculate the S_{Fr} number for our simulations in the manuscript to be $S_{\mathrm{Fr}} = 3.12$ and for the experiments performed by Chiu *et al* to be $S_{\mathrm{Fr}} = 1.70$, again demonstrating that we are operating in the same regime.

Project II: Mixing

In the second Appendix to the manuscript of the second article we present a method for numerically calculating the flow-diffusion profiles of a channel given a discrete velocity profile. However, in the paper we did not show any actual calculations from our simulation. From the analysis we did perform, we obtained the discrete flow profiles for each simulation (such as those presented in Fig. 10 of the manuscript) and we can easily use Eq. B.1 to calculate the flow-diffusion profiles. This can be seen in Fig. 4.1 where we have normalized the curves so that they all reach $y_0 \simeq 24.83\ \sigma$ at the same point (which we label L_0). This is essentially normalizing the flow profiles so that they have the property $\bar{u} = 2DL_0/y_0^2$. This figure is the numerical equivalent to the theoretical prediction presented in Fig. 2 of the manuscript. The data is shown for each obstacle configuration and for the channel without obstacles as well as for the theoretical prediction for a flat flow profile with the same flow rate. Clearly, the obstacle laden channels show the position across the channel, d, as larger than that for the channel without obstacles measured at a point $L_{\mathrm{M}} < L_0$. This would correspond to an increased level of partial mixing measured at this point which is exactly what we observe in the article manuscript.

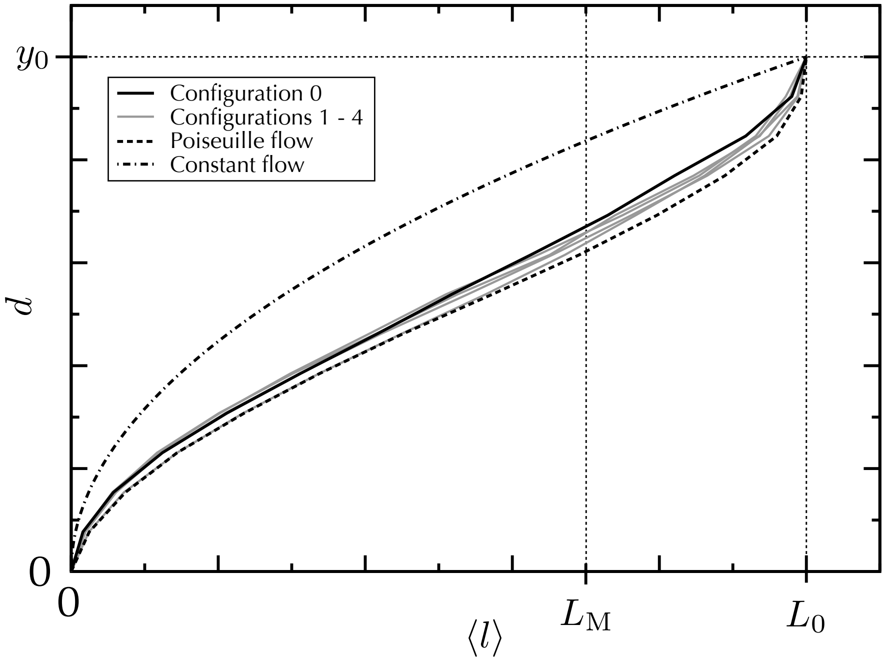

FIGURE 4.1 Numerically calculated flow-diffusion profiles for simulations of a plain channel (Poiseuille flow) and obstacle laden channels (configurations 0 to 4) as well as the theoretical prediction for a constant flow given by $u = 2DL_0/y_0^2$. All of the results for channels with obstacles show that the flow-diffusion profile is greater than that for a channel with no obstacles (measured at a point $L_\mathrm{M} < L_0$). Obstacle configuration 0 is shown in black as a clear demonstration.

It should be noted that we use the flow profiles averaged over a length of channel near the position of the obstacles. The flow will slowly recover a Poiseuille profile far from the obstacles which will affect the flow-diffusion profiles. Therefore, we must interpret the data presented here as an upper bound for the flow-diffusion profiles in obstacle-laden channels. However, it should be possible to extend the theory for these profiles to include flows that vary along the length of the channel in addition to the width.

5

Conclusions

This thesis contributes to the field of microfluidics with two distinct studies and adds to the growing body of work demonstrating the utility of Molecular Dynamics as a simulation tool for microfluidic and nanofluidic systems. There is a growing need for a better understanding of the physics governing microflows and for fresh ideas and new approaches to old problems. As we have shown in this thesis, there is still room for explorations of new phenomena and explanations of old results.

The two projects presented here are distinct but share a few similarities: both are low Reynolds number flows over similar length scales and we apply the same model to both systems. Each project has resulted in a submitted manuscript and the projects are independent of one another (i.e., they can be read in any order). There is some overlap between the two articles (such as the discussion of simulation method and hydrodynamic properties in Molecular Dynamics simulations) but for the most part they do discuss the same subject matter.

Project I: Spinning

The first project, “spinning”, was a numerical reproduction and extension of published experimental research. We recreated the microvortex studies by Chiu’s group as a Molecular Dynamics simulation and developed a method of generating spin in a more efficient manner. We began by exploring the hydrodynamic properties of a fluidic channel with no cavity and how we could modify the wall-fluid interaction. By reducing the attractive portion of the Lennard-Jones potential we decreased the interfacial tension between the wall and the fluid. Then, by measuring the slip length observed at the wall we determined that this effect corresponds to increasing the hydrophobicity of the wall: effectively allowing the fluid to acquire a significant nonzero velocity along the wall. We then applied this technique to a system containing both a channel and cavity to explore how the hydrophobicity affects the rotation of the cavity fluid. Using two schemes which selectively alter the hydrophobicity of the cavity and/or channel we were able to significantly increase the level of spin (measured by the time- and mass-averaged angular momentum) in the cavity. The two schemes selectively modify the fluid-wall interaction either along one channel wall (scheme A) or along the channel and cavity walls (scheme B). Using scheme B we were able to increase the level of spin by over 80% by reducing the surface tension by half. From finite difference calculations of a model based on the Navier-Stokes equation we were able to determine how the cavity spin should depend on the channel properties (in this case, the flow) and were able to fit our data succesfully. Finally, we proposed a nondimensional parameter to characterize the spin regime for studies performed on coupled channel-cavity microfluidic systems.

As far as we are aware, the technique we develop for increase spin by modifying the chemistry of the wall has never been proposed or examined experimentally. Therefore, we will contact the authors and discuss the viability of our technique as well as the possibility of a collaboration. More generally, our results show the importance of wall-fluid interaction in microsystems. Since walls play such an important role on micro- and nanoscale systems, determining how they effect the dynamics of microflows and controlling their behaviour is of paramount importance to the development of microfluidic devices.

Project II: Mixing

The second project, “mixing”, was also a numerical reproduction of a previous study. This time the study was on the mixing properties of channels with obstacles and we reproduced as well as explained the results in detail. We explored the various processes that are relevant for enhancing mixing and clarified prior interpretations of the results. The original study by Wang *et al* claimed that the presence of obstacles increased the efficiency of mixing in a microchannel. We challenged that statement in our study by breaking down all of the possible effects and how they might alter the mixing efficiency. We were able to determine that obstacles had two effects: (i) increasing the effective contact between the different fluid species by inducing flow in the lateral direction and

(ii) flattening the Poseuille flow profile over a finite length of the channel. From our simulation results we determined that the former effect is negligible and the latter effect is responsible for the conclusions drawn in the earlier paper by Wang *et al*. We showed, through theoretical arguments and simulation data, that all flow profiles of the same flow rate reach complete mixing at the same point (a length L_0, determined from the geometry of the channel and the diffusive properties of the fluid). Also in this paper we presented a theoretical prediction for diffusion of a particle across a channel in the presence of a Poiseuille flow profile. This theory explains how, with a flattened flow profile, the measured mixing at a point before L_0 will yield a higher level of partial mixing (<100%). This is the effect that was observed previously and published by Wang *et al* since their channel length is an order of magnitude smaller than the L_0 required given their channel width and Peclet number.

We have shown that simple tricks, such as those explored in this project, cannot be used to increase mixing in low Reynolds number flows. One can think of many (such as bumps and grooves along the channel walls or hydrophobic and hydrophilic patches on the wall) but more complex schemes are required in order to significantly enhance the mixing. For this reason, many schemes of increasing complexity have been and are still being explored in this field.

Further Studies

Molecular Dynamics allows the study of many physical systems that would be difficult with traditional methods (such as macroscopic hydrodynamics). One example is our treatment of hydrophobic walls: we have only made assumptions on the *interaction* between the wall and the fluid. In a hydrodynamic model one would have to make assumptions on the observable properties of the system (such as the fluid velocity). Also, as shown in the introduction, Molecular Dynamics allows for the study of immiscible and partially immiscible fluids in a natural way: by modifying the interaction between fluid species. This would, again, require a complex model in order to be simulated with macroscopic theories.

In future work we would like to extend the projects from two dimensions to three dimensions, particularly for the mixing project. Although we are confident in the generic physics of our results, we would be interested in exploring the same systems in three dimensions. Clearly, the exact numerical values we obtain will be different depending on the dimensionality but we expect to observe the same general physical trends.

One avenue that was not explored in this work is the properties of complex fluids under the two conditions studied here: rotational motion and diffusive mixing. A complex fluid would constitute an ensemble of dimers, oligomers and polymers (or other types of macromolecules, such as branched polymers) and can exhibit very unique properties. Modelling such a system is trivial with Molecular Dynamics but poses problems in macroscopic models. Furthermore, Molecular Dynamics simulations allow one to explore the properties of systems where the nanoscopic nature of materials may become apparent (as we witnessed with fluid layering near walls). Exploring either project under such conditions would be an interesting study. How does a driven *nano*vortex behave? How do the mixing properties of channels with obstacles change in the presence of the finite structure of fluids? Molecular Dynamics simulations along with other models of similar spirit (such as Monte Carlo) are indispensible tools for examining physical (as well as chemical and even biological) systems.